Development and Experimental Verification of an Analytic Model for Large Area Grating Couplers in Photonic Integrated Alignment Sensors

de Louw, Nick

Award date:
2022

ASML: Research group Optics & SXR Metrology
Eindhoven University of Technology
Department of Applied Physics

Development and Experimental Verification of an Analytic Model for Large Area Grating Couplers in Photonic Integrated Alignment Sensors

3MA60 - Graduation project Applied Physics (60 ECTS)

N. de Louw (student ID:1012059)
Master Applied Physics: Nano, Quantum and Photonics

External supervisor ASML:
dr. I.D. Setija
Optics & SXR Metrology

TU/e supervisor:
prof.dr. A. Fiore (TU/e)
Department of Applied Physics
Photonics and Semiconductor Nanophysics (PSN)

Examination committee:
prof.dr. A. Fiore
dr. Y. Jiao
dr. I.D. Setija

Eindhoven, August 2022

Public thesis

This Master's thesis follows the TU/e Code of Scientific Integrity

Abstract

The demands for continuous improvement of the alignment accuracy, in order to keep up with Moore's law, drive the development in wafer alignment metrology within ASML. Measuring more alignment marks is one possibility to realize the desired improvement of the alignment accuracy. This can be achieved by the photonic integrated circuit (PIC) alignment sensor, of which the feasibility is currently investigated within ASML. Focusing large area grating couplers are crucial elements of this PIC alignment sensor. Due to the large required size of these grating couplers there is a strong demand for alternatives to the computationally expensive rigorous simulation methods. Therefore, a novel analytic model, called the Born Approximation applied to computation of Grating Coupler Emission (BA-GCE) model, for simulating normalized radiation profiles of grating couplers of any size has been developed in this research project. The BA-GCE model is transparent and intuitive as it reveals the underlying physics. It is extensively benchmarked by comparing it with rigorous finite difference time domain (FDTD) simulations. The results seem promising as they show that the BA-GCE model is in good agreement with the theoretical expectations and the FDTD results, within its region of validity, which is limited by the Born approximation and the far field approximation that are applied in the derivation. Hence, with some further development, this model may ultimately result in an accurate analytic model which can be used in the design process of large area (focusing) grating couplers, for which rigorous simulation methods are too computationally expensive. In addition, an experimental setup has been rebuilt, re-calibrated and extensively prepared for the future measurements on the PIC alignment sensor. Therefore, calculations to obtain maximum light incoupling with this experimental setup are provided in this work. Lastly, the beam profile measurement capabilities of the setup have been demonstrated through experimental verification measurements on large grating couplers.

Acknowledgements

In the first place I would like to thank Irwan Setija for the daily supervision and guidance during my graduation project. With his expertise he was able to provide me with the necessary advices and discussions to shape and develop my graduation project, resulting in this thesis as end product. Moreover, I would also like to thank him for the opportunity to perform my graduation project at ASML, within the integrated optics research group. I am grateful that I was given the opportunity to contribute to their interesting project and I hope that it will eventually result in the desired improvement in wafer alignment. Another word of gratitude to the complete integrated optics research group at ASML for making me feel welcome as a member of their team and for making my time at ASML a real pleasure. A special mention to Jorn van Engelen, to whom I am grateful for helping me with all his expertise on Lumerical simulations. Furthermore, I would like to thank my TU/e supervisor Andrea Fiore for his guidance during the graduation project, but even more for his help in the process of finding this perfect internship opportunity. Finally, a word of gratitude to all other interns and employees at ASML who helped me in some way or another during my year at the company. It has been an honor and a pleasure to perform my graduation project within the integrated optics research group at ASML. I wish them good luck with their research and hopefully someday the promising potential of the PIC alignment sensor will be realized, resulting in the integration of this sensor into the ASML lithography machines.

Contents

Chapter 1

Introduction

Integrated circuits (ICs), or more commonly known as chips, have taken up a vital role in our day-to-day existence over the past decades. They empowered the technological revolution that led to our modern digital society, as ICs have developed into the core element of nearly all electronic devices. The destructive impact of the recent global chip shortage on our modern society has demonstrated the enormous reliance on this technology. This vital role of the ICs in our society drives continuous developments in this field. The foundation for these rapid developments is laid by the continuous reduction of feature sizes on the ICs, known as the famous "Moore's law" [2]. Smaller device features obviously allow for more functionality in a smaller volume [3]. In addition, it also leads to an increase in processing speed and a reduction of the power consumption [3].

ICs are fabricated in a repetitive layer by layer process. After a layer is grown on the wafer, the pattern with the desired features is created in this layer through photolithography, after which the next layer is grown and patterned. The photolithography process starts by covering the wafer with a thin layer of photo-resist, which is a light sensitive chemical. Subsequently, a complex machine is used to project an image, including parts of the IC features, onto the wafer. In this machine, a light source and a complex collection of high quality optical elements is used to shrink and project the image from a mask (reticle), shaped with the desired pattern, onto the wafer. The parts of the photo-resist that are then exposed to the light will either harden or soften and thereby a contrast, containing the desired features, is created on the wafer. In order to convert this into a patterned layer, the wafer is developed after light exposure. This means that the soft resist is removed and only the harder photo-resist areas remain on top of the wafer. The photo-resist that remains on top of the wafer protects the material underneath from being etched away in the next step. Hence, in the selective etching step only unprotected areas are etched away. Afterwards, the remaining photo-resist layer is also removed. Finally, the etched parts can be filled with materials with specific properties to create functionality into the patterned layer. This process for single layer patterning is repeated multiple times to create the ICs. The most critical step in this complex IC manufacturing process is the light exposure step in which the image from the reticle is projected onto the wafer. ASML is, by far, the world leading company in the fabrication of the photolithography machines that are able to perform the exposure step. Since these machines are responsible for the most critical step, their improvements are key for enabling further development of ICs, thereby giving ASML a vital position in the world IC industry.

As ICs consist of multiple layers on top of each other, it is crucial for its performance that the features in each of these layers are accurately positioned relative to the underlying pattern. Small misalignments of a few nanometers can cause serious problems in the functionality of the ICs. Hence, accurate metrology is required to position the wafers in the lithography machine such that the features in each layer are aligned on top of each other with the highest possible accuracy. Yet, as features sizes of ICs continue to decrease in order to keep up with Moore's law, the requirements on alignment accuracy increase, resulting into a continuous development in wafer alignment metrology within ASML.

1.1 Wafer metrology

In general, wafer metrology can be divided into a part before exposure to the light image and after exposure. After exposure of the photo-resist layer to the light pattern, it is important to measure and

monitor the quality of the created pattern before it is processed into a product layer. The quality is measured in terms of two parameters: the overlay and the critical dimension uniformity (CDU) [3]. The overlay quantifies the misalignment between the top layer and the underlying pattern. The CDU, as the name suggests, quantifies the uniformity of the critical dimension (CD), which is the minimum feature size, over the wafer. Large CD variations and large overlay values both have a destructive impact on the IC performance [3]. Therefore, the metrology of these two parameters and the immediate correction of the photolithography machine through the metrology feedback will minimize the CD variations and overlay values, thereby securing a high quality of the machine output. Even more important than metrology after exposure is the metrology before light exposure. By accurately measuring the wafer position and height variations before exposure, the initial overlay values and CD variations can be minimized. These measurements are currently performed by two bulk optical sensor systems, illustrated in figure 1.1, where the middle module is the alignment sensor and the two outer modules are part of the level sensor. The level sensor is used to construct an accurate height map of the wafer. It is crucial to determine this height map, since height variations across the wafer will lead to small focus offsets, which will lead to significant CD variations [3]. Hence, by accurately measuring the height map of the wafer with the level sensor, the modules in the machine can be adjusted such that the focus offsets are counteracted and CD variations are minimized. In addition, the alignment sensor is used to accurately measure the position of the (deformed) wafer grid. It is called a wafer grid because the wafer generally consists of multiple rectangular dies (fields), with an IC in each of these dies. The accurate position measurement is critical in order to obtain the required low overlay values of just a few nanometers, since the wafer is initially positioned onto the wafer stage in the lithography machine through a robotic arm, with a relatively coarse accuracy of a few micrometers [3]. The focus of this research project is on the alignment sensor, therefore it is beyond the scope of this project to provide further details on the other metrology tools. Hence, the remainder of this thesis will be devoted to the alignment sensor.

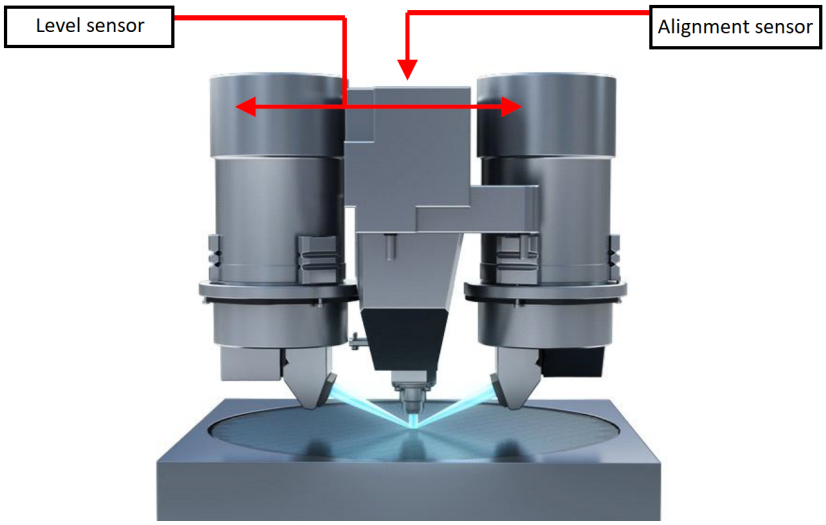

Figure 1.1: Illustration of the current bulk optical sensor systems for wafer metrology before exposure in the ASML photolithography machines. The two outer modules are part of the level sensor, which is used for measuring the wafer height map and the middle module is the alignment sensor, which is used to measure the position of the (deformed) wafer grid. Adapted from: [4]

1.2 Alignment sensor

As mentioned before, the alignment sensor measures the exact wafer grid position before light exposure in order to obtain good overlay performance. The wafer grid position is determined by measuring the position of a number of alignment marks located on the wafer, with respect to a certain reference position. For an ideal non-deformed wafer grid (figure 1.2), two alignment marks in each of the two in-plane directions (x and y) would be sufficient to determine the complete two-dimensional (2D) wafer grid, defined by the four parameters: x-translation, y-translation, magnification and rotation. However, in reality the wafer grids are often deformed, which complicates the alignment sensor measurement. Certain wafer processing steps, as well as the clamping of curved wafers on flat wafer tables can cause large in-plane wafer distortions [3]. Consequently, as illustrated in figure 1.2, deformed wafer grids cannot be

accurately measured by only four alignment marks anymore. ASML is working in multiple different areas to mitigate this deformation challenge in alignment. For example, there is an ongoing research into the wafer table and clamping technique to minimize the deformations introduced by this. Furthermore, the model for determining the wafer grid from the alignment marker positions is constantly reviewed and improved. Yet, there are still tens of alignment marks needed to be able to accurately measure the local deformations of the wafer grid, instead of the four marks in the ideal case of a non-deformed wafer.

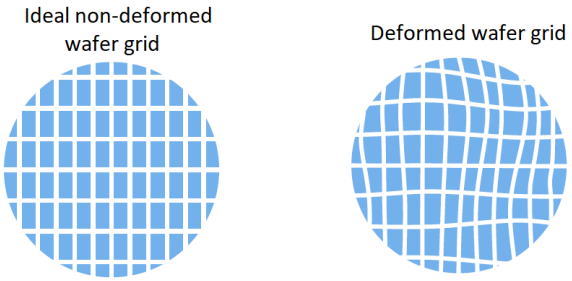

Figure 1.2: Schematic illustration of an ideal non-deformed wafer grid (left) and a deformed wafer grid (right), for which more alignment marks are required to determine the local deformations. Adapted from: [4]

The alignment sensor system thus accurately measures the position of alignment marks on the wafer. These alignment marks are phase gratings with a certain period. The working principle behind the position measurement of the alignment marker grating is illustrated in figure 1.3. A laser beam is incident on the alignment marker grating, where the light will be diffracted. A lateral displacement, δx, of either the sensor or the grating will induce a phase shift of the diffracted order according to [5]

$$\Delta\Phi_m = \frac{2\pi m}{\Lambda}\delta x, \tag{1.1}$$

where m is the diffraction order and Λ is the period of the grating. Consequently, the phase shift of the positive and negative order will differ in sign and by interfering both orders this phase shift can be measured. Hence, the positive and negative diffracted orders are captured and interfered with each other by a lens system, resulting in a sinusoidal signal. Subsequently, by passing this interference signal through a reference grating, as illustrated in figure 1.3, a sinusoidal intensity signal as a function of the alignment marker position can be measured at the detector [6]. Through a fitting procedure, the phase shift, and thereby the lateral displacement δx, can then be determined from this signal at the detector.

As features sizes on ICs continue to decrease in order to uphold Moore's law, the maximum allowed values for the overlay and the CDU become smaller and smaller. Hence, the alignment measurements also require continuous improvement of its accuracy in order to keep up with the demands resulting from Moore's law. Thus, in order to decrease the overlay error and CD variations, to be able to cope with decreased feature sizes, IC manufacturers are demanding more alignment marks on the wafer grid so that the local deformations can be determined more accurately. The demand for more alignment marks leads to the positioning of additional alignment marks intra-die, besides the marks in the scribe lines of this wafer. Therefore, this also requires smaller alignment marks. Furthermore, if the same sensor needs to measure more marks, the measurement time will increase. Consequently, an increase of the alignment measurement time will decrease the throughput of the lithography machine, which is intolerable for ASML. Hence, there is an ongoing research at ASML to solve the challenge of more and smaller alignment marks. In this project, the focus is on solving the challenge of measuring more alignment marks while not effecting the machine throughput negatively. There are multiple paths one can follow to solve this challenge. One possibility is to make the sensor perform the alignment measurements faster. Another possibility is to shrink the size of the sensors, such that it allows for parallel alignment measurements, meaning that multiple alignment marks can be measured at the same time. Moreover, another option is to investigate if a change in the structure of the alignment mark can help to make measurements faster or more accurate, in order to decrease the required amount of alignment marks to achieve a certain accuracy. Thus, at this moment multiple possible solutions to solve this challenge are investigated within ASML. One of these possible solution is based on the use of integrated optics (photonics). Integrated optics paves the way towards much smaller sensors than the bulk optical alignment sensors, which allows for parallel measurement of alignment marks. Hence, a dedicated project group within ASML is investigating if

integrated optics is one of the possible solutions to increase the alignment accuracy without decreasing the machine throughput.

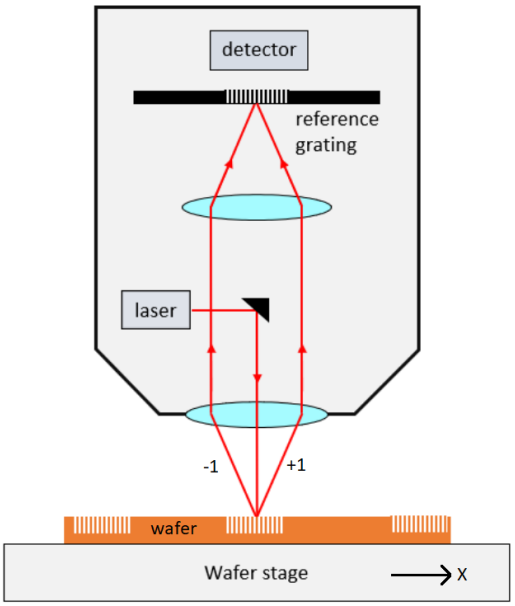

Figure 1.3: Schematic illustration of the working principle behind the alignment marker grating position measurement: A laser beam is incident on the alignment marker grating, where the light will be diffracted. The positive and negative first diffracted orders are then captured and interfered by a lens system. The interfered signal is then passed through a reference grating, after which the resulting signal is measured by the detector. Adapted from: [7]

1.3 Research goal and approach

In the process of investigating the potential of integrated optics in alignment sensors, the first step is to conduct a feasibility study. For this purpose, a photonic integrated circuit (PIC) alignment sensor prototype has been designed by J.P. de Graaf in a collaboration between Eindhoven University of Technology (TU/e) and ASML [8]. The initial plan for this graduation project was to measure and analyze the complete PIC alignment sensor prototype in order to investigate the feasibility of such an alignment sensor. Therefore, an experimental setup, capable of characterizing the performance of the PIC alignment sensor and its individual photonic components, has been made. However, due to serious problems with the (external) fabrication of this PIC alignment sensor prototype, the PIC was not delivered before the end of this project. Consequently, the focus of this graduation project has changed during the internship period. The comprehensive research goal of this project is still to contribute to the feasibility study of PIC alignment sensors. As will be explained extensively in the next chapter, grating couplers are the crucial photonic elements in the PIC alignment sensor prototype design. Grating couplers are used to emit a focusing Gaussian beam incident on the alignment mark and other grating couplers are used to capture the diffracted orders and convert them into waveguide modes on the PIC. In order to achieve the required functionality of these grating couplers, they need to be large area focusing grating couplers. There is one main challenge in the design process of such large area focusing grating couplers, which is that they cannot be simulated in full scale through conventional rigorous simulation methods, such as Lumerical finite difference time domain (FDTD) [9]. These rigorous simulation methods are too computationally expensive for large structures. This significantly complicates the design process of the large grating couplers for the PIC alignment sensor. Therefore, alternative ways of simulating radiation patterns of large area grating couplers are demanded. Hence, an analytic model which can be used to simulate radiation patterns of grating couplers of any size, is developed and extensively benchmarked in this research project. The model is based on solving Maxwell's equations in the first order Born approximation, as proposed in a paper of C.A. Flory [1]. The final model that is developed in this research project is an improved version of Flory's model, and it is also extended to include more design freedom. With some further developments, the model may ultimately be used in the design optimization process of the large area grating couplers required for the PIC alignment sensor. In addition to the development

of the analytic model, the experimental setup is prepared for the measurements on the actual PIC alignment sensor prototype. In order to demonstrate the capabilities of the experimental setup, measurements are performed on other large grating couplers from a test PIC that was provided by the TU/e. Besides the demonstration of the experimental setup, these measurements also provide results for experimental comparison of the developed analytic model. Thus, the research goal of this project is twofold. The first part of the research goal is to develop and benchmark an analytic model for large area grating couplers. The second part is to prepare the experimental setup for the measurements on the actual PIC alignment sensor once it is delivered, and to demonstrate its capabilities by performing and analyzing measurements on large grating couplers. With these two goals, this research project will contribute to the main objective of the project group to investigate the feasibility of PIC alignment sensors in ASML's metrology systems.

The design of the first PIC alignment sensor prototype is extensively discussed in chapter 2. Furthermore, this chapter will elaborate on the theory behind grating couplers. In chapter 3, the analytic model for simulating radiation patterns of grating couplers, called the "Born Approximation applied to computation of Grating Coupler Emission" (BA-GCE) model, will be developed. Starting from the underlying physics of solving the Maxwell's equations in the first order Born approximation, the first section will cover the basics behind the BA-GCE model, which is the Flory model [1]. Furthermore, this chapter will elaborate on the adaptations and extensions that have been made to the Flory model to create a novel model for simulation of grating couplers. The chapter will end with a description of the final BA-GCE model, also mentioning the approximations and limitations behind this model. It is then benchmarked in chapter 4, where the results will be compared with Lumerical FDTD [9] results and with the Flory model [1] results. Moreover, this chapter will present the results of the BA-GCE model for the large grating couplers that are measured in this research project for the experimental comparison. Additionally, this simulation chapter includes the results of the standard IMOS grating couplers on the PIC alignment sensor, which are useful for maximizing the fiber-to-chip coupling in the experimental measurements. The experimental setup that is used to perform the measurements will be explained in chapter 5, including a description of the associated measurement procedures. Chapter 6 will present the results of the experimental measurements performed in this research project. Besides the verification measurements of the optical fibers, this chapter will present the results of the large grating couplers from the test PIC provided by the TU/e. Finally, the conclusions and outlook of this study will be elaborated in chapter 7.

In conclusion, this research project will present the development and experimental verification of an analytic model for simulating large area grating couplers in PIC alignment sensors. The experimental verification will also demonstrate the capabilities of the experimental setup, which has been fully prepared for the experimental characterization of the actual PIC alignment sensor prototype in the near future. Hence, this research project will contribute in two ways to the feasibility study of the PIC alignment sensors, which should ultimately result in a PIC alignment sensor design complying with ASML's demands and restrictions.

Chapter 2

Theory and PIC design

As introduced in the previous chapter, a PIC alignment sensor prototype has been designed in order to investigate the feasibility of integrated optics alignment sensors. The working principle and important design characteristics of this prototype are elaborated in section 2.1. However, due to confidentiality issues, not all the details of the prototype design will be included in this thesis. Nevertheless, this thesis is structured in such a way that the absence of these design details has no influence on the comprehensibility of this study. As will be explained in this section, grating couplers are the essential element of the prototype design. Therefore, section 2.2 contains the theory behind these photonic components and how they are used in the PIC alignment sensor prototype. Additionally, this section will end with a short description of the large grating couplers on the TU/e test PIC that will be measured in this research project.

2.1 PIC alignment sensor prototype

The PIC alignment sensor prototype that is studied in this research project is an adaptation of the original design of J.P. de Graaf, which resulted from a collaboration between the TU/e and ASML [8]. The prototype design solely consists of passive components. Therefore, light needs to be coupled into the PIC as well as out of the PIC for external analysis. Before diving into more detail on the specific PIC design, first the general working principle is discussed in the coming subsection, which will reveal how the PIC is able to perform an alignment measurement.

2.1.1 Working principle

The working principle of the PIC alignment sensor prototype is still based on the same method as for the general ASML alignment sensor system, which was introduced in section 1.2. Thus, light is incident on the alignment marker grating, where the light will be diffracted into diffraction orders according to the well-known grating equation [10]:

$$\sin(\theta_m) - \sin(\theta_i) = m\frac{\lambda}{\Lambda}. \tag{2.1}$$

In this equation, θ_i is the angle of the incident light with respect to the grating normal, θ_m is the angle of the diffracted order m with respect to the grating normal, λ is the wavelength and Λ is the grating period. For the ASML alignment marks the period is defined as $\Lambda = \frac{16}{n}$ µm, where n is the order of the alignment mark. ASML alignment marker gratings operate as phase reflection gratings [11]. Figure 2.1 provides a schematic illustration of an example of diffraction at such a phase reflection grating, according to equation 2.1. This figure also shows the sign conventions for the angles that are used in equation 2.1. Equation 2.1 is only satisfied for a limited number of diffraction orders m, thus also for a limited number of diffraction angles θ_m. It follows that only diffraction orders, and corresponding diffraction angles, can exist for order numbers that satisfy the condition of equation 2.2.

$$\left| m\frac{\lambda}{\Lambda} + \sin\theta_i \right| \leq 1 \tag{2.2}$$

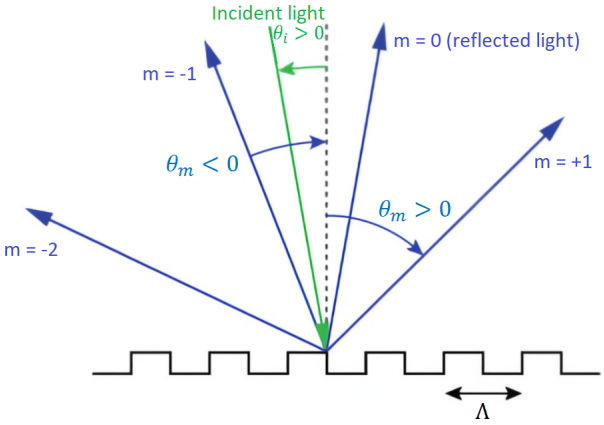

Figure 2.1: Example of light diffraction at a phase reflection grating with period Λ. The figure shows the existing diffraction orders, being the 0^{th} order (reflected light), the positive and negative 1^{st} orders and the minus 2^{nd} order in this case. The sign convention used in equation 2.1 is also illustrated in the figure. Adapted from: [12]

As mentioned before, translation of either the wafer or the sensor would introduce a phase shift between the positive and negative diffraction orders according to equation 1.1. Thus, by interfering both orders, the phase shift can be determined, from which the lateral translation can be deduced. The main difference with the current ASML alignment sensor systems is that the capturing and interference of both diffraction orders is not performed by bulk optical sensors. In the PIC alignment sensor prototype, these functionalities are all integrated on the small PIC. Furthermore, the light beam incident on the alignment mark is also produced on the PIC. The total footprint of the PIC alignment sensor prototype is not larger than 4 mm by 20 mm [8], thereby providing the significant size reduction compared to the current bulk optical sensors.

Figure 2.2 illustrates the working principle of the PIC alignment sensor prototype. The PIC is placed 10 mm above the alignment mark. A Gaussian beam is produced under an angle by the emitting grating coupler (indicated by EG) and focused at the position of the alignment marker grating, where the conventional light diffraction takes place. The positive and negative first diffracted order beams are then captured by the PIC again through the two capturing grating couplers (indicated by CG). After the beams are captured by the capturing grating couplers, they are converted into waveguide modes on the PIC. Subsequently, a beam combiner is used to interfere the positive and negative first diffracted orders, resulting in a sinusoidal output power signal which depends on the induced phase shift [8]. Based on the relation between the lateral translation and the induced phase shift (equation 1.1), a fitting procedure can then be performed to determine the lateral translation from this output signal.

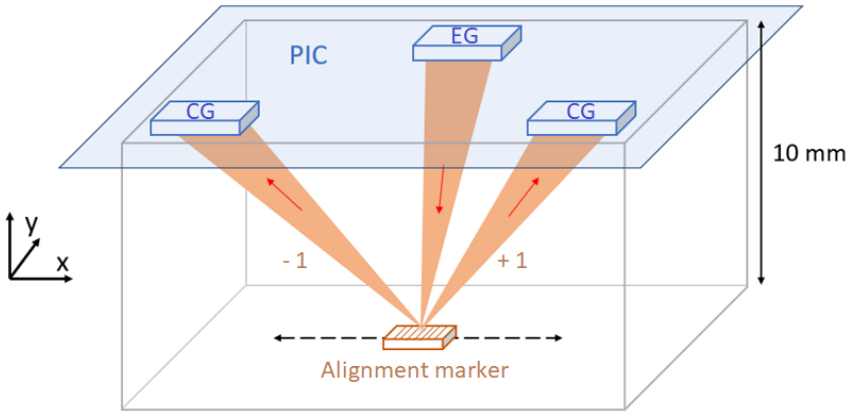

Figure 2.2: Schematic illustration of the working principle of the PIC alignment sensor prototype. The emitting grating coupler (EG) produces a focused Gaussian spot on the alignment marker grating at 10 mm from the PIC. The diffracted positive and negative first orders are captured by the 2 capturing grating couplers (CG). The alignment marker grating is moved in the indicated direction to perform the alignment scan. Adapted from: [7]

As previously mentioned, the PIC alignment sensor prototype does not include active components on the PIC. Therefore, light will need to be coupled into and out of the PIC, which is also done by grating couplers, the standard IMOS grating couplers. Hence, the importance of the grating couplers in the PIC alignment sensor must be evident by now. Section 2.2 will elaborate more on this crucial element of the sensor prototype. First, more relevant information on the specific PIC prototype design will be provided.

2.1.2 PIC design

The PIC alignment sensor prototype is realized in the indium-phosphide-membrane-on-silicon (IMOS) photonic integration platform. As the name suggests, the structure of this platform consists of an indium-phosphide (InP) membrane on top of a silicon wafer with a buffer layer in between. After an optimization process it is found that the optimum buffer layer stack consists of a 1850 nm thick benzocyclobutene (BCB) layer in between two thin ($\approx$ 50 nm) layers of silicon dioxide (SiO_2) [13]. The buffer layer prevents the optical mode in the InP membrane from coupling to the silicon substrate [14, 15]. Due to the high refractive index contrast that is created in this way, high confinement is achieved which enables high density PICs and therefore a small PIC footprint [15, 16]. In addition to the high density PICs, IMOS technology allows for low power consuming PICs [16, 17]. Hence, the IMOS platform combines the strengths of silicon photonics with the strengths of the generic InP platforms [16]. For this reason, the IMOS platform is preferred for the PIC alignment sensor, over these alternative platforms. Passive waveguides in the IMOS platform have a thickness of 300 nm and a width of 400 nm, and support both the fundamental transverse electric (TE) mode and the fundamental transverse magnetic (TM) mode at a wavelength of 1550 nm [15]. Although the waveguides support both TE and TM polarization, the PIC alignment sensor prototype is designed only for TE polarization at the single wavelength of 1550 nm [8].

Since the emitting and capturing grating couplers are both integrated on the PIC, it is important to carefully align them with respect to each other, by determining their required size and position on the PIC. The requirement for the emitting grating coupler is that it produces a focusing Gaussian beam with a beam width of 40 µm at the alignment mark [8]. The beam width is defined by the points with an intensity equal to $1/e^2$ of the maximum intensity of the beam. Additionally, it is designed in such a way that it produces this beam under a positive angle of 6 degrees with respect to the PIC normal, as shown in figure 2.2. The chosen value for the positive emission angle resulted from a trade-off between ensuring there is no diffracted angle close to zero degrees in any part of the emitting grating and minimizing the size of the PIC alignment sensor [18]. A diffracted angle of zero degrees would results in light being reflected back into the taper and the waveguide, which would be disastrous for the grating efficiency. The size and positions of the capturing grating couplers are chosen in such a way that it captures at least the complete beam width of the diffracted orders. conical diffraction calculations. Based on these requirements, the exact positions and characteristics of the emitting and capturing grating couplers are determined for the PIC alignment sensor prototype. Consequently, the PIC alignment sensor is explicitly designed to function for a single diffraction order number (positive and negative) and a single alignment marker period. If either the targeted diffraction order number or the alignment marker period is changed, the positions and characteristics of the emitting and capturing grating couplers should be adjusted accordingly. The specific PIC alignment sensor prototype consists of two sensor systems, both designed to capture the first diffraction orders. One system is designed to align on a 3^{th} order ASML alignment marker grating (period of $\frac{16}{3}$ µm), and the other one is designed to be aligned on a 5^{th} order ASML alignment marker grating (period of $\frac{16}{5}$ µm).

Figure 2.3 shows a schematic top view of one PIC alignment sensor system. The PIC thus does not contain any active elements. Hence, the light needs to be coupled into and out of the PIC externally. For this purpose, an external laser source is connected to a fiber, which will couple light into the PIC by a fiber-to-chip coupling at the standard IMOS input grating coupler (1). Section 2.2 will elaborate on how this fiber-to-chip coupling is established. Through this coupling, the light enters the waveguide which is connected to the emitting grating coupler (2). The emitting grating coupler consists of a taper and an apodized 2D focusing grating coupler to produce a beam into free space which is focused at the alignment marker, which is at 10 mm directly below the center of the PIC [18]. The positive and negative first diffraction orders, diffracted by the alignment marker, are then captured by the two capturing grating couplers (3a and 3b). These capturing grating couplers consist of two main parts: a free space to slab mode converter and a slab mode to waveguide mode converter. The diffracted beam, incident at an angle on the capturing grating coupler, is converted into a guided slab mode by an apodized rectangular

grating coupler (red part). Subsequently, the guided slab mode of hundreds of microns wide is converted into a 400 nm wide waveguide mode through a gap coupler (pink part). More details on the emitting and capturing grating couplers are provided in section 2.2.4. After the capturing and conversion of the diffracted order beams, both waveguide modes are interfered at the beam combiner (4), after which the interference signal can be extracted at the standard IMOS output grating coupler (5). The signal can be extracted again through a chip-to-fiber coupling. The fiber can then be connected to an external photodetector to measure the interference (alignment) signal. The actual designed PIC contains two of these systems on one PIC. Besides these two alignment sensor systems, several additional test structures are integrated on this PIC to analyze their performance.

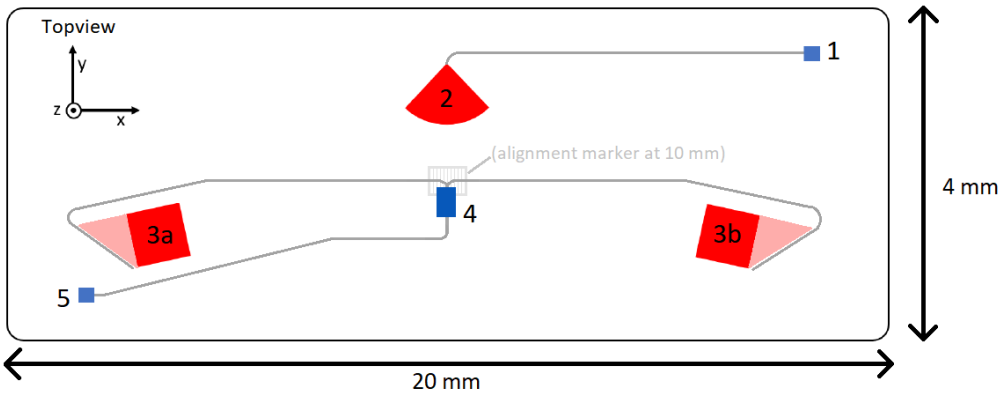

Figure 2.3: Schematic top view of the PIC alignment sensor system. The grey curves represent waveguides. Numbers 1 and 5 indicate, respectively, the standard IMOS input and output grating couplers (blue). Number 2 refers to the emitting grating coupler (red) and 3a and 3b represent the capturing grating couplers, consisting of the apodized rectangular grating coupler (red) and the gap coupler (pink). Number 4 indicates the beam combiner, which interferes the waveguide modes from both diffracted orders. The alignment marker grating is indicated in light grey and is positioned at the center of the PIC at a distance of 10 mm. Adapted from: [7]

2.2 Grating couplers

As explained in the previous section, grating couplers are the crucial element of the PIC alignment sensor prototype. The main function of the grating couplers is to provide the coupling between the PIC and free space. In general, light coupling into or out of a waveguide on a PIC can be achieved through multiple different methods. Transverse coupling, also called edge coupling or end-fire coupling, is one of these methods [19, 20]. In this method light is coupled into or out of a waveguide along the propagation direction. Therefore, this requires high optical quality facets, cleaved through the cross-sections of the waveguide, at the edges of the PIC [20]. However, in many cases the realization of these waveguide facets at the edges of the PIC is not possible or impractical. Consequently, vertical coupling, implying that light is coupled into or out of the waveguide from the top surface, is often required. For the IMOS platform, grating couplers are the most efficient building block for vertical light coupling. Grating couplers have the main advantage that their angular pattern of emission can be optimized, and that the coupling efficiency remains constant once the PIC is fabricated, since they are an integral part of the waveguide structure and the PIC design [19]. Furthermore, they can be used in high index waveguides, for which it is difficult to find suitable prism coupler materials, since the prism coupler material must have a larger index than the waveguide and superstrate [19]. Thus, grating couplers are used in the PIC prototype design to establish the coupling between the PIC and free space in multiple occasions. Firstly, the emitting grating coupler is used to produce a free space focusing Gaussian beam out of the PIC. Furthermore, two capturing grating couplers are used to capture the diffracted beams from free space with a grating coupler and to convert these captured slab modes into waveguide modes with a gap coupler. Thirdly, there are also standard IMOS grating couplers on the PIC alignment sensor prototype. These grating couplers are used to establish the fiber-to-chip (and vice versa) coupling to connect the PIC sensor to the external input and output. There is an important difference between the standard IMOS grating couplers and the emitting and capturing grating couplers. The standard IMOS grating couplers are uniform non-focusing grating couplers, whereas the emitting and capturing grating couplers are designed focusing grating couplers. Overall, grating couplers are the essential element for light coupling into and out of the PIC prototype

design, which is why this study focuses on grating couplers. This section will elaborate on the underlying physics of these photonic components and on their presence on the PIC alignment sensor prototype and the TU/e test PIC.

2.2.1 Phase matching condition

For vertical light coupling into or out of a waveguide, the wavevector components along the direction of propagation in the waveguide and in the beam need to be the same [19]. This results from Maxwell's boundary condition that the tangential electric field components should be continuous at the interface [21]. This condition is referred to as the general phase matching condition:

$$\beta = k_0 n_1 \sin(\theta) = \frac{2\pi}{\lambda_0} n_1 \sin(\theta). \tag{2.3}$$

In this equation β is the propagation constant, which is the wavevector component along the propagation direction, of the guided mode. λ_0 is the vacuum wavelength, n_1 the refractive index of the medium around the waveguide and θ is the angle at which the outcoupled beam propagates with respect to the normal of the waveguide surface. Since the guided mode condition states that $\beta > k_0 n_1$, the phase matching condition (equation 2.3) cannot be satisfied for guided modes. This implies that, conform the expectation, there is no outcoupling from an unperturbed guided mode. Nevertheless, there are multiple ways to allow for vertical light coupling into and out of a waveguide. As explained before, in the PIC prototype design this light outcoupling is initiated by grating couplers.

Grating couplers are defined as (periodic) variations of the refractive index of a waveguide structure. The refractive index variation is commonly created by partially etching the waveguide structure. Consider a uniform 2D grating coupler structure with a constant periodicity Λ for simplicity. The grating vector for such a structure is defined as [22]

$$\vec{K} = \frac{2\pi}{\Lambda}\hat{z}, \tag{2.4}$$

along the direction of periodicity, which is the propagation direction z in this case. As a result of the refractive index perturbation of the grating coupler structure, infinitely many diffracted orders are created. However, not all of these diffracted orders are real travelling waves out of the waveguide grating structure, as will become clear in the remainder of this elaboration. As mentioned before, for vertical light coupling to occur the wavevector components along the direction of propagation in the waveguide and in the beam need to be the same, which resulted in the phase matching condition of equation 2.3. Due to the perturbation induced by the grating structure, the phase matching condition for a grating coupler changes to equation 2.5 [20].

$$k_{m,z} = \beta - mK \qquad m = 0, \pm 1, \pm 2, ... \tag{2.5}$$

In this equation $k_{m,z}$ is the propagation constant of the diffracted orders m, where $m = 0, \pm 1, \pm 2, ...$ is again the diffraction order number. β is the propagation constant of the guided mode in the waveguide grating section and K is the grating vector, defined by equation 2.4. Equation 2.5 results in an infinite set of propagation constants for the diffracted waves due to the infinite number of diffracted orders m. However, similar as for the phase reflection grating of figure 2.1 only certain orders of this infinite set of spatial harmonics, also called Floquet-Bloch waves, are real travelling waves [22]. This is illustrated in the wave vector diagram of figure 2.4. The propagation constant of the guided mode in the waveguide grating section is defined by

$$\beta = n_{eff} k_0 = \frac{2\pi n_{eff}}{\lambda_0}, \tag{2.6}$$

where λ_0 and k_0 are respectively the vacuum wavelength and the vacuum wavevector. n_{eff} is the effective refractive index of the waveguide grating structure, which depends on multiple grating characteristics, such as period, groove width and etch depth [20]. The propagation constant of a diffracted wave travelling under an angle θ with respect to the x-axis is given by

$$k_z = k_1 \sin(\theta) = \frac{2\pi n_1}{\lambda_0} \sin(\theta), \tag{2.7}$$

where n_1 is the refractive index of the medium where the diffracted wave travels in. This equation implies that for real travelling diffracted waves, it must satisfy the condition that

$$|k_z| \leq \frac{2\pi}{\lambda_0} n_1. \tag{2.8}$$

Therefore, only the diffraction orders that satisfy both equations 2.5 and 2.8 are real travelling waves. It is even possible that the grating period Λ is so small, leading to a large grating vector (equation 2.4), that there is no diffraction order diffracted out of the waveguide. This phenomena is physically expected, since for very small grating periods, the grating merely acts as a perturbation of the refractive index [18]. Furthermore, this theoretical description shows that by increasing the grating period, and thereby decreasing the grating vector K, more diffracted orders will lead to outward travelling waves, meaning that the light is outcoupled under multiple different angles. Moreover, from this elaboration it also follows that if the grating period Λ is too small, no diffracted orders are coupled out of the waveguide, since the grating vector K is too large to fulfill the restriction of equation 2.8.

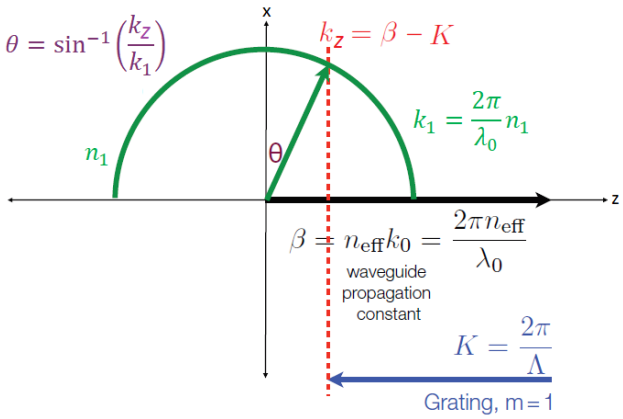

Figure 2.4: Wavevector diagram for a grating coupler. The wavevector of the diffracted orders is defined by equation 2.5. Only diffracted orders that have a wavevector within green half circle, defined by the refractive index of the surrounding medium n_1, result in real travelling waves out of the waveguide. Adapted from: [23]

Overall, substitution of equations 2.4, 2.6 and 2.7 into the phase matching condition (equation 2.5 finally results in:

$$\frac{2\pi}{\lambda_0} n_1 \sin(\theta_m) = \frac{2\pi}{\lambda_0} n_{eff} - m\frac{2\pi}{\Lambda}. \tag{2.9}$$

This equation can be simplified into the general phase matching condition between a free space beam travelling under an angle θ_m and the guided mode inside the grating, which is presented in equation 2.10.

$$n_1 \sin(\theta_m) = n_{eff} - m\frac{\lambda_0}{\Lambda} \tag{2.10}$$

Most diffraction grating couplers are limited to only the first diffraction order being coupled out of the waveguide, as that will generally provide the highest coupling efficiency [24, 25]. Having more diffracted orders would result in a loss of power. Moreover, equation 2.10 illustrates that the outcoupled angle θ of each grating line can be adjusted by changing its period Λ. Hence, by altering the period of each grating line in a certain manner, which is called apodization, the grating coupler can produce a diffracted beam that is focused into one point in free space. However, it has to be taken into account that the effective refractive index (n_{eff}) of the waveguide grating structure also changes when the grating period is altered [26]. This effect is often counteracted by simultaneously adapting the grating groove width of each grating element such that the effective refractive index remains constant. Hence, combining period apodization with a changing groove width significantly simplifies the design process of focusing grating couplers. Focusing grating couplers will be discussed in more detail in section 2.2.3.

2.2.2 Light coupling

The coupling between a free space beam and the waveguide mode inside the grating structure can be established if the phase matching condition for grating couplers, equation 2.10, is satisfied. Light in the waveguide will then be coupled out into the sub- and superstrate as diffracted orders, as illustrated in the left schematic diagram of figure 2.5. The angle at which the light is coupled out of a uniform grating structure, for each diffraction order m follows from equation 2.10 and is given by

$$\theta_m = \sin^{-1}\left(\frac{n_{eff} - m\frac{\lambda_0}{\Lambda}}{n_1}\right). \tag{2.11}$$

Again this equation implies that the diffraction orders are only real travelling waves under certain criteria, in this case the argument of the inverse sine function needs to be between -1 and +1. Equation 2.11 shows that the outcouple angle also depends on the refractive index of the medium the diffracted order is travelling in, given by n_1. Hence, when the sub- and superstrate have different refractive indices, the outcouple angles of the diffracted orders will be different. Furthermore, it depends on the grating period, the order number, the wavelength and the effective refractive index of the waveguide grating mode. Although the outcouple angles of the diffracted orders can be determined from the simple expression of equation 2.11, it does not provide enough information to construct the complete radiation pattern of a grating coupler. Moreover, this equation only holds for uniform grating couplers and as mentioned before, there is a specific interest in focusing grating couplers, which are apodized. For this reason radiation patterns of grating couplers, and especially focusing grating couplers, are conventionally determined through rigorous simulation methods.

Although the preceding elaboration focused on grating couplers as outcoupling devices, they can also be used as incoupling devices. The principles of light incoupling and outcoupling by grating couplers are illustrated in figure 2.5. The working principle of light incoupling is exactly equivalent to the outcoupling of light, because the grating coupler system is a reciprocal system [22, 27]. Thus, if the outcoupled diffracted beam is reversed to become the incident beam on the grating coupler structure, the light is coupled into the same waveguide mode, only travelling in the opposite direction compared to the outcoupler device. Moreover, because of this reciprocity the coupling efficiencies between two modes are the same for both incoupling and outcoupling if the wavefronts are identical. Another consequence of the reciprocity of the grating coupler device is that the ideal incouple angle, to obtain the highest coupling efficiency, can be determined from the outcoupled profile of a grating coupler. For this reason, simulations will be performed on the standard IMOS grating couplers in order to find the ideal incouple angle which is needed to couple a maximum amount of light into the PIC. This will be discussed in section 4.3.

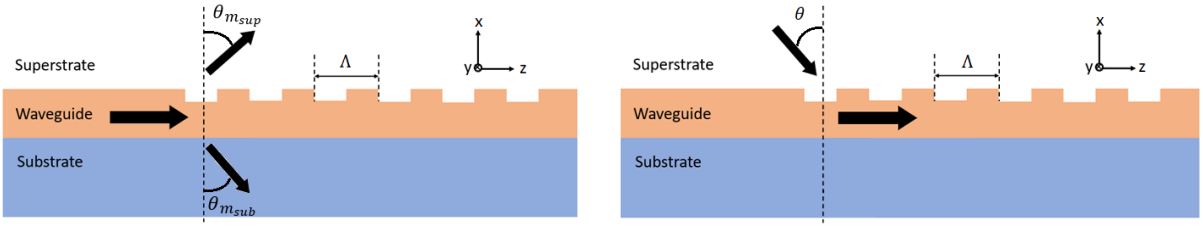

Figure 2.5: Uniform grating couplers as an outcoupler (a) and incoupler device (b). The black arrows indicate the directions of the light, θ refers to the respective angles and Λ refers to the constant grating period. Adapted from: [7]

2.2.3 Focusing grating couplers

As discussed before, for the application in the PIC alignment sensor, there is a specific interest in focusing grating couplers. The design process of 2D focusing grating couplers starts with a one-dimensional (1D) apodized focusing grating coupler. A Gaussian output beam can be achieved by varying the leakage factor (coupling strength) of the grating α along the direction of propagation (z), according to [28]

$$2\alpha(z) = \frac{G^2(z)}{1 - \int_0^z G^2(z')\,dz'}, \tag{2.12}$$

where $G(z)$ is a normalized Gaussian profile with the required beam diameter. It should be mentioned that equation 2.12 is only exact for long grating couplers with small leakage factors α. Consequently, the resulting design should be used as a starting point and further numerical optimization is required [28]. The $\alpha(z)$ profile can be tuned by adjusting the ratio between the length of the unetched part and the grating period, which is defined as the fill factor (FF). Therefore, focusing can be achieved by varying the grating period or the grating groove width. There are multiple methods to determine the required variation profile of the FF to achieve a certain α profile. Most design processes from the literature determine this relation between α and FF through numerical optimization methods based on multiple uniform gratings with different values for the FF [8, 29, 30]. However, the rigorous simulation methods that are used in this optimization process are computationally expensive for large area grating couplers, such as the ones on the PIC alignment sensor. The grating couplers on the PIC alignment sensor have

such large dimensions due to the relatively large required focusing distance of 10 mm, as mentioned in section 2.1. Still, there are a few (quasi) analytic models that provide an approximate expression for this relation, such as the works of Tamir and Peng [31] and Ogawa et al. [32] [8]. These expressions are used to determine the required apodization profile of the large area grating couplers on the current PIC alignment sensor prototype. However, for these specific large area capturing and emitting grating couplers Ogawa's method might result in functionality errors, since the method is based on single material gratings, whereas the capturing and emitting grating couplers are compound gratings [18]. Moreover, the Tamir method also has its deficiency, since this model is based on the assumption that the maximum α factor is always achieved at a FF of 0.5, which is not always the case [18]. Thus, it is rather questionable if these approximate expressions will result in correct functionality of the capturing and emitting grating couplers and experimental measurements should verify this. Hence, the numerical optimization methods are still desired for these large area grating couplers.

Yet, grating apodization will only result in focusing of the beam in one direction. In order to achieve focusing in the transverse direction, the apodized grating grooves should be curved [20]. The required curvature of the grating grooves can be calculated through interferometric approaches in which the desired phase profile on the surface of the grating coupler is interfered with the guided mode propagating in the waveguide grating section [18]. There are multiple methods available in the literature to determine the desired phase profile on the surface of the grating coupler. For example, Oton [33] calculates the phase profile at the surface by taking the desired focus point as a diverging Gaussian beam with the focus at the defined location in space, whereas in the work of Chen et al. [34] the focus is taken as a point source radiating into all directions [18]. The disadvantages of these interferometric approaches is that they do not allow for modifications of the field profiles while propagating through the grating waveguide section and that it does not account for high index contrast effects [29]. The resulting curved apodized grating coupler structures, for which an example is provided in figure 2.6, still rely on further numerical optimization as also mentioned before [26,28]. Hence, numerical optimization is used in multiple steps of the design process, hereby highlighting the importance of this process. The rigorous FDTD method is the conventional method to perform this numerical parameter optimization. Although FDTD simulations are accurate, their main drawback is their computational burden, especially for these large area grating couplers that are required in the PIC alignment sensor application. Other more efficient alternatives to perform the parameter optimization are coupled mode theory (CMT) and the mode matching method (MMM) [35]. Also these methods have their limitations, as the CMT method is unsuitable for large refractive index contrast problems and the MMM is only applicable to weak radiation structures [35]. Therefore, there is a strong demand for analytic models that are able to accurately determine radiation profiles of such large area grating couplers, so that they can be used in the design optimization process of the grating couplers. The recent developments from Xu et al. [35], who showed promising results for designing focusing grating couplers with an efficient complex mode matching method (CMMM), are a confirmation of the ongoing research in this area.

2.2.4 Grating couplers on the PICs

PIC alignment sensor prototype

As described before, grating couplers are the essential elements in the PIC alignment sensor prototype design. The standard IMOS grating couplers are simple uniform rectangular grating couplers, since there is no focusing required to achieve the coupling between free space and PIC. For the emitting grating coupler, which is schematically illustrated on a small scale in figure 2.6, the 2D focusing is achieved by curving the grating lines of a 1D apodized grating. The taper underneath the emitting grating coupler expands with such a large angle that the mode out of the waveguide is freely expanding into the taper. The required curvature of the grating grooves is calculated with the interferometric approach discussed in the previous subsection. For more details on the design of the emitting grating coupler a reference is made to the thesis of A.E.C. van den Bosch [18] in which this is extensively discussed. As mentioned before, the capturing grating couplers consist of an apodized rectangular grating coupler to convert the free space beam to a slab mode and a gap coupler to convert the slab mode into a waveguide mode. This configuration is schematically illustrated in figure 2.3, indicated by the numbers 3a and 3b. In this schematic, the red part refers to the apodized rectangular grating coupler, the pink part refers to the gap coupler and the grey curve is the waveguide. The apodized rectangular grating has period adjustments in one direction, therefore it also provides focusing in one direction. Hence, this part of the capturing grating coupler produces a guided slab mode. The guided slab mode is converted into a 400 nm wide

waveguide mode by a so called gap coupler. The gap coupler is based on frustrated total internal reflection (FTIR) and couples light from the slab mode to the waveguide by terminating the slab as a triangle and positioning a waveguide close to the edge of the slab [8]. The slab mode is reflected at the edge of the slab, where the evanescent field will penetrate and couple into the waveguide. The slab mode to waveguide mode conversion could also be achieved with tapers. However, a width conversion from hundreds of micron to 400 nm would require a taper length of multiple millimeters, which results in undesirable large footprint. Therefore, a gap coupler is used to provide this conversion from slab mode to waveguide mode. In order to have this conversion as efficient as possible, gap distance and waveguide width variations are applied to the gap coupler. This is extensively discussed in the thesis of J.P. de Graaf [8]. Thus, by combining the gap coupler with the 1D focusing grating coupler the conversion of the free space beam to a waveguide mode is made in both directions.

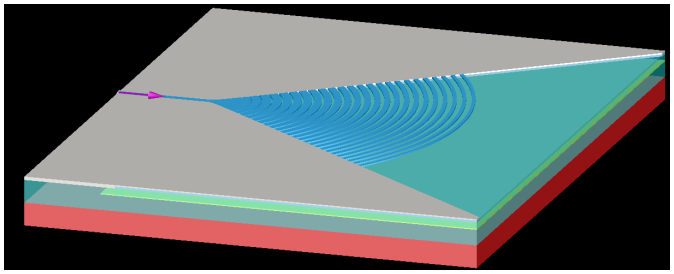

Figure 2.6: Small scale schematic illustration of the design of the 2D focusing emitting grating coupler. The arrow indicates the incoming guided mode and the darker blue lines in the light blue area indicate the curved apodized grating lines to create the 2D focusing beam. The light blue area indicates the wide-angled taper in which the guided mode expands freely. Adapted from: [18]

TU/e test PIC

As mentioned in chapter 1, a test PIC is provided by the TU/e to experimentally measure the beam profiles out of large grating couplers. This will not only demonstrate correct operation of the experimental setup, it will also provide data for experimental comparison of the analytic model. The test PIC of the TU/e contains the design of Y. Wang, in which multiple long grating couplers (antennas) are designed [36]. These structures are actually used as optical beam steerers as explained in the paper [36]. However, for the purpose of this research project the sole interest is in the measurement of the far field beam profiles of these large grating couplers. Hence, it is out of the scope of this project to discuss all the details of the designs and functionalities of these large grating couplers, and the reader is referred to the paper of Y. Wang for this [36]. Figure 2.7 provides a schematic illustration of the large grating coupler structures. The light is coupled in at the standard IMOS grating coupler (blue), travels through the waveguide (light grey) and is converted from a 400 nm wide waveguide mode into a 15 µm wide waveguide mode by a taper (dark grey). Although the standard IMOS grating couplers on this test PIC are different from the ones on the PIC alignment sensor prototype (curved versus straight grating lines respectively), they have the same purpose of providing coupling between the PIC and free space. The waveguide mode then enters the large uniform grating coupler (red). There are multiple different variations of the large grating couplers fabricated, more details on the measured large grating couplers are included with the results in chapter 6. The light that is not coupled out by the large grating coupler is again tapered down and coupled out of the PIC by a standard IMOS grating coupler.

Figure 2.7: Schematic illustration of the large grating coupler structures on the TU/e test PIC. It consists of two standard IMOS grating couplers at the input and output (blue), which are connected to waveguides (light grey). The guided mode is expanded into the large grating coupler (red) through a taper (dark grey).

Chapter 3

Born Approximation applied to computation of Grating Coupler Emission (BA-GCE) model

The importance of the grating coupler components for the PIC alignment sensor design has been discussed in the previous chapter. Due to the large footprints of the emitting and capturing grating couplers, conventional rigorous simulation methods like Lumerical FDTD [9] are too computationally expensive to simulate these structures on full scale. However, an accurate simulation method is desired for in the design optimization process of these components. Thus, alternative ways of simulating radiation profiles of large area grating couplers are demanded. For this reason, an analytic model has been developed, which is able to accurately determine electric fields and radiation profiles of grating couplers of any size. The developed grating coupler model is based on a paper of C.A. Flory [1]. The physical principles of this "Flory model" will be elaborated in section 3.1. Subsequently, multiple adaptations and extensions have been made to this model in order to improve it and to extend its application range and options. These adaptations and extensions will be discussed individually in section 3.2. Finally, all the adaptations and extensions to the model will be combined to develop the novel BA-GCE model which can be used to accurately determine emission profiles of grating couplers of any size. This section will also highlight the approximations that are made in this model, as well as the limitations that arise from these approximations.

3.1 Flory model [1]

The physical reasoning behind the Flory model, which is a 2D model, is illustrated in figure 3.1. The grating coupler is modelled as an unperturbed homogeneous slab waveguide plus the dielectric constant (or refractive index) perturbation introduced by the grating structure. A perturbative technique, called the volume current method (VCM), is then used to calculate the scattered radiation due to this refractive index perturbation of the grating grooves. In this technique the scattering effect of each grating groove is modelled by a collection of point sources. Hence, each grating groove will radiate light from the waveguide mode into the sub- and superstrate as if it were a collection of point sources. The radiation that is emitted from each point source is described by the Green's function. All these point sources together make up the radiated Poynting vector. In order to end up with an analytic expression for the radiated Poynting vector in terms of the waveguide and grating parameters, two approximations are applied: the first order Born approximation and the far field approximation. As a consequence of these approximations, the model is only accurate in a limited range of grating parameters. Section 3.3 will provide more details on the limitations of the final model. First, the mathematical derivation of the model will be elaborated, based on the physics described above. Since not all the mathematical calculations will be provided, a reference is made to the paper for the complete derivation [1].

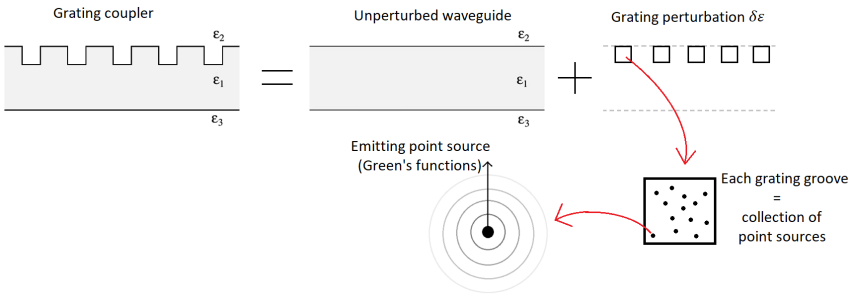

Figure 3.1: Schematic summary of the physical reasoning behind the Flory model [1]. The grating coupler is modelled as an unperturbed waveguide plus the dielectric constant perturbation introduced by the grating structure. Then, each grating groove perturbation is modelled as a collection of point sources that emit radiation described by the Green's function.

In order to calculate the emitted field from a grating coupler, the famous Maxwell equations have to be solved. For fields with a harmonic time dependence of $e^{i\omega t}$, and no externally applied currents, the two Maxwell curl equations can be simplified into equations 3.1 and 3.2 [21].

$$\vec{\nabla} \times \vec{E} = i\omega\vec{B} \tag{3.1}$$

$$\vec{\nabla} \times \vec{H} = -i\omega\epsilon_0\epsilon_r\left(\vec{r}\right)\vec{E} \tag{3.2}$$

In these equations $\vec{E}$ and $\vec{H}$ are respectively the electric and magnetic fields, ω is the field angular frequency and $\epsilon_r(\vec{r})$ is the position dependent dielectric constant. If it is then assumed that the waveguide grating structure is embedded into a background medium with dielectric constant ϵ_2, the position dependent dielectric constant can be defined by

$$\epsilon_r\left(\vec{r}\right) = \epsilon_2 + \delta\epsilon_r\left(\vec{r}\right), \tag{3.3}$$

where the dielectric perturbation induced by the grating structure is defined as $\delta\epsilon_r\left(\vec{r}\right)$. In the VCM method, the effect of this dielectric perturbation is represented by an equivalent volume polarization current density which acts as a source for the radiated field [1, 37]. The equivalent polarization current density ($\vec{J}_P$) is defined in terms of the dielectric perturbation $\delta\epsilon_r\left(\vec{r}\right)$ by equation 3.4.

$$\vec{J}_P = i\omega\epsilon_0\delta\epsilon_r\left(\vec{r}\right)\vec{E} \tag{3.4}$$

Substitution of equations 3.3 and 3.4 into equation 3.2 then results in

$$\vec{\nabla} \times \vec{H} + i\omega\epsilon_0\epsilon_2\vec{E} = -\vec{J}_P. \tag{3.5}$$

Subsequently, the vector and scalar potentials, respectively ϕ and $\vec{A}$, are introduced through their relations with the fields, which are given by equations 3.6 and 3.7.

$$\vec{E} = -\vec{\nabla}\phi + i\omega\vec{A} \tag{3.6}$$

$$\vec{B} = \vec{\nabla} \times \vec{A} \tag{3.7}$$

Then, if it is assumed that the medium is nonmagnetic ($\vec{B} = \mu_0\vec{H}$), substitution of equations 3.6 and 3.7 into equation 3.5 leads to

$$\vec{\nabla} \times \left(\vec{\nabla} \times \vec{A}\right) + i\omega\mu_0\epsilon_0\epsilon_2\left(-\vec{\nabla}\phi - \frac{\partial\vec{A}}{\partial t}\right) = -\mu_0\vec{J}_P. \tag{3.8}$$

After using the vector identity $\vec{\nabla} \times \left(\vec{\nabla} \times \vec{A}\right) = \vec{\nabla}\left(\vec{\nabla} \cdot \vec{A}\right) - \nabla^2\vec{A}$ and applying the definition of the Lorenz gauge [38, 39], equation 3.8 results in the Helmholtz equation for the vector potential:

$$\left(\nabla^2 + \omega^2\mu_0\epsilon_0\epsilon_2\right)\vec{A} = \mu_0\vec{J}_P. \tag{3.9}$$

Equation 3.9 thus describes the vector potential of the radiated field due to the grating perturbation ($\delta\epsilon_r\left(\vec{r}\right)$), which is hidden in the polarization current density $\vec{J}_P$. The general solution for this equation

consists of a homogeneous solution and a particular solution. This general solution for the vector potential $\vec{A}$ can be expressed in integral form in terms of a Green's function, leading to equation 3.10.

$$\vec{A}\left(\vec{r}\right) = \mu_0 \int G\left(\vec{r} - \vec{r}\,'\right) \vec{J}_P\left(\vec{r}\,'\right) d^3\vec{r}\,' \tag{3.10}$$

In this equation $G\left(\vec{r} - \vec{r}\,'\right)$ is the appropriate Green's function for the Helmholtz equation 3.9. The appropriate Green's function is found by solving the homogeneous equation of equation 3.9 with a point source as source term. For the 2D Helmholtz equation, the Green's function in free space is given by [40]

$$G\left(\vec{r} - \vec{r}\,'\right) = -\frac{i}{4} H_0^{(1)}\left(k|\vec{r} - \vec{r}\,'|\right). \tag{3.11}$$

In this equation $H_0^{(1)}$ is the zeroth order Hankel function of the first kind, $\vec{r}$ is the distance vector in the propagation direction with respect to the origin and $k = \sqrt{\epsilon_2} k_0$ is the wavenumber. As indicated in figure 3.2, the origin is defined at the center of the waveguide (x = 0) and at $-z_0$ from the start of the first grating groove. In order to simplify the expression for the Green's function, the far field approximation is applied. The next chapter will provide an analysis of the distance at which this far field approximation is applicable. In the far field limit, the leading term of equation 3.11 takes the form [40]

$$G\left(\vec{r} - \vec{r}\,'\right) \to -\frac{i}{4} e^{-i\frac{\pi}{4}} \sqrt{\frac{2}{\pi k r}} e^{ikr} e^{-ik\hat{r}\cdot\vec{r}\,'}. \tag{3.12}$$

Moreover, the effective dielectric perturbation that is induced by the grating coupler in figure 3.2 is described by

$$\delta\epsilon\left(\vec{r}\right) = -\left(\epsilon_1 - \epsilon_2\right) f\left(\vec{r}\right), \tag{3.13}$$

where $f(\vec{r})$ is 1 in the area of the grating grooves and 0 everywhere else. Substitution of this dielectric perturbation in equation 3.4 yields the induced equivalent polarization current density:

$$\vec{J}_P = -i\omega\epsilon_0\left(\epsilon_1 - \epsilon_2\right) f\left(\vec{r}\right) \vec{E}\left(\vec{r}\right). \tag{3.14}$$

In this equation $\vec{E}$ refers to the electric field in the waveguide grating region. However, in order to circumvent the complex problem of determining the electric field in the waveguide grating region, the first order Born approximation is applied. Therefore, the electric field is approximated by the expression of the electric field of the lowest order TE mode in the unperturbed symmetric slab waveguide. This electric field expression for lowest order TE mode in the unperturbed symmetric slab waveguide is straightforwardly calculated in photonics books, like [41], resulting in:

$$E_y = E_0 \frac{\cos\left(\kappa x\right)}{\cos\left(\frac{\kappa h}{2}\right)} e^{i\beta z}. \tag{3.15}$$

In this equation E_0 is the electric field amplitude at the dielectric interfaces of the waveguide, κ is the wavevector in the waveguide layer and β is the propagation constant of the waveguide mode. Eventually substitution of this expression for the electric field into equation 3.14 and afterwards substituting this equation, as well as equation 3.12, into equation 3.10, results in:

$$A_y\left(\vec{r}\right) = -\frac{\mu_0\omega\epsilon_0\left(\epsilon_1 - \epsilon_2\right) E_0}{4\cos\left(\frac{\kappa h}{2}\right)} \sqrt{\frac{2}{\pi k r}} e^{-\frac{i\pi}{4}} e^{ikr} \int_{grooves} \cos\left(\kappa x\,'\right) e^{-ik\hat{r}\cdot\vec{r}\,'} e^{i\beta z\,'} d^2\vec{r}\,'. \tag{3.16}$$

Equation 3.16 is the integral form of the general solution for the radiated vector potential resulting from the grating perturbation. This expression is calculated for the system configuration illustrated in figure 3.2, which also includes the definitions of the parameters. ϵ_1 refers to the dielectric constant of the waveguide material and ϵ_2 refers to the dielectric constant of the medium in the grating grooves, in this case the superstrate. The other symbols in equation 3.16 are either the conventional physical constants or refer to the same parameters as introduced before. The x and z components of the radiated vector potential are both zero, because the electric field of the lowest order TE mode in the unperturbed waveguide only has a y component. Furthermore, since there is only a dielectric perturbation in the grating groove regions, the integral in equation 3.16 is only over the 2D cross-sectional areas of these grooves.

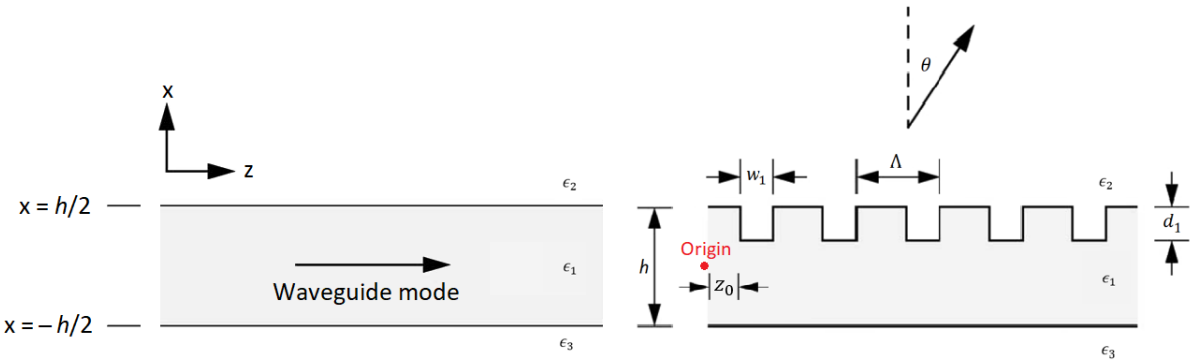

Figure 3.2: Configuration of the Flory model, with the unperturbed planar slab waveguide on the left and the grating coupler with symbol definitions on the right. The red dot refers to the origin of the coordinate system that is used in the Flory calculation. Adapted from: [1]

The integral in equation 3.16, over the cross-sectional areas of the grating grooves, can then be solved by introducing the angle θ defined as in figure 3.2. The dot product in the exponential can then be evaluated as $\hat{r} \cdot \vec{r}\,' = x' \cos(\theta) + z' \sin(\theta)$. Therefore, the integration over the 2D cross-sectional areas of the grating grooves can be factored out into an x-dependent part and a z-dependent part. For a constant etch depth d_1, the x-integral over the grooves runs from $\frac{h}{2}$–d_1 to $\frac{h}{2}$. Thus, the integration of equation 3.16 can be rewritten into equation 3.17.

$$\int_{grooves} \cos(\kappa x')e^{-ik\hat{r}\cdot\vec{r}\,'}e^{i\beta z'}d^2\vec{r}\,' = \int_{\frac{h}{2}-d_1}^{\frac{h}{2}} \cos(\kappa x')e^{-ikx'\cos(\theta)}dx' \int_{grooves} e^{iz'(\beta - k\sin(\theta))}dz' \tag{3.17}$$

The integration over the height direction (x) and the length direction (z) can be calculated separately. More details behind this mathematical calculation are provided in the paper of Flory [1]. The integration over the height direction depends on the height of the waveguide h and the depth of the grating grooves d_1 and results in the factor $\mathcal{D}$. The integration over the length direction is split into two terms: the grating element factor $\mathcal{E}$ considering one single grating groove and the grating array factor $\mathcal{A}$ considering the periodicity of the grating structure. The element factor depends on the width of the grating grooves w_1, whereas the array factor depends on the grating period Λ and the number of grating elements N. Finally, this extensive mathematical derivation, explained in the paper of Flory [1], results in the following solution for the radiated vector potential:

$$A_y(\vec{r}) = -\frac{\mu_0\omega\epsilon_0(\epsilon_1 - \epsilon_2)E_0}{4\cos\left(\frac{\kappa h}{2}\right)}\sqrt{\frac{2}{\pi kr}}e^{-\frac{i\pi}{4}}e^{ikr}e^{iz_0(\beta - k\sin(\theta))}\mathcal{A}\mathcal{D}\mathcal{E}. \tag{3.18}$$

The solution of the height integral for this case is

$$\mathcal{D} = \frac{d_1}{2}\left(e^{i\frac{(h-d_1)}{2}(\kappa - k\cos(\theta))}\frac{\sin\left(\frac{d_1}{2}(\kappa - k\cos(\theta))\right)}{\left(\frac{d_1}{2}(\kappa - k\cos(\theta))\right)} + e^{-i\frac{(h-d_1)}{2}(\kappa + k\cos(\theta))}\frac{\sin\left(\frac{d_1}{2}(\kappa + k\cos(\theta))\right)}{\left(\frac{d_1}{2}(\kappa + k\cos(\theta))\right)}\right). \tag{3.19}$$

The grating element factor is evaluated as

$$\mathcal{E} = w_1 e^{i\frac{w_1}{2}(\beta - k\sin(\theta))}\mathrm{sinc}\left(\frac{w_1}{2}(\beta - k\sin(\theta))\right). \tag{3.20}$$

Lastly, the grating array factor for this case is given by

$$\mathcal{A} = e^{i\frac{(N-1)}{2}\Lambda(\beta - k\sin(\theta))}\frac{\sin\left(N\frac{\Lambda}{2}(\beta - k\sin(\theta))\right)}{\sin\left(\frac{\Lambda}{2}(\beta - k\sin(\theta))\right)}. \tag{3.21}$$

The final step is to compute an expression for the radiated Poynting vector $\vec{S}$. As calculated by C.A. Flory [1], the far field limits of the radiated fields in terms of the radiated vector potential $\vec{A}$ are given by equations 3.22 and 3.23, where $\hat{r}$ refers to the unit vector in the direction of the radiated field.

$$\vec{E} = -i\omega\hat{r} \times \left(\hat{r} \times \vec{A}\right) \tag{3.22}$$

$$\vec{H} = i\omega\sqrt{\frac{\epsilon_2}{\mu_0}}\left(\hat{r} \times \vec{A}\right) \tag{3.23}$$

Substitution of these far field limits into the definition of the time-averaged Poynting vector ($\vec{S} = \frac{1}{2}\mathrm{Re}\left[\vec{E} \times \vec{H}^*\right]$) and working out the cross-products by using vector identities eventually yields

$$\vec{S} = \frac{\omega^2}{2}\sqrt{\frac{\epsilon_2}{\mu_0}}\left|\hat{r} \times \vec{A}\right|^2 \hat{r}. \tag{3.24}$$

Note that in this thesis, the radiated Poynting vector actually refers to the time-averaged radiated Poynting vector. Finally, equation 3.18 for the radiated vector potential can be substituted into equation 3.24 to arrive at the expression for the radiated Poynting vector in the far field limit:

$$\vec{S} = \frac{\mu_0 \omega^3 \epsilon_0^2 \left(\epsilon_1 - \epsilon_2\right)^2 E_0^2}{16\pi \cos^2\left(\frac{\kappa h}{2}\right) r} |\mathcal{A}|^2 |\mathcal{D}|^2 |\mathcal{E}|^2 \hat{r}. \tag{3.25}$$

This Flory model serves as the foundation for the novel BA-GCA model, which is developed by improving and extending the Flory model. These applied adaptations and extensions are discussed in the next section.

3.2 Adaptations and extensions to Flory model

The Flory model that is explained in the previous section is constructed for uniform grating couplers in symmetric waveguide structures. Therefore, in this section the model will be extended to grating couplers with apodized periods and for asymmetric waveguide structures. As explained in the previous chapter the emitting and capturing grating couplers are apodized grating couplers to achieve the focusing of light. Hence, it is in the interest of this research project to include these extension options in the model. Furthermore, the Flory model assumes that the electric field amplitude in the waveguide E_0 remains constant over the complete grating structure. However, since light is outcoupled from the waveguide mode into the sub- and superstrate, the light intensity, and thereby the electric field amplitude, decreases over distance in the waveguide structure. Hence, the model can be improved by taking into account this decrease in light intensity in the waveguide. In this section, these adaptations and extensions to the Flory model will be discussed individually.

3.2.1 Exponential decay of light intensity in the waveguide

Due to the outcoupling of light by the grating coupler, the electric field amplitude will decrease over distance along the propagation direction. In the Flory model, a constant electric field amplitude E_0 is used over the complete grating coupler structure. In reality the power loss per unit length of the waveguide mode scales with the radiated power. It follows from equation 3.25 that this radiated power is proportional to E_0^2, therefore it is also proportional to the power in the waveguide mode. Thus, since the power loss per unit length is proportional to the power in the waveguide mode itself, it directly implies an exponential decrease of the light intensity (power) in the waveguide over distance along the propagation direction (z). This exponential relation is also supported by the literature [20]. Hence, in this section an expression is derived for the light intensity loss per grating element in order to incorporate the exponential decay of the light intensity in the waveguide into the model.

The expected exponential decay of light can be calculated by applying the Poynting theorem to the grating coupler. Poynting's theorem states that for a certain volume:

$$\frac{\partial U}{\partial t} + \nabla \cdot \vec{S} = -\vec{J} \cdot \vec{E}. \tag{3.26}$$

In this equation $\frac{\partial U}{\partial t}$ refers to the energy density as function of time, which is equal to zero, since a stable situation is considered in this case. Moreover, there is no macroscopic current in the grating coupler, so $\vec{J} = 0$. Thus, if a slice of the grating coupler is considered, the volume integral over the divergence of the Poynting vector $\vec{S}$ should be equal to 0. By using the divergence theorem, the volume integral can be converted into a surface integral, leading to

$$\iiint_{slice} \left(\nabla \cdot \vec{S}\right)\, d^3\vec{r} = \oiint_{slice\ surface} \vec{S} \cdot d^2\vec{r} = 0. \tag{3.27}$$

Then, if equation 3.27 is applied to the integration surface illustrated in figure 3.3, it results in

$$\oiint_{slice\ surface} \vec{S} \cdot d^2\vec{r} = -\int_{-\frac{h}{2}}^{\frac{h}{2}} S_{in}\, dx + \int_{-\frac{h}{2}}^{\frac{h}{2}} S_{out}\, dx + \int_{top} S_{sup} \cdot r d\theta + \int_{bottom} S_{sub} \cdot r d\theta = 0. \tag{3.28}$$

As can be seen from the dimensions of both sides of the equation, the third dimension (width) is ignored in this step, since it is a 2D model. The incoming Poynting vector can be calculated from the electric and magnetic fields for the unperturbed waveguide structure as

$$\vec{S}_{in} = \frac{1}{2}\mathrm{Re}\left[\vec{E}_{waveguide} \times \vec{H}^*_{waveguide}\right]. \tag{3.29}$$

Substitution of the final expression for $\vec{S}_{in}$ into the integral of equation 3.28 leads to a closed expression from which a numerical value can be obtained for specific grating coupler parameters. The result of this integral is referred to as $I_{S_{in}}$. Integration over the half circular top and bottom sides of the integration surface will also result in a closed expression from which a numerical value can be obtained, which is referred to as $I_{S_{sup}}$ and $I_{S_{sub}}$ for respectively the radiated intensity into the super- and substrate. For this calculation the radiated Poynting vector for a single grating element is used, which is given by equation 3.25 with an array factor $\mathcal{A}$ of 1. Hence, the assumption is made that all the light that is outcoupled from the grating coupler will reach the far field.

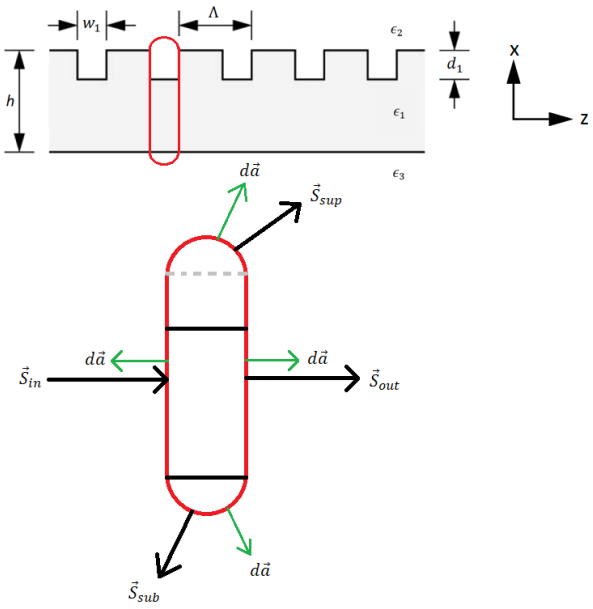

Figure 3.3: Integration surface of the grating coupler to which the Poynting theorem is applied. Adapted from: [1]

Since numerical values can be obtained for three of the four integrals of equation 3.28, the integrated outgoing Poynting vector can be calculated. By comparing this with the integrated intensity of the incoming Poynting vector, the exponential loss factor of the light intensity over one grating element can be determined. The expression for this F_{loss} factor is provided in equation 3.30.

$$F_{loss} \equiv \frac{I_{S_{sub}} + I_{S_{sup}}}{I_{S_{in}}} \tag{3.30}$$

Grating grooves with the same width therefore result in the same loss factor. As a result of this exponential decay factor, the electric field amplitude is not constant anymore but has changed according to:

$$E_0 \rightarrow (1\text{–}F_{loss})^{\frac{z}{2w_1}}\, E_0 \tag{3.31}$$

In this expression, z refers to the distance along the grating when the non-radiating (unetched) parts are ignored. The additional factor of 2 is introduced due to the proportionality relation between the intensity and the squared electric field. Furthermore, this calculation assumes a constant width of the grating grooves and ignores the unetched parts of the grating coupler structure. Conclusively, by correcting this change of the electric field amplitude for the unetched parts it can be readily implemented into the Flory model calculations, to include the exponential decay of the light intensity in the waveguide due to light outcoupling.

3.2.2 Period apodization

As discussed before, when focusing grating couplers are desired, the FF has to be adjusted. This can be achieved by period apodization of the grating coupler structure. This period apodization can also be included in the Flory model, as will be shown in this section. It is important to mention that this extension option for period apodization assumes a constant width of the grating grooves w_1. It should be possible to extend this option to allow for apodized grating groove widths as well, however that would change the complete calculation. It would make the calculations for $\mathcal{A}$, $\mathcal{E}$, and especially the calculation of the F_{loss} factor, significantly more complex, thereby complicating the process of finding analytic and intuitive formulas for these terms. For this reason, only the period of each grating element Λ is varied in this extension option for now.

The grating array factor $\mathcal{A}$ is the only factor in the expression for the radiated Poynting vector that is influenced by a varying grating period Λ. It can be derived that a varying period will result in the following expression for the grating array factor:

$$\mathcal{A} = \sum_{n=0}^{(N-1)} \left(\prod_{m=1}^{n} e^{i\Lambda_m(\beta - k\sin(\theta))} \right). \tag{3.32}$$

In this equation Λ_m is the period of the m^{th} grating element. As elaborated in section 3.1, the z-integral of equation 3.17 is an integral over phase factors depending on the position along the grating coupler (z). This integral is then split into an array factor $\mathcal{A}$ and an element factor $\mathcal{E}$. Since the width is assumed to be constant, $\mathcal{E}$ remains unchanged. However, a change in the period of an individual grating element will change the z-position of all the grating elements at larger z-positions. Therefore, the $\mathcal{A}$ factor is a sum of products, since the z-position of each individual grating element depends on the periods of all the grating elements before that. In case the grating periods are constant, equation 3.32 simplifies to the grating array factor defined by Flory (equation 3.21). In case that the grating periods vary linearly over distance along the grating coupler ($\Lambda_m = \Lambda_1 + \Delta\Lambda \cdot z$), the expression for the grating array factor can be simplified into

$$\mathcal{A} = \sum_{n=0}^{(N-1)} e^{i(\beta - k\sin(\theta))\left(n\cdot\Lambda_1 + \frac{1}{2}n(n-1)\cdot\Delta\Lambda\right)}. \tag{3.33}$$

3.2.3 Asymmetric waveguide

The Flory model is not applicable to grating couplers that have different materials as substrate and superstrate, since the Flory model is based on an unperturbed symmetric waveguide. By converting the calculations of Flory to an asymmetric waveguide, the model can be generalized to be applicable to asymmetric as well as to symmetric waveguide structures.

As a result of the change from a symmetric to an asymmetric waveguide structure, the electric field in the waveguide is changed. The field calculations have to be performed on an asymmetric planar slab waveguides instead. Hence, the field expression used in the first order Born approximation will change to this field expression for the asymmetric planar slab waveguide. The electric field expression for the asymmetric planar slab waveguide can be obtained from textbook calculations, such as in Photonic Devices by J.M. Liu [42]. The final result for the electric field of the first order TE mode in such an unperturbed asymmetric planar slab waveguide is

$$E_y = \begin{cases} E_0 \cos\left(\frac{\kappa h}{2} - \phi\right) e^{-\gamma_2\left(x - \frac{h}{2}\right)} e^{i\beta z} & x \geq \frac{h}{2} \\ E_0 \cos(\kappa x - \phi) e^{i\beta z} & -\frac{h}{2} \leq x \leq \frac{h}{2} \\ E_0 \cos\left(\frac{\kappa h}{2} + \phi\right) e^{\gamma_3\left(x + \frac{h}{2}\right)} e^{i\beta z} & x \leq -\frac{h}{2} \end{cases}. \tag{3.34}$$

In these expressions E_0 now is the maximum electric field amplitude, whereas it referred to the electric field amplitude at the dielectric interfaces in Flory's calculation for the symmetric planar slab waveguide. Furthermore, κ is again the transverse wavevector component in the waveguide layer and γ_2 and γ_3 are the decay constants in respectively the super- and substrate. The values of the phase factor ϕ and the other three constants can be calculated by a numerical root calculations with their mathematical definitions, also including the propagation constant β, and the two eigenvalue equations 3.35 and 3.36.

$$\tan(\kappa h) = \frac{\kappa(\gamma_2 + \gamma_3)}{\kappa^2 + \gamma_2\gamma_3} \tag{3.35}$$

$$\tan(2\phi) = \frac{\kappa(\gamma_3 + \gamma_2)}{\kappa^2 + \gamma_2\gamma_3} \tag{3.36}$$

Thus, as a result of this change to an asymmetric structure the calculation of the values for the constants κ and β will change, which are both prominently present in the expressions for the radiated Poynting vector and its script factors. In addition, the change in electric field expression influences the results of the x-integral $\mathcal{D}$. Recalculation of this integral with the new electric field expression results in

$$\mathcal{D} = \frac{d_1}{2}\left(e^{i\frac{(h-d_1)}{2}(\kappa - k\cos(\theta)) - i\phi}\frac{\sin\left(\frac{d_1}{2}(\kappa - k\cos(\theta))\right)}{\frac{d_1}{2}(\kappa - k\cos(\theta))} + e^{-i\frac{(h-d_1)}{2}(\kappa + k\cos(\theta)) + i\phi}\frac{\sin\left(\frac{d_1}{2}(\kappa + k\cos(\theta))\right)}{\frac{d_1}{2}(\kappa + k\cos(\theta))}\right). \tag{3.37}$$

In this equation the symbols refer to the same properties as introduced before.

Besides the two changes discussed above, another consequence of the change to an asymmetric structure is that the calculations for the radiated light into the substrate and into the superstrate need to be seperated, because the wavevector k has different values in these two regions. Furthermore, as mentioned above, the definition of the constant E_0 has also changed in the new electric field calculation for the asymmetric slab waveguide. This definition of E_0, as the maximum electric field amplitude coincides, with the definition for the electric field amplitude in the Lumerical FDTD [9] simulations later on. Since the asymmetric field calculation is also applicable to the symmetric slab waveguide structure, this calculation is also used for the Flory results later on, in order to correct for the difference in scaling factor of the electric field amplitude compared to Lumerical FDTD. More importantly, this extension allows for an additional option to calculate radiated fields of grating couplers with asymmetric waveguide structures, which is not possible with Flory's model.

3.2.4 Radiated electric field

The final extension of the Flory model is the most straightforward, because a large part of the derivation is already provided in the paper of Flory [1]. This extension finally leads to a formula to determine the radiated electric field at a certain distance above the grating coupler. It is important in the PIC alignment sensor application to determine the electric field profiles of the grating couplers at the alignment mark, which is at 10 mm from the PIC. Hence, this extension is particularly useful for that purpose.

Flory already provides the expression for the radiated electric field $\vec{E}$ in the far field approximation as function of the vector potential $\vec{A}$, as shown in equation 3.38.

$$\vec{E} = -i\omega\hat{r} \times \left(\hat{r} \times \vec{A}\right) \tag{3.38}$$

Calculation of the cross products in the 2D configuration leads to the simple relation

$$\vec{E} = i\omega A_y \hat{y}. \tag{3.39}$$

Thus, the radiated electric field at a certain position can be directly determined from the expression for the vector potential $\vec{A}$ according to equation 3.39. After a standard transformation from spherical coordinates to cartesian coordinates the radiated electric field can be determined along the grating coupler axis z, at a certain distance above the grating coupler x . This extension option is included in the final BA-GCE model.

3.3 BA-GCE model

3.3.1 Model description

Finally, all the adaptations and expansions discussed in section 3.2 are combined to convert Flory's model into the novel analytic BA-GCE model. The core calculation of the BA-GCE model is provided in the Mathematica [43] script of appendix A. The scripts for analyzing the results of the model are not presented in the appendix, because of two reasons: firstly, it depends on the properties of interest and secondly, these are just conventional function analysis procedures.

The first step in the conversion of Flory's model to the novel BA-GCE model is to change the electric field calculation to the case of the asymmetric planar slab waveguide. As mentioned in section 3.2.3,

the impact of this adaptation is that the calculation for the β and κ values will be changed, as well as the expression for the $\mathcal{D}$ factor. Furthermore, the asymmetric structure induces the separation of the calculation into a superstrate part and a substrate part. The next step is to implement the decay of light intensity in the waveguide as a result of light outcoupling. The calculation of section 3.2.1 results in a loss factor of the light intensity per grating element F_{loss}. Besides several grating parameters and the $\mathcal{D}$ factor, this F_{loss} factor depends on the element factor $\mathcal{E}$. However, as the $\mathcal{E}$ factor depends on the F_{loss} factor in the grating element, the calculation ends up in a vicious circle. In order to break this vicious circle an iteration process is applied. The iteration process starts by calculating F_{loss} based on the $\mathcal{E}$ factor for a grating element without loss of light intensity, meaning a constant electric field amplitude E_0, which is essentially the expression for $\mathcal{E}$ of Flory's model. Subsequently, an iteration loop is entered in which the adjusted $\mathcal{E}$ factor is calculated based on the previous F_{loss} factor and with this new $\mathcal{E}$ factor, the new value for F_{loss} is determined. This iteration loop continues until the new value of F_{loss} has changed by less than a factor of 10^{-10} compared to its value at the previous iteration step. The final F_{loss} value from this iteration process is then used to determine the final $\mathcal{E}$ factor. Due to this iteration process, the BA-GCE model does not only include the decay of light intensity per grating element, it also takes into account the decay of the light intensity inside each grating element. Thereafter, the array factors can be determined with the general equation for grating couplers with period apodization (equation 3.32). Section 3.2.2 also showed that for a linearly varying grating period, the array factor expression can be simplified into equation 3.33. Due to this simplification the product factor is worked out of the general equation, thereby significantly reducing the computational complexity of the $\mathcal{A}$ function. For uniform grating couplers, even the sum term can be worked out to result in equation 3.21. Hence, these three different cases all have a different level of computational complexity in its expression for $\mathcal{A}$. For this reason the array factor is calculated separately for each case. In the final model calculations, only the functions for the correct period apodization case should be run. The last step in the calculations of the BA-GCE model prior to the analysis is to calculate the radiated Poynting vector and the radiated electric field at a certain position (section 3.2.4). The expression for the radiated Poynting vector is slightly different from the expression in the Flory model (equation 3.25) as a result of the difference in the electric field expressions for an asymmetric and a symmetric slab waveguide structure. Thereafter the analysis of the radiated fields can be carried out. In appendix A only the script for computing the figure of the radiated Poynting vector at a radius of 1 meter is provided, because of the reasons mentioned at the start of this section. Nonetheless, it is important to mention that conventional function analysis procedures are used to compute the results presented in the next chapter, such as peak position, peak value and the full width at half maximum (FWHM).

The main advantage of this model is that it clearly illustrates the underlying physics as explained in section 3.1. The model is transparent in revealing the mechanisms leading to the radiated light. The effects of the two dimensions are separated into the height factor $\mathcal{D}$ and the width factor consisting of the element factor $\mathcal{E}$ and the array factor $\mathcal{A}$. Since these three factors all depend on different grating parameters, intuition can be gained about the effect of one of these parameters. Furthermore, another advantage of this model is the low level of computational complexity of this model. Therefore, the analytic BA-GCE model is capable of calculating the radiated fields of grating couplers of any size in a matter of seconds, contrary to the conventional rigorous simulation methods. For these rigorous simulation methods, simulation of large grating couplers would be too computationally expensive. Thus, the BA-GCE model can be of use in the design optimization process of the large grating couplers used in the PIC alignment sensor. The novelty of the BA-GCE model compared to the Flory model, which also has the aforementioned advantages, is in the adaptations and extensions discussed in the previous section. By combining these adaptations and extensions into the final model, the model is improved and the applicability is extended. Yet, there are still some limitations to the model, which will be discussed in the coming subsection. Obviously, there is still room for improvement of the BA-GCE model, therefore suggestions for improvements and extensions to the current model will be made in chapter 7.

3.3.2 Approximations and limitations

As previously explained in this chapter, there are two important approximations made in the derivation of the analytic BA-GCE model: the Born approximation and the far field approximation. These approximations lead to limitations to the validity and applicability of this model. Before the implications of these two approximations will be discussed, it is important to discuss the other limitations and approximations of the BA-GCE model. One assumption that is made in the calculation of section 3.1 is

that the expression for the Green's function in free space is used. Therefore, this assumes that all the scattered energy will reach the far field. In reality, this is obviously not the case, since a fraction of the light will reflect back and remain in the waveguide. Furthermore, the BA-GCE model is developed for grating couplers with a constant groove width w_1 and only for grating couplers that are etched into the waveguide layer. It is possible to extend the model beyond these two applicability limitations. However, as that requires a completely new and more complex recalculation, it is not yet included in this variant of the model.

Born approximation

The first order Born approximation is applied in the derivation to replace the complicated electric field expression in the waveguide grating region with the electric field expression of the unperturbed waveguide. Obviously, this approximation significantly simplifies the calculations of the BA-GCE model. In order for the Born approximation to be applicable, the electric field in the waveguide grating region must closely resemble the field of the unperturbed waveguide. Therefore, the grating must be a weak perturbation, meaning that it is only applicable to weak grating couplers. In the BA-GCE model, the strength of the grating coupler is quantified by the loss factor of the light intensity per grating element F_{loss}. In order to also incorporate the effect of the grating period Λ, the loss factor can be converted into a fractional energy loss factor per period of the propagating mode, as introduced by Flory [1]. When this fractional energy loss is low enough, the Born approximation can be applied. Hence, the limitation arising from this approximation is that the BA-GCE model cannot be applied to strong grating couplers. In the next chapter, more details will be provided on the fractional energy loss factor and the region of validity arising from the Born approximation will be discussed.

Far field approximation

The far field approximation is applied in order to significantly simplify the expression for the Green's function, since the derivation of a transparent and intuitive analytic model is not possible if the exact Green's function (equation 3.11) would be used. Besides the simplification of the Green's function, the far field approximation also has an effect on the calculation of the relations between the radiated electric field and Poynting vector, and the vector potential. The limitation that arises from this approximation is evident, namely that the BA-GCE model is only valid in the far field regime. A procedure to quantify the far field regime is provided in the next chapter, where the BA-GCE model is extensively benchmarked.

Chapter 4

Simulation results and analysis

In order to assess the performance of the BA-GCE model that is developed in the previous chapter, it is important to carefully benchmark this model. The first step in benchmarking the model is to determine its region of validity. As explained in section 3.3, the applied Born approximation and far field approximation lead to limitations to the validity and applicability of the model. Therefore, the first subsection will elaborate on this region of validity. After that, the adaptations and extensions of the novel BA-GCE model will be benchmarked by comparing it with the results from the Flory model and from the rigorous simulation method Lumerical FDTD [9]. The results from this benchmark process will be discussed in the remainder of section 4.1. Yet, the main advantage of the BA-GCE model is that it is able to simulate radiated fields for large grating couplers, for which rigorous simulation methods would be too computationally expensive. Therefore, an experimental verification of the model will be performed by comparing its results with the experimental measurement results on large grating couplers. As mentioned before, due to serious fabrication problems, the measurements are conducted on a test PIC from the TU/e instead of the actual PIC alignment sensor. Nevertheless, the measured far field profiles of these large grating couplers, which are presented in chapter 6, can be compared with the results of the BA-GCE model, which will be presented in section 4.2. In addition to the benchmarking process, this chapter will present the results obtained with Lumerical FDTD for the standard IMOS grating couplers in section 4.3. These results are used to determine the ideal incouple (and outcouple) angle for the standard IMOS grating couplers. This will be useful in the experimental measurements to maximize the coupling efficiency, as will be explained in more detail in the next chapter. An important remark is that all the results in this chapter are computed for an electric field amplitude (E_0) of 1.

4.1 Benchmarking the BA-GCE model

4.1.1 Region of validity

As discussed before, the two approximations that are made in the derivation of the BA-GCE model limit the region of validity of the model. In the coming two subsections the region of validity resulting from both approximations will be discussed individually.

Born approximation

In section 3.3 it was elaborated that the first order Born approximation is only valid for weak grating couplers and that the strength of the grating couplers can be quantified by the fractional energy loss factor. In the BA-GCE model, the exact value of the F_{loss} factor is calculated, which is defined as the fractional loss of light intensity per grating element. Hence, the fractional loss of light intensity per unit length is defined as $\frac{F_{loss}}{\Lambda}$. Since Flory defines the fractional energy loss per period of the propagating mode, it is more convenient to convert the F_{loss} factor into this $F_{loss,prop.mode}$ factor. Therefore, the fractional loss per unit length needs to be multiplied with the period of the propagating mode ($\frac{2\pi}{\beta}$), leading to equation 4.1, where β refers to the propagation constant of the waveguide mode.

$$F_{loss,prop.mode} = F_{loss} \cdot \frac{2\pi}{\Lambda\beta} \tag{4.1}$$

In order for the Born approximation to be valid, this fractional energy loss per propagating mode should be smaller than some limit value ζ:

$$F_{loss,prop.mode} < \zeta. \tag{4.2}$$

After an extensive analysis, it turned out that this value for ζ for which the Born approximation is valid is very application-specific. This is also illustrated in the paper of Flory [1] as it provides a formula for the upper limit of the $F_{loss,prop.mode}$ factor, given by equation 4.3 in which the symbols refer to the same properties as before.

$$F_{loss,prop.mode} < \left(\frac{2\pi^2 \left(\epsilon_1 - \epsilon_{back}\right)^2}{\epsilon_1} \right) \left(\frac{d_1^2 w_1^2}{\Lambda h \lambda_0^2} \right) \tag{4.3}$$

It was found that the exact value for the $F_{loss,prop.mode}$ factor, calculated in the BA-GCE model, indeed remained below this upper limit and showed similar dependencies. As an illustrative example for the other grating parameters, figure 4.1 shows the dependency of $F_{loss,prop.mode}$ on the grating period Λ for the grating coupler parameters from example in the paper of Flory, which is shown in the top right. It shows that the dependency of $F_{loss,prop.mode}$ on Λ is indeed as suggested by equation 4.3, and that the exact value of $F_{loss,prop.mode}$ remains below the upper limit. All the other grating parameters resulted in the same two conclusions, that $F_{loss,prop.mode}$ remains below Flory's upper limit and that the dependencies are indeed as suggested by equation 4.3, except for the vacuum wavelength λ_0. The BA-GCE model has no clear dependency of $F_{loss,prop.mode}$ on λ_0, contrary to what equation 4.3 suggests. Nonetheless, it can be concluded that equation 4.3 can be used as upper limit for $F_{loss,prop.mode}$, except for extreme values of λ_0. Again the values of λ_0 at which the upper limit cannot be used, depends on the application. Furthermore, it can be concluded that $F_{loss,prop.mode}$ indeed depends on many grating parameters. This means that the region of validity for one grating parameter strongly depends on the values of all the other grating parameters. Therefore, a value for ζ is application-specific and should be found after careful investigation of the specific grating coupler that is to be designed. Moreover, the value of ζ also depends on the required level of accuracy that is demanded for the application.

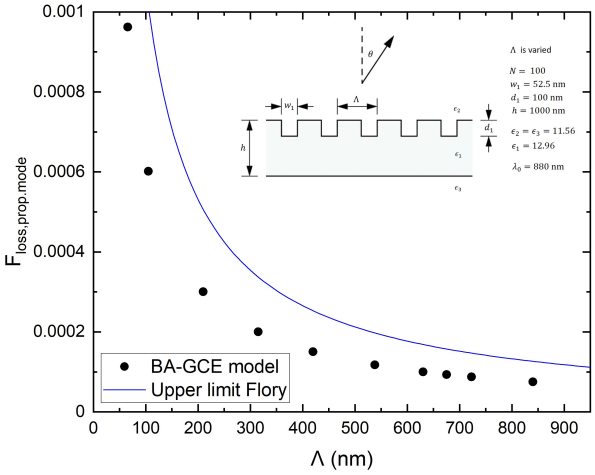

Figure 4.1: Fractional energy loss per period of the propagating mode ($F_{loss,prop.mode}$) from the BA-GCE model (black points) and the upper limit of equation 4.3 (blue line), versus the grating period Λ for the parameter values provided in the top right of this figure.

Overall, the conclusion is that the region of validity of the Born approximation can be quantified by equation 4.2, although an exact value of ζ should be determined per application. It can be determined by comparing the BA-GCE model results with Lumerical FDTD results and finding the value of $F_{loss,prop.mode}$ for which the model results deviate by more than the required accuracy from the Lumerical results. However, since it is very application-specific this is not quantified in more detail in this project.

Far field approximation

Since the far field approximation is applied in the derivation of the BA-GCE model, it is only valid in the far field regime. In order to quantify the far field regime, it will be investigated at which distance from the grating coupler the field profiles of the BA-GGE model will be similar to the field profiles from Lumerical FDTD. The extension of the BA-GCE model to calculate the electric field at a certain position

from the grating coupler is used in this investigation for the comparison with Lumerical. In addition also the phase fronts of the electric fields were compared with Lumerical. Although the phase fronts from both methods also showed similar results, it is less suitable for comparison due to fast oscillations of the phase front over distance that were found in both the BA-GCE model and Lumerical. The electric field intensities were found to be more suitable for profile comparison.

Consider again the grating coupler example of the paper of Flory, shown in figure 4.2a. Note that the number of grating lines is reduced to 25 instead of 100 in order to reduce the size of the simulation, thereby allowing for field monitors at larger distances in Lumerical FDTD. A first investigation proved that for this example the electric field profiles of the monitors are equal to the electric field profiles obtained with the far field extension tool in Lumerical FDTD at a distance from the grating coupler of 10 µm or higher. Hence, for larger distances the far field extension tool is used to determine the electric field profile at the specific distance. Figure 4.2a provides an example for the actual electric field profile determined from Lumerical FDTD (orange curve) and the field profile determined by the BA-GCE model (blue curve) at a distance of 20 µm. This figure clearly illustrates that the far field regime has not been reached at 20 µm. Figure 4.2b shows this comparison at a distance of 200 µm. In this figure the profile of the BA-GCE model resembles the shape of the Lumerical profile more, although the position of the peak is still off. Furthermore, there is a certain scaling factor present between both curves. The cause of this scaling factor will be discussed in more detail in the next section. Therefore, for this investigation the peak position and width, of the electric field profiles are the comparison material and the peak value is not considered for now, since the same scaling factor will always be present. The comparison made in figure 4.2 was extended to other distance values. From this investigation it could be concluded that starting from a distance of 200 µm, the two profiles both have one clear peak in the electric field.

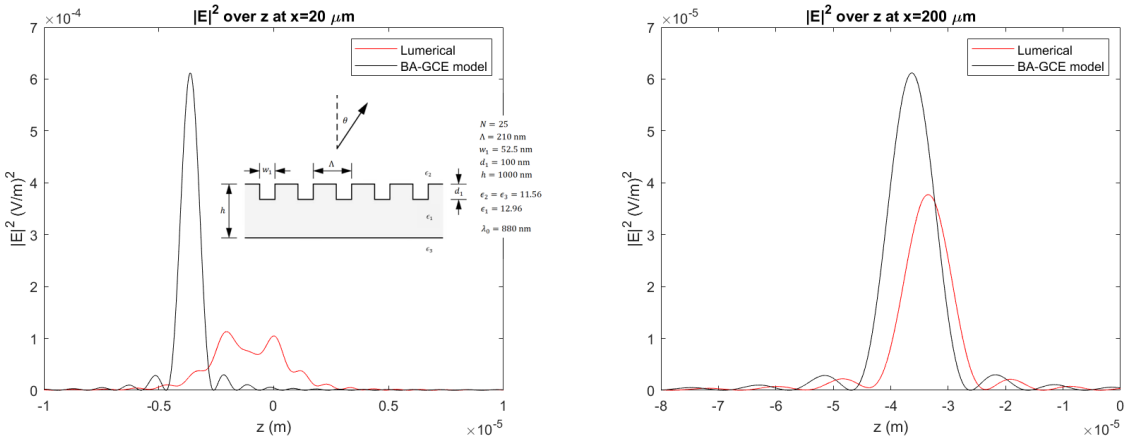

(a) x = 20 µm

(b) x = 200 µm

Figure 4.2: $|E|^2$ profiles as a function of distance along the grating axis (z) at x-distances of 20 µm (left) and 200 µm (right) above the grating coupler, for the grating parameter values shown in figure a. The orange curve represents the Lumerical result and the blue curve represents the BA-GCE model results.

Obviously, due to the divergence of the beam the FWHM increases for larger distances. The difference between the FWHM of the BA-GCE model and Lumerical, normalized by the Lumerical FWHM value, remained constant over distance. Hence, this cannot serve as a measure for the far field regime. An interesting observation that is obtained from this investigation is that the difference in peak positions between the model and Lumerical normalized by the absolute peak position, decreased over distance above the grating. Therefore, this property can serve as a measure for the far field regime. The results are shown in figure 4.3.

Depending on the desired level of accuracy of the peak position, the minimum distance of the far field regime can be determined from figure 4.3. This way, the region of validity of the far field approximation can be determined. For example for this specific case, the relative deviation in peak position of the BA-GCE model compared to Lumerical FDTD is below 1% at distances larger than 5 mm. It is important to perform this validity investigation for each specific application before starting any design optimization process.

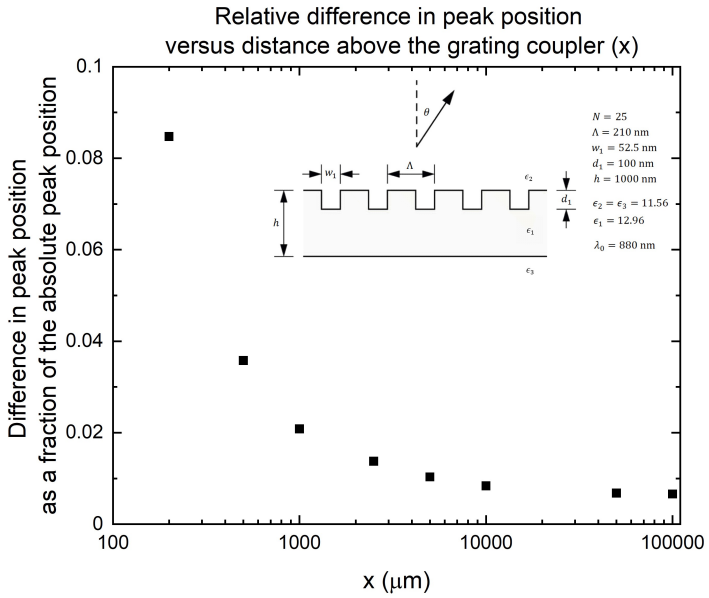

Figure 4.3: Relative difference in peak positions of the $|E|^2$ profiles between the Lumerical results and the BA-GCE results for the grating parameter values in the top right corner, as a function of distance above the grating x.

4.1.2 Benchmarking BA-GCE adaptations

As the region of validity of the BA-GCE model has been discussed in the previous subsection, the next step is to start benchmarking the BA-GCE model. In this subsection the results of the BA-GCE model will be compared to the results of the Flory model, and in addition Lumerical FDTD results will be computed to serve as the benchmark. Since the comparison is made with the Flory model, only the adaptation of including the exponential decrease of light intensity in the waveguide will be benchmarked in this section. In the next subsection, the extension options of the BA-GCE model will be benchmarked with Lumerical, since these extension options are not included in Flory's model. After an extensive analysis, two interesting cases were discovered: the behaviour of the radiation profile under different values for the grating period Λ and under a different number of grating elements N. The main advantage of these two cases is that the expected behaviour is already described in section 2.2. As discussed in this section, it is expected that more diffraction orders will become visible in the radiation spectrum if the grating period is increased. Furthermore, if the grating period is below a certain value, no diffracted orders will be coupled out of the waveguide. Moreover, it is expected that for a larger number of grating lines, more light will be coupled out of the waveguide, while the angle in the far field will remain unaltered. The results for these two cases will now be discussed individually.

Variation of the grating period (Λ)

This investigation starts again with the grating coupler parameter values from Flory's example, which are indicated in the top left corner of figure 4.5. The profiles of the radiated Poynting vector into the superstrate are calculated with the BA-GCE model, the Flory model and computed with Lumerical FDTD, for various values of the grating period Λ. Figure 4.4 shows these results for a grating period value of 420 nm. The black curve represents the BA-GCE model results, the red curve represents the Lumerical FDTD results and the blue curve represents the results from the corrected Flory model. As mentioned in section 3.2.3, the corrected Flory model, in which the scaling difference in E_0 is negated, is used for the comparison.

This figure illustrates that the spectra for all three models are very similar in terms of peak position and peak width, as the difference in peak positions is only 0.07° at maximum. However, as mentioned in the previous subsection, there is a certain scaling factor present between the BA-GCE model results (and Flory model) and the Lumerical results. This will be discussed in more detail in the next investigation, where the number of grating elements is varied. For this purpose, there is a specific interest in the number of diffraction peaks and their positions and widths, since it is expected from theory that the number of diffraction peaks will increase with an increase in the grating period. The final results of this

investigation are shown in figure 4.5, where the position of all the diffraction peaks for various values of the grating period are illustrated. Similarly, the FWHM of all these peaks was compared for the three different models and the resulting values for each peak were within 0.2% of each other.

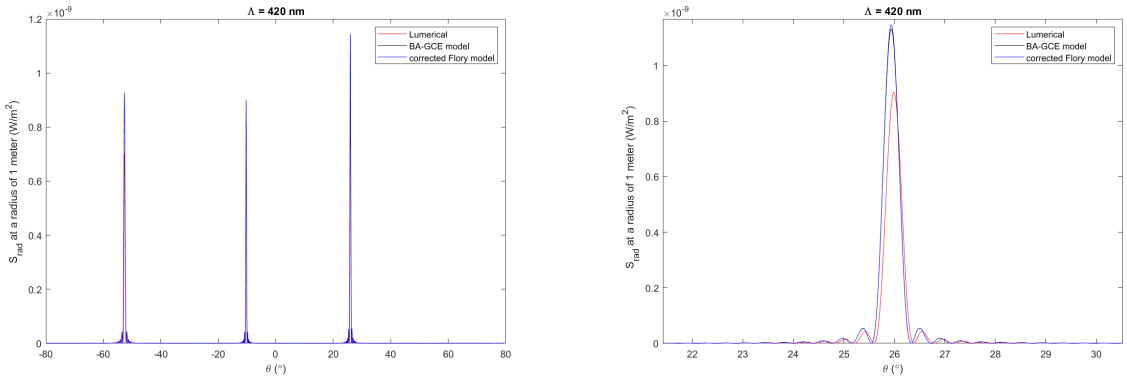

Figure 4.4: Radiated Poynting vector (S_{rad}) for a grating period of 420 nm (a) and zoom of one peak (b), for the BA-GCE model (black curve), Lumerical FDTD (red curve) and the corrected Flory model (blue curve).

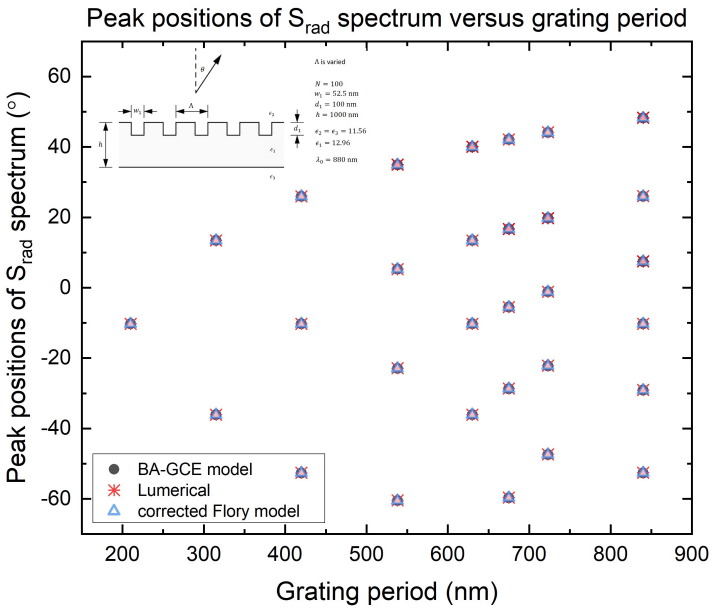

Figure 4.5: Peak positions of the radiated Poynting vector (S_{rad}) spectra for various values of the grating period (Λ). The figure includes results from the BA-GCE model (black dots), Lumerical FDTD (red asteriks) and the corrected Flory model (blue triangles).

First of all, from this investigation it can be concluded that the inclusion of the exponential decay of the light intensity in the waveguide has no effect on the peak position, since the peak position resulting from the BA-GCE model is exactly the same as from the corrected Flory model. Furthermore, except from the peak value, the BA-GCE model are in good agreement with the Lumerical FDTD results. The peak positions are off by 0.07° at maximum and the FWHM of these peaks are within 0.2% of the Lumerical results. The BA-GCE model results are also conform the expectations from theory, since the amount of diffraction orders present in the radiation spectra increases with an increase in the grating period. In addition, the BA-GCE model also correctly simulates the behaviour at small grating periods. As explained in section 2.2, below a certain grating period, no diffraction peaks will be radiated out of the waveguide and that is indeed observed.

Variation of the number of grating elements (N)

This investigation is again performed with the parameter values of the grating coupler example of Flory (figure 4.6), whereas the number of grating elements (N) is now varied. As shown in figure 4.5, there is only one diffraction peak at a grating period of 210 nm. The characteristics of this diffraction peak are compared for various number of grating elements. As concluded from the previous investigation, the inclusion of the exponential decay of light intensity in the waveguide, which is currently the only adaptation to the Flory model, has no effect on the position of the diffraction peak and that was indeed verified in this investigation too. The inclusion of the exponential decay does have an effect on the peak value and the peak shape, and thereby the FWHM. The peak values of the radiated Poynting vector at a radius of 1 meter for various values of N are shown in figure 4.6.

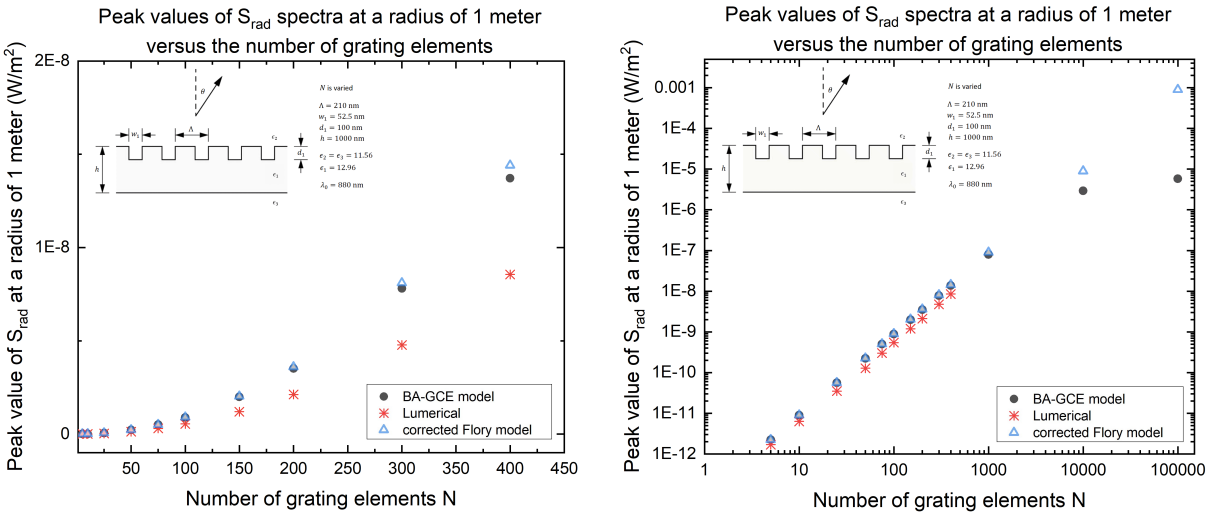

Figure 4.6: Peak value of the radiated Poynting vector (S_{rad}) spectra at a radius of 1 meter for various number of grating elements N. The left figure is on a linear scale, whereas the right figure is on a logarithmic scale with an extended x-axis. Again the results of the BA-GCE model (black dots), Lumerical FDTD (red asterisks) and the corrected Flory model (blue triangles) are included.

The first observation that follows from the left figure of figure 4.6 is that the scaling factor difference between the BA-GCE model results and the Lumerical FDTD results scales with the number of grating elements. This is an interesting observation which gives an indication for the physical explanation behind the existence of this scaling factor. This scaling factor means that according to the BA-GCE model more light is radiated out of the grating coupler than according to Lumerical, which serves as a benchmark for the reality. The most probable explanation is that in the BA-GCE model, all the emitted radiation in each grating groove reaches the far field. In reality (Lumerical), part of the radiation will be reflected at the grating substrate interface. This is an effect which will scale with the number of grating elements and therefore it can be an explanation for this observation. Another optional cause for this scaling factor is an incorrect fractional loss factor, since that would also lead to a scaling factor that scales with the number of grating elements. However, this can never be the sole explanation for the scaling factor, since a correction of the BA-GCE model for the difference in peak value would require a fractional loss factor which is much larger than Flory's upper limit (equation 4.3). Though, it is possible that this difference in the fractional loss factor in combination with the fact that in the BA-GCE model all emitted radiation reaches the far field, provides the physical explanation behind this scaling factor. Although, these two explanations are provided, it cannot be ruled out that there are other effects also contributing to the scaling factor. Nonetheless, the two mentioned explanations are plausible explanations, since these effects would indeed lead to a larger peak value in the BA-GCE model and would indeed scale with the number of grating elements.

The effect of the inclusion of the exponential decay of the light intensity in the waveguide becomes apparent from the right figure of figure 4.6. Whereas the peak value of the Flory model results keep increasing for a higher number of grating elements, the results from the BA-GCE model show asymptotic behaviour towards a maximum. Similar behaviour was found for the shape of the diffraction peak. For smaller values of N this was still very similar for all three results. However, for larger values of N (which could

not be simulated with Lumerical) the FWHM of the peak according to the Flory model kept decreasing, whereas it approached a minimum value in the BA-GCE model. Intuitively, this asymptotic behaviour is indeed expected, since the intensity of the light is decreased throughout the grating coupler as a result of the outcoupling of light. Therefore, less and less light remains in the waveguide, available to be coupled out. Hence, it is indeed expected that the peak value of the radiated Poynting vector asymptotically approaches its maximum, which corresponds to the point when all the light in the waveguide has been coupled out. Moreover, it is expected that the FWHM of the diffraction peak does not keep decreasing, because at a certain point the grating elements do not radiate sufficient light intensity to have a noticeable impact on the diffraction peak. Thus, the improvement resulting from the inclusion of the exponential decay becomes apparent for large grating couplers. Unfortunately, Lumerical FDTD results cannot be computed for such large numbers of grating elements, since that is too computationally expensive. So, although the BA-GCE model indeed simulates the expected behaviour correctly, contrary to the Flory model, the exact asymptotic behaviour cannot be compared with Lumerical. Multiple other examples of grating coupler parameters, especially for stronger grating couplers, have been investigated to try to find certain parameters for which the asymptotic behaviour already occurs at smaller number of grating elements. Indeed it was found that (as expected) for stronger grating couplers, this asymptotic behaviour was observed at smaller number of grating lines. However, since the BA-GCE model is only valid in the Born approximation regime, the grating coupler could not be made too strong. Eventually, it was concluded that the asymptotic behaviour did not start at a smaller number of grating lines than 1000, in the validity regime of the Born approximation (where a ζ value of 10^{-2} suggested by Flory was used as indication). Even for this number of grating lines, the Lumerical simulations were too computationally expensive, which at the same time underlines the desire for an analytic model that is able simulate large grating couplers.

Since the scaling factor between the BA-GCE model results and the Lumerical FDTD results has been extensively discussed, and probable explanations have been proposed, the remainder of this thesis will work with the radiation spectra normalized to 1, to provide a more intuitive comparison.

4.1.3 Benchmarking BA-GCE extensions

The last step in the benchmarking process of the BA-GCE model is to compare the results of this model including the extensions options, to Lumerical FDTD. First, the extension of the asymmetric waveguide structure is benchmarked. Therefore, the asymmetric grating coupler structure, of which the values are displayed in the results of figures 4.7 and 4.8, is simulated with the BA-GCE model (black curves) and Lumerical FDTD (red curves). The normalized radiated Poynting vector spectra are computed for the radiation into the superstrate (figure 4.7) and into the substrate (figure 4.8).

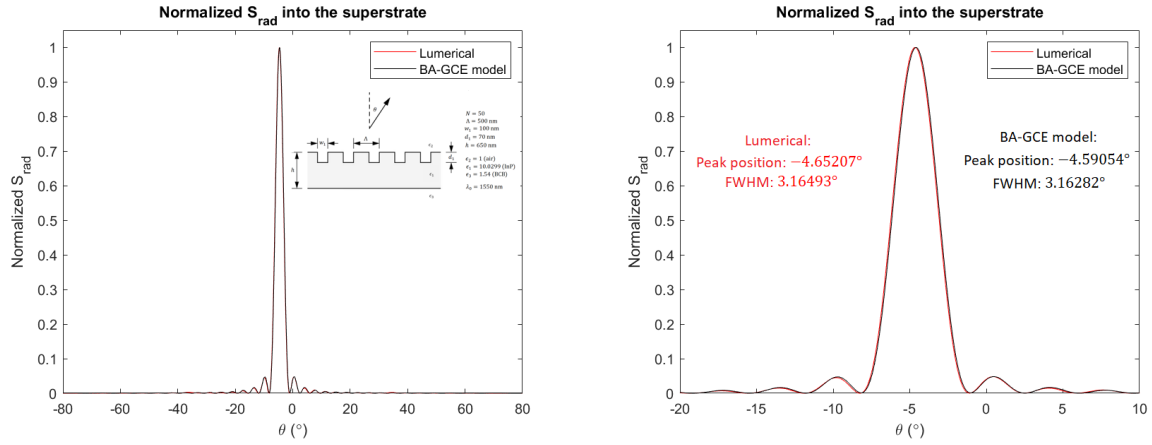

Figure 4.7: Normalized spectra for the radiated Poynting vector (S_{rad}) into the superstrate (left) and a zoom of the peak with relevant characteristic values (right) following from the two models: BA-GCE (black) and Lumerical FDTD (red).

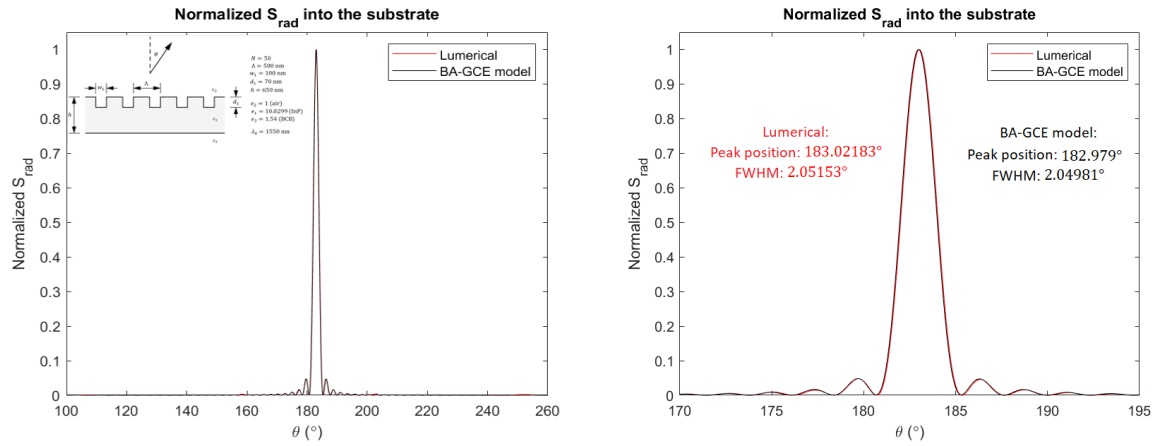

Figure 4.8: Normalized spectra for the radiated Poynting vector (S_{rad}) into the substrate (left) and a zoom of the peak with relevant characteristic values (right) following from the two models: BA-GCE (black) and Lumerical FDTD (red).

From these figures it can be concluded that the BA-GCE model is in good agreement with the Lumerical FDTD results, also for grating couplers with an asymmetric waveguide structure. The values of the peak position and FWHM are also included in these figures and show that the difference in peak position normalized to the FWHM is only around 2% for both the substrate and the superstrate. Therefore, this proves that the asymmetric waveguide extension functions properly.

The second and final step is to assess the performance of the grating period apodization extension, together with the other adaptations and extensions of the BA-GCE model. Therefore, the grating coupler structure of the previous investigation is simulated for 51 grating elements with a linearly increasing grating period from 487.5 nm to 512.5 nm. The results for the normalized radiated Poynting vectors into the substrate (a) and into the superstrate (b) are shown in figure 4.9. These figures are zoomed in on the nonzero parts of the normalized radiation spectra.

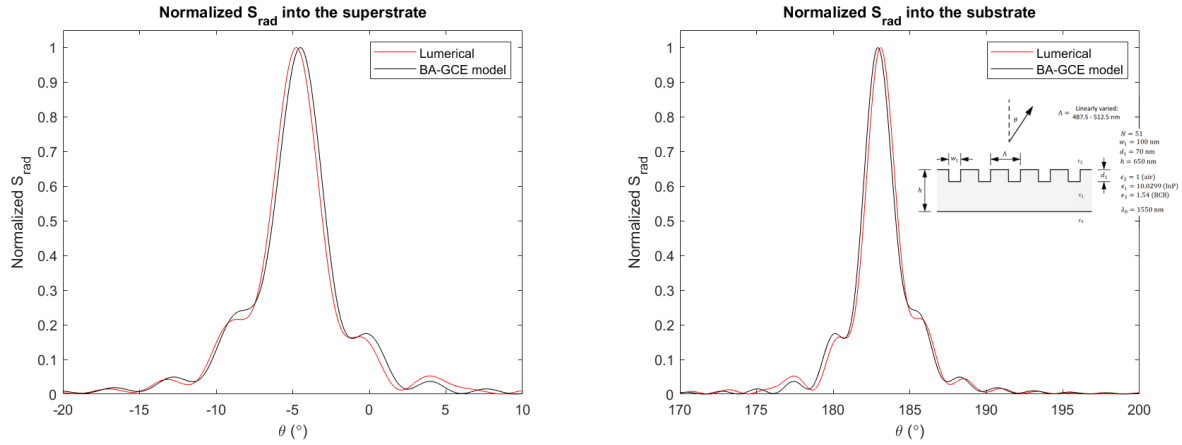

Figure 4.9: Normalized spectra for the radiated Poynting vector (S_{rad}) into the superstrate (left) and into the substrate (right) following from the two models: BA-GCE (black) and Lumerical FDTD (red). The period of the grating coupler is linearly varied from 487.5 nm to 512.5 nm over the 51 elements.

From figure 4.9 it can be concluded that the BA-GCE model is able to correctly simulate radiation profiles of apodized grating couplers, since the radiation profile from the BA-GCE model is similar in shape to the Lumerical results. Furthermore, the difference in peak position between the two results normalized to the FWHM is still below 8%. Hence, the BA-GCE model is within reasonable accuracy for apodized grating couplers. However, an important remark to be made is that the approximations made in the BA-GCE model also result in limited validity ranges for apodized grating couplers. The results of the BA-GCE model deviate more and more from the Lumerical results when the strength of the period apodization (referring to the difference in period between the grating elements) is increased. This effect is exemplified by figure 4.10, which presents the simulated results for the same grating coupler as in figure

4.9 except that the grating period is linearly increased with steps of 1 nm (from 475 nm to 525 nm) instead of steps of 0.5 nm. The figure indeed illustrates that the results of the BA-GCE model for this apodization significantly deviate from the Lumerical results. This behaviour can be explained by first order Born approximation that is applied in the derivation of the BA-GCE model. Since an increase of the grating period difference will increase the effective refractive index variation between each subsequent grating element, the fields from the waveguide mode start to deviate more and more between subsequent elements. Consequently, the error introduced by the first order Born approximation increases, since the approximation replaces the exact fields in the waveguide grating region (for each element) by the constant electric field of the unperturbed waveguide. Thus, it is important to take into account that the BA-GCE model is only valid for limited grating apodization strengths. The quantification of the validity range is again application-specific and depends on the desired accuracy.

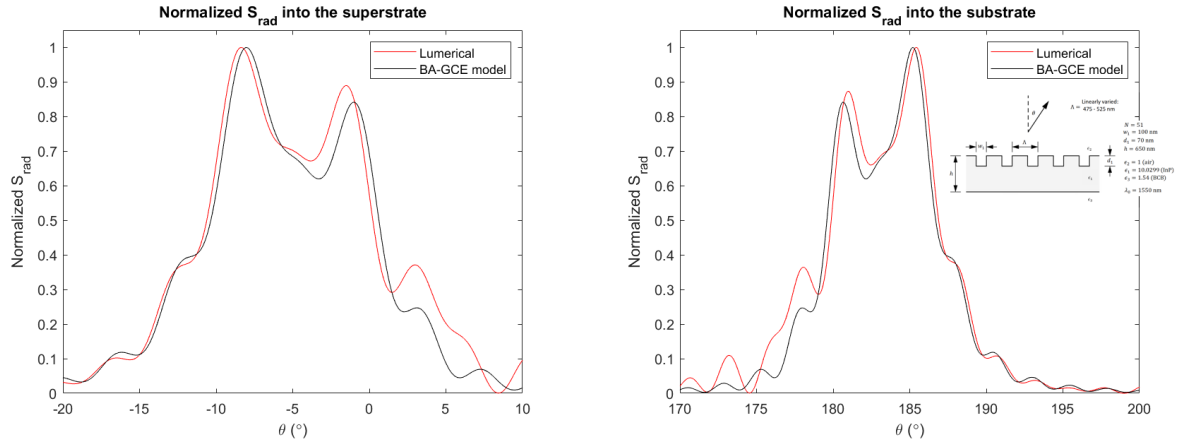

Figure 4.10: Normalized spectra for the radiated Poynting vector (S_{rad}) into the superstrate (left) and into the substrate (right) following from the two models: BA-GCE (black) and Lumerical FDTD (red). The period of the grating coupler is linearly varied from 475 nm to 525 nm over the 51 elements.

As mentioned in section 2.2, period apodization can be used to create focusing grating couplers, as illustrated by equation 2.10. However, a change in the period of the grating coupler also changes the effective refractive index of the waveguide grating structure, which significantly complicates the design process of focusing grating couplers with only period apodization. For this reason the above investigation is not performed on a focusing grating coupler. As also mentioned in section 2.2, the common approach is that the grating groove width is also adapted to counteract the change in effective refractive index resulting from the period apodization. Thus, an important step for further improvement of the BA-GCE model is to allow for varying grating groove widths, such that both period and width apodization can be used to simplify the focusing grating coupler design process. Period apodization is thus already incorporated in the current BA-GCE model.

4.2 BA-GCE model results for experimental grating couplers

Besides the theoretical benchmarking of the BA-GCE model, it is also interesting to perform experimental verification of the model. Therefore, experimental measurements are performed on large grating couplers TU/e test PIC (discussed in section 2.2.4), and the results are presented in chapter 6. For comparison, the BA-GCE model results for these experimentally measured large grating couplers will be presented in this section. However, there is a difficulty in this comparison. The BA-GCE model is developed for grating couplers that are etched into the waveguide layer, whereas the experimentally measured large grating couplers are etched into the superstrate. Conversion of the BA-GCE model to a model in which the grating coupler is etched into the superstrate is theoretically possible, however it would require a completely renewed derivation. Hence, it is left open for the future to redevelop the BA-GCE model into a model in which the grating coupler is etched into the superstrate. In this thesis, this difficulty is circumvented in the best way possible by identifying the equivalent structure where the grating is etched into the waveguide layer, that results in a similar output profile. This investigation is performed with Lumerical and the results are provided in appendix B. Thereafter, the equivalent structure is used to compute the radiated spectra of the experimentally measured large grating couplers with the BA-GCE model.

For the comparison, the normalized radiated electric field intensity is computed with the BA-GCE model for the three equivalent structures. The three measured grating coupler structures differ in their value for the FF. The three variants of the large grating couplers have FFs of 0.5, 0.65 and 0.8. The measurements are performed on the 200 µm long grating couplers, consisting of 333 grating elements (N). In these measurements the output beam is measured at two distances: 17 mm and 20 mm above the PIC. Hence, also the BA-GCE model results for the normalized electric field intensity profiles are computed for these large grating coupler structures at 17 mm and 20 mm. The resulting normalized electric field intensities for the large grating coupler with FF = 0.65 are shown in figure 4.11. This result is illustrative for the results of the other large grating couplers with different FF values. They all have a single peak with a similar shape as in figure 4.11. There are only some minor differences in the positions and FWHM of the electric field intensity peaks. The values for these peak characteristics for the three different variants at the two different heights are provided in table 4.1. They will be compared with the experimental results in section 6.2.

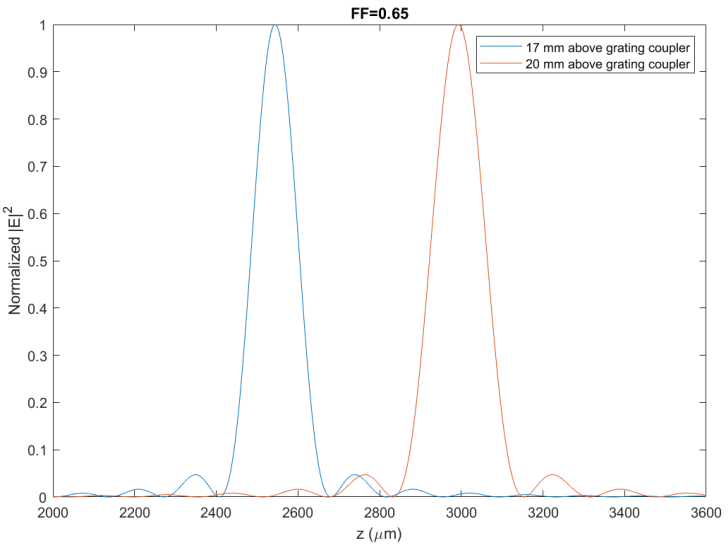

Figure 4.11: Normalized electric field intensities for the equivalent structure of the large grating coupler with FF = 0.65 at 17 mm (blue curve) and 20 mm (orange curve) above the grating coupler, computed with the BA-GCE model.

Equivalent grating coupler structure for FF:	x (mm)	Peak characteristics	
		Position z (µm)	FWHM (µm)
0.5	17	2516.78	120.701
	20	2960.91	142.001
0.65	17	2544.12	120.788
	20	2993.07	142.104
0.8	17	2572.14	120.873
	20	3026.05	142.203

Table 4.1: Position and FWHM values of the electric field intensity peak for the three different large grating coupler variants (different FF values) at 17 and 20 mm above the grating coupler (x). The results are computed with the BA-GCE model applied to the equivalent structures discussed in appendix B.

4.3 Standard IMOS grating couplers

The standard IMOS grating couplers are used to couple light into and out of the PIC by using angle polished fibers, as will be explained in more detail in the next chapter. In order to achieve maximum incoupling and outcoupling efficiencies, the ideal coupling angle of these grating couplers needs to be determined. Hence, in this section the ideal coupling angles of the standard IMOS grating coupler structures will be determined through accurate Lumerical FDTD simulations. Contrary to the large area grating

couplers, the standard IMOS grating couplers can be simulated in full scale with Lumerical FDTD simulations due to their relatively small footprint of 16.5 µm by 15 µm.

The standard IMOS grating couplers are general building blocks of the IMOS platform of the TU/e. Extensive research has been conducted to find the layer stack for maximum coupling efficiency. This resulted in the optimum layer stack that is shown in figure 4.12. The layer stack consists of a 300 nm thick InP waveguide layer on top of the silicon wafer, with a buffer layer in between. This buffer layer consists of a 1850 nm thick BCB layer ($n = 1.54$ [13]) in between two 50 nm thick SiO_2 layers. Due to some additional required processing steps for the PIC alignment sensor prototype, the final layer stack will have a 100 nm thick layer of SiO_2 on top of the InP membrane (J.P. van Engelen, private communication, April 2022). Near the grating groove edges this will result in 70 nm thick SiO_2 sidewalls, as shown in figure 4.12 (J.P. van Engelen, private communication, April 2022). The standard IMOS grating coupler system consists of a grating coupler and a linear taper. The grating coupler has a uniform period of 660 nm, and 330 nm wide and 120 nm deep grooves. There are 25 grating elements leading to a total length of 16.5 µm. The width of the grating coupler structure in the third dimension is 15 µm. In order to convert the standard 400 nm wide waveguide mode into the 15 µm wide mode that enters the grating coupler, a 250 µm long linear taper is used.

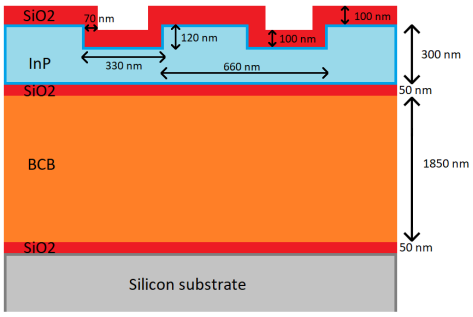

Figure 4.12: Layer stack of the standard IMOS grating coupler on the PIC alignment sensor prototype. There is a buffer layer of 1850 nm thick BCB, sandwiched between two 50 nm thick SiO_2 layers, between the silicon substrate and the 300 nm thick InP layer. On top of the InP layer is an additional 100 nm thick $SiO2_2$ layer which leads to 70 nm wide sidewalls in the grating grooves.

In order to determine the ideal coupling angle for the standard IMOS grating coupler system, the far field radiation pattern is computed through Lumerical FDTD simulations. The angle at which the radiation pattern has maximum intensity then provides the best prediction for the ideal coupling angle. Moreover, since the grating coupler is a reciprocal system, as mentioned in section 2.2, the ideal coupling angle will be the same for both incoupling and outcoupling.

The standard IMOS grating coupler system can be divided into two parts: the linear taper and the grating coupler itself. The linear taper is used to convert the 400 nm wide waveguide mode into a 15 µm wide mode going into the grating coupler structure. Therefore, the linear taper is simulated separately in a Lumerical MODE simulation [44]. The eigenmode expansion solver tool is used to propagate the initial waveguide mode, through the linear taper, to the start of the grating coupler. As expected for the linear taper, the simulations show that most of the light is simply converted into the fundamental mode for a 15 µm wide waveguide. Therefore, for the purpose of finding the ideal coupling angle of the system, the assumption can be made that the grating coupler has a perfect fundamental waveguide mode as input. With this fundamental waveguide mode as input, Lumerical FDTD simulations [9] are performed to compute the far field radiation pattern of the grating coupler structure. The normalized far field electric field intensity profile of the three-dimensional (3D) Lumerical FDTD simulation is shown as a polar plot in figure 4.13. The red arrow indicates the propagation direction of the light through the waveguide-grating structure and the values refer to the angles of the polar plot in degrees.

The far field intensity profile of figure 4.13 clearly shows an intensity peak at one specific location, corresponding to the ideal coupling angle. As expected for the symmetric grating coupler structure, the far field radiation pattern is perfectly symmetric in the $y = 0$ plane. Moreover, the maximum field intensity point is also at $y = 0$, corresponding to an angle of $0°$ with respect to the y-axis, again due to its symmetry. Consequently, the 3D simulation can be changed into a 2D simulation without losing any

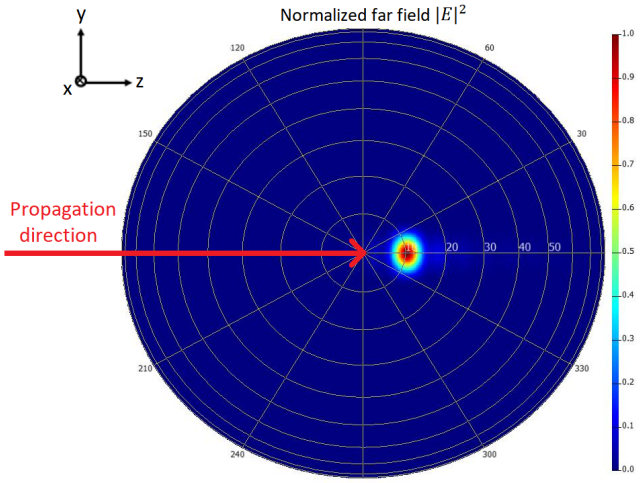

Figure 4.13: Polar plot of the normalized far field $|E|^2$ profile of the standard IMOS grating coupler, obtained through 3D Lumerical FDTD simulations [9]. The propagation direction of the waveguide mode is indicated by the red arrow. The numerical values in the polar plot refer to the angles in degrees.

relevant information on the angle of maximum output intensity, since that is at 0° for the y-axis. This dimensionality reduction will significantly decrease the computational burden of the simulation, thereby allowing for finer mesh grids, leading to more accurate simulation results. For this reason, the exact value of the angle with maximum field intensity is determined through 2D Lumerical FDTD simulations of the standard IMOS grating coupler. Besides the other standard convergence tests, it is important to compute the angle corresponding to the maximum field intensity for various levels of mesh accuracy, in order to check if the simulation has converged and to find the final angle value. Figure 4.14 shows the resulting angle at which the far field has maximum intensity for various levels of mesh accuracy. These levels of mesh accuracy are defined on the x-axis by the number of mesh cells per wavelength.

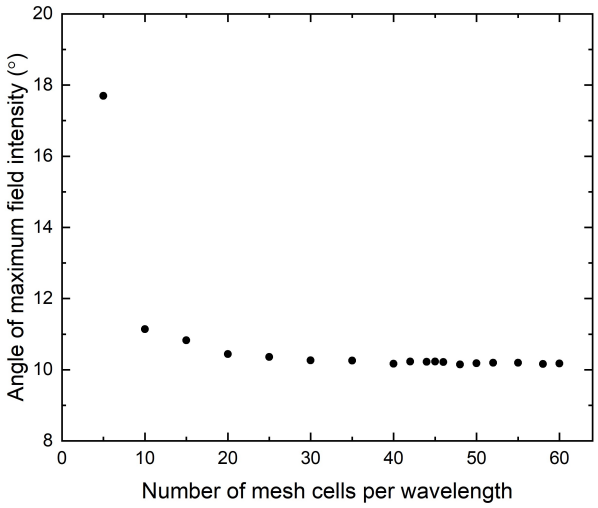

Figure 4.14: The angle (in degrees) corresponding to the point of maximum far field intensity, obtained from 2D Lumerical FDTD simulations [9], versus the number of mesh cells per wavelength.

From figure 4.14 it can be concluded that the simulations have certainly converged for 40 mesh cells per wavelength and higher. By calculating the mean and standard deviation of the resulting output angles for this minimum required mesh accuracy, the angle corresponding to the maximum field intensity of the standard IMOS grating coupler can be determined. This results in:

$$\theta_{max} = (10.19 \pm 0.03)^\circ. \tag{4.4}$$

Thus, the ideal coupling angle for the simulated standard IMOS grating coupler structure will be equal to $(10.19 \pm 0.03)^\circ$ in the plane perpendicular to the grating lines, and 0° in the plane parallel to the grating lines, due to the symmetry of the structure.

Chapter 5

Experimental setup

5.1 Experimental setup description

Another important part of this research project is to completely prepare the experimental setup for the upcoming measurements on the PIC alignment sensor prototype. In addition, its the beam profile measurement capabilities are demonstrated by the calibration measurements on the angle polished fibers and by the measurements on the large grating couplers, which will be presented in chapter 6. First, the experimental setup will be discussed in more detail in this chapter. The experimental setup was designed, initially built and calibrated by M.R. Otto. Due to a scheduled movement to a new location, it was disassembled and built up again in this research project. Furthermore, some small adjustments (fiber rotator and motorized goniometer under wafer sample stage) are made to the setup, which clarifies the small differences between this experimental setup description and the thesis of M.R. Otto [7]. Due to the reconstruction of the experimental setup, some additional calibrations are performed, which will be discussed in this section. In addition, an extensive procedure to receive the so-called "green label" for the experimental setup has been followed. This green label indicates that the experimental setup fulfills all the requirements for safe operation, according to the general European and ASML safety standards. The green label approval process starts with a risk assessment of the setup. Afterwards, a detailed operation manual and electric scheme have to be made. Lastly, the experimental setup needs to pass the electrical inspection, after which the safety of the experimental setup can be approved and the green label is received.

The experimental setup that is used in this research project is shown in figures 5.1 and 5.2. The procedures of the measurements that can be performed with this setup will be explained in the next section, first the setup will be described. The experimental setup is build on top of an optical table and inside a cleanroom area to operate in a vibration free and clean environment. Figure 5.1 shows the front view of the experimental setup. The tunable laser source is a Santec TSL-550 with tunable wavelengths in the infrared (IR) range (1480-1630 nm), and it is indicated with number 1. Number 2 refers the photodetector, also in the IR wavelength range, and the photodiode amplifier. The photodetector is a Thorlabs DET10C2 and the amplifier is a Thorlabs PDA200C. Close up pictures of the breadboard setup, which is in the middle of figure 5.1, are shown in figure 5.2. In this figure, number 1 again indicates the tunable laser source. The visible light camera system is indicated with number 3 and consists of the Basler acA4112-8gm camera connected to a 12x zoom lens on top of mutually orthogonal manually adjustable stages. Number 4 indicates the IR camera system, consisting of the IR camera (Raptor Photonics NX1.7-VS-CL-640) with a microscope unit and a near IR objective. This objective has a 50x magnification, a focal length of 200 mm and a depth of field of 0.65 µm. The field of view (FoV) of this camera system is 192 µm by 154 µm. The IR camera system is attached to a vertical motorized stage (Newport TRB25CC), to accurately control the height of the camera. This assembly is screwed on top of a manual dual axis stage, which is then attached to a vertical breadboard. The fiber rotator stage is indicated by number 5 and consists of a Newport optical fiber rotator (466A-717), which clamps the fiber, on top of a manual goniometer (Thorlabs GN05/M), both providing one rotational degree of freedom. This assembly is put on top of a triple axis manual stage to control the three translation degrees of freedom. There is a fiber rotator stage on either side of the setup, one to couple light into the PIC and the other one to couple light out of the PIC. For the incoupling of light, the fiber is connected to the tunable laser source (1). The light that is coupled out of the PIC can be connected to the photodetector and amplifier (2) to measure the output signal. Number 6 indicates the wafer sample stage consisting of a motorized

vertical lift stage (Zaber X-VSR20A), with a motorized double goniometer (Thorlbas GNL20/M-Z8) and a SmarAct piezo element assembly on top. The piezo element assembly consists of two translational piezo elements, with an absolute accuracy of 30 nm and a resolution of 1 nm, and one rotational piezo element with a resolution of 1 µrad [7]. This way, all six degrees of freedom (translational and rotational) of the wafer sample stage are motorized. The wafer sample is eventually glued onto a glass scale plate (Thorlabs R1L3S1P), which is clamped between the two cylinders of the piezo element assembly, as shown in figure 5.2. Furthermore, an additional white light source, indicated by number 7, is integrated in the setup to aid in the alignment procedure. Lastly, the small blue star in figure 5.2 indicates the custom-made chuck for holding the PIC. It is connected to a vacuum source to suck the PIC to the bottom of the chuck. The PIC chuck is placed on top of a manual dual axis translation stage to extend the range over which the PIC can be measured. For more details on all the individual components a reference is made to the thesis of M. R. Otto [7], since this thesis is completely devoted to the design, construction and calibration of the experimental setup.

After construction of the experimental setup, it is crucial that the elements of the setup are accurately aligned with respect to each other. As described in his thesis [7], multiple setup calibrations are already executed by M.R. Otto. Still, some additional calibrations are performed in this research project. For the purpose of this project, it is crucial to accurately align the plane of the IR camera system to the plane of the PIC chuck and to align the translational travelling directions of the IR camera to the plane of the PIC chuck. Firstly, the translational travelling directions are accurately aligned by using a spirit level and inserting thin slices of aluminium shim stock at specific positions underneath the two manual stages of the IR camera system, to make it level in both directions. Since the PIC chuck was already level, its position and orientation remains unaltered. Secondly, the planes of the IR camera and the PIC chuck are aligned by bringing the complete FoV of the IR camera into focus. This is achieved by inserting shim stock underneath the three bolt locations where the 90 degrees bracket of the IR camera system is attached to the two manual translation stages. After completion of this time consuming alignment process, it is ready to be used in measurements. Yet, before the actual measurements are performed, it is important to perform the fiber calibration measurements. The results of these fiber calibration measurements are presented and discussed in section 6.1. They are used to determine the desired orientation of the fiber rotator stages for maximum light coupling, as will be explained in the next section. Furthermore, in the fiber calibration measurement the absolute rotation angle is calibrated to the scale of the fiber rotator. This is simply achieved by determining the value of the fiber rotator scale corresponding a 0° or 180° rotation angle of the fiber, with the use of the visible light camera system. Additionally, the experimental setup has been completely prepared for the measurements on the PIC alignment sensor that were part of the initial plan for this research project. Therefore, all the individual components of the setup are connected to their power supplies and control equipment. The associated software programs are downloaded and a correct operation of the individual components, through the software, has been achieved and verified. Detailed instructions on how to operate the experimental setup, including the software programs, have been written and shared with the future users of the setup. This will allow for immediate performance of the characterization measurements on the PIC alignment sensor prototype, once it is delivered. After these additional calibrations and preparations of the experimental setup, the actual measurements can be performed. The next section will elaborate on these measurement procedures and how the setup is used to perform them.

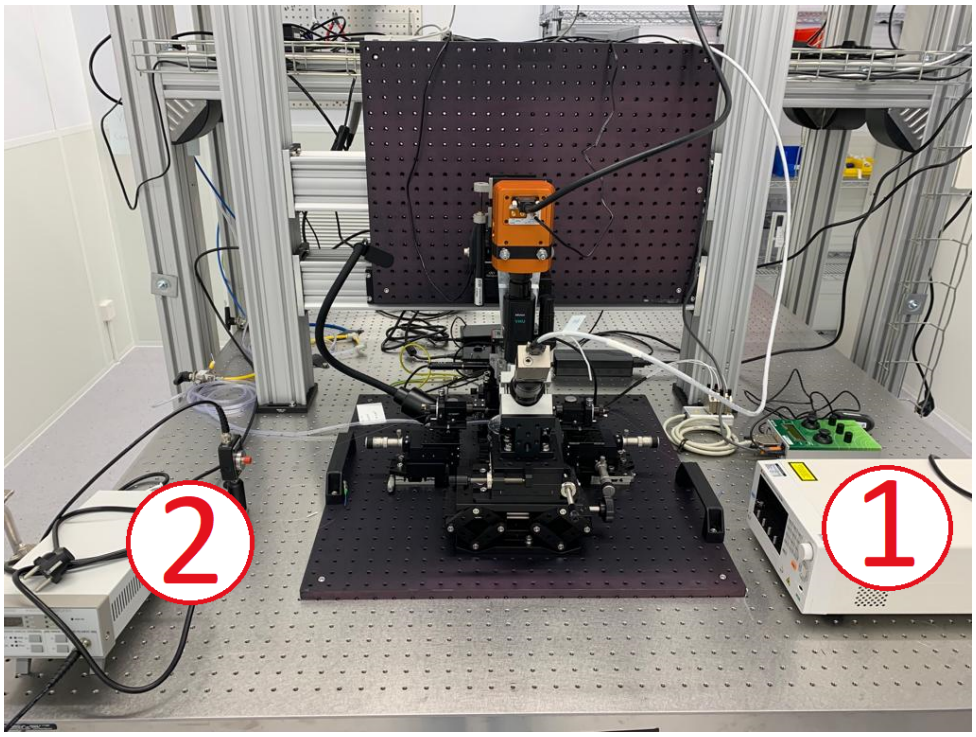

Figure 5.1: Front view of the experimental setup. In the middle of the figure the breadboard setup, for which close up images are shown in figure 5.2. On the sides of the breadboard setup are the tunable laser source (1) and the photodetector and amplifier (2).

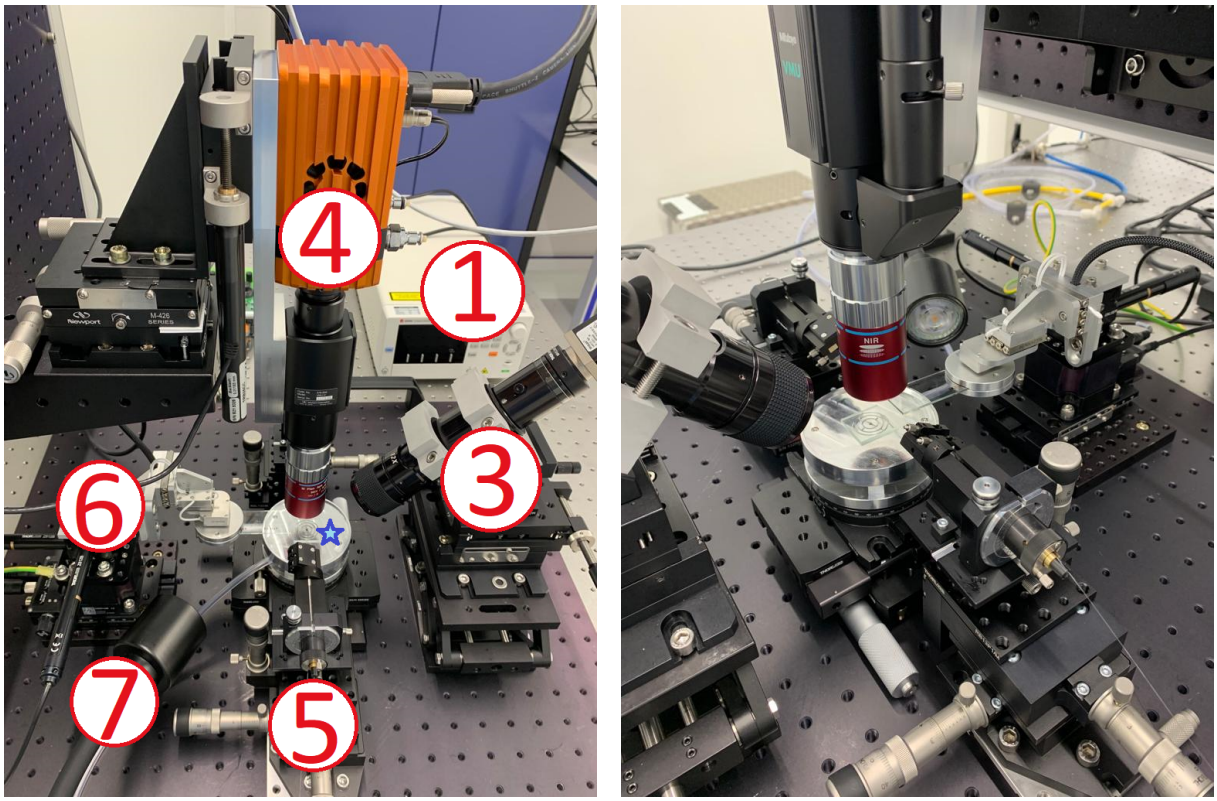

Figure 5.2: Side views of the experimental setup, where the numbers refer to the following components: tunable laser source (1), visible light camera system (3), IR camera system (4), fiber rotator stage (5), wafer sample stage (6) and white light source (7). The blue star marks the vacuum sucked PIC chuck.

5.2 Experimental measurement procedure

The experimental setup is designed to perform two main types of measurements: beam profile measurements and alignment scans. As mentioned before, the initial plan was to perform measurements on the PIC alignment sensor prototype, which would also include alignment scans. However, since measurements could only be conducted on the large grating couplers of the TU/e test PIC, only the beam profile measurements are actually performed in this research project. Hence, the beam profile measurement procedure will be extensively described in this section, whereas the alignment scan procedure is only briefly mentioned to illustrate the capabilities of the setup. Before these two measurement procedures are discussed, some additional information is provided on the fibers used to couple light into and out of the PIC.

5.2.1 Angle polished fibers

Since the IR camera system takes up the space above the PIC chuck, the light from the fibers should be coupled into the PIC horizontally. Therefore, angle polished fibers are used. Due to total internal reflection (TIR) of the light travelling in the core of the fiber at the cleaved facet, an output beam is produced from these angle polished fibers. In order to achieve the required TE polarization, the angle polished fiber should be coupled to the standard IMOS grating coupler according to the configuration in figure 5.3a. In this figure ω is defined as the tilt angle of the fiber rotator stage. Furthermore, the relative rotation angle of the fiber is referred to as the angle of incidence (AoI). The value for AoI is determined by the Lumerical FDTD simulations of section 4.3, corresponding to the ideal coupling angle of the standard IMOS grating coupler. Thus, in order to achieve maximum coupling, the relative rotation angle of the fiber rotator stage is set to this value of AoI. The angle θ_{out} in figure 5.3a refers to the output angle of the fiber, which is determined from the measurements in section 6.1. In summary, the value for AoI is determined from the simulations in section 4.3 and the value for θ_{out} is determined from the measurements in section 6.1, meaning that only the tilt angle ω still needs to be determined. The required value for this angle can be determined from its relation with the other two angles.

Consider figure 5.3b in which the configuration of figure 5.3a has been converted into vector notations. The angle θ_{out} can be determined from the dot product of the two vectors $\vec{a}$ and $\vec{b}$, as illustrated in figure 5.3b. For simplicity, the length of both vectors are set to 1, yielding

$$\vec{a} \cdot \vec{b} = |\vec{a}| \left|\vec{b}\right| \cos(\theta_{out}) = \cos(\theta_{out}). \tag{5.1}$$

The dot product is defined as the sum of the multiplication of the respective components:

$$\vec{a} \cdot \vec{b} = a_x b_x + a_y b_y + a_z b_z. \tag{5.2}$$

The vector components can be determined from the two right figures in figure 5.3b, while using the fact that the length of the vectors is equal to 1. Simple trigonometric calculations then lead to equations 5.3 and 5.4 for the vector components.

$$\vec{a} = \begin{pmatrix} a_x \\ a_y \\ a_z \end{pmatrix} = \begin{pmatrix} \sin(\text{AoI}) \\ 0 \\ -\cos(\text{AoI}) \end{pmatrix} \tag{5.3}$$

$$\vec{b} = \begin{pmatrix} b_x \\ b_y \\ b_z \end{pmatrix} = \begin{pmatrix} 0 \\ -\cos(\omega) \\ \sin(\omega) \end{pmatrix} \tag{5.4}$$

After substitution of these vector components into equation 5.2, the dot product can be simplified into:

$$\vec{a} \cdot \vec{b} = -\cos(\text{AoI}) \sin(\omega). \tag{5.5}$$

Finally, from equations 5.1 and 5.5, the relations between the three different angles can be determined:

$$\cos(\theta_{out}) = -\cos(\text{AoI}) \sin(\omega). \tag{5.6}$$

This leads to the following expression for the undetermined tilt angle ω:

$$\omega = \arcsin\left(-\frac{\cos(\theta_{out})}{\cos(\text{AoI})}\right) \tag{5.7}$$

Thus, this equation is used to determine the value for ω corresponding to the values for AoI (determined in section 4.3) and θ_{out} (determined in section 6.1).

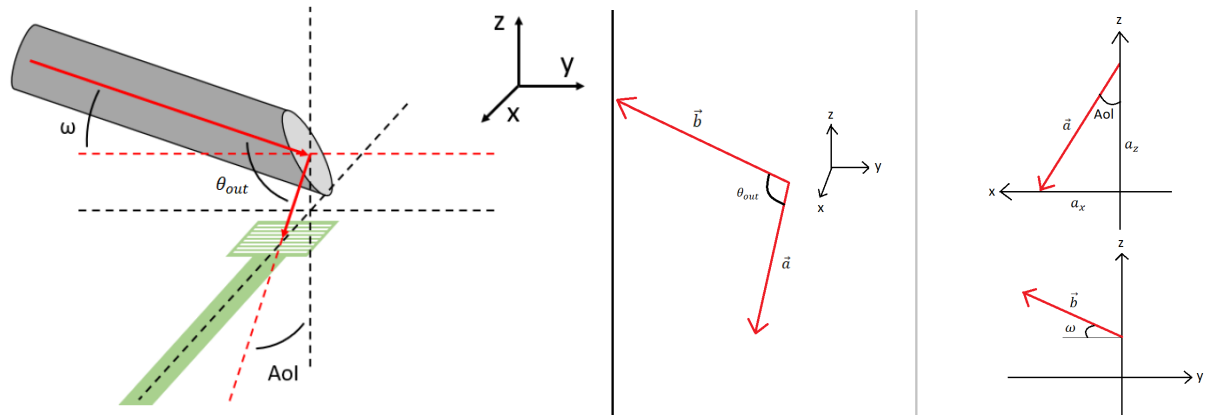

(a) Configuration of the angle polished fiber with output beam incident on the standard IMOS grating coupler, including the definitions of the various angles. Adapted from: [7]

(b) Vector notation of the angle polished fiber configuration.

Figure 5.3: Angle polished fiber configuration

5.2.2 Beam profile measurements

In general, the first step in beam profile measurements of grating couplers is to couple light into the waveguide of the grating coupler structure that is to be measured. Therefore, one of the angle polished fibers is connected to the tunable laser and the fiber is aligned to the relevant input standard IMOS grating coupler on the PIC. As mentioned in the previous section, the rotation angle of the fiber is set to the value of AoI determined from the simulations of section 4.3. Subsequently, the tilt angle of the fiber ω is set to the value calculated with equation 5.7, which also requires the results from the fiber measurements (section 6.1). When these angles are set to their specific values, the rotational degrees of freedom of the fiber rotator stage are fixed and the next step is to align the fiber to the standard IMOS input grating coupler in the three translational degrees of freedom. Therefore, the visible light camera system is used. With the additional white light source on, the visible camera system provides a view of the PIC and the fiber under an angle of 45°. Hence, by bringing the fiber close to its reflection, it can be positioned just above the standard IMOS input grating coupler. An example of this configuration is shown in figure 5.4. The subsequent step is the positioning of the IR camera system above the large grating coupler that is to be measured. By using the two manual stages and the motorized height stage of the IR camera system, the PIC plane with the large grating coupler can be brought into focus. After that, the additional white light source is switched off. If the tunable laser source is then switched on at the right wavelength, the output beam of the large grating coupler is captured by the IR camera system. By slightly adjusting the in plane positions of the fiber rotator stages, the fiber-to-chip coupling can be optimized to obtain maximum signal. If maximum signal is obtained, the output beam of the large grating coupler is measured in the PIC plane, which is the starting point of the measurement, defined as $x = 0$. Subsequently, the height of the IR camera system (x) is increased in small steps (typically 5 µm), with the motorized height stage. After each small increment, the image of the IR camera is captured and saved for analysis. In the analysis beam profile images can be made, from which the beam characteristics, such as the output angle, can be determined.

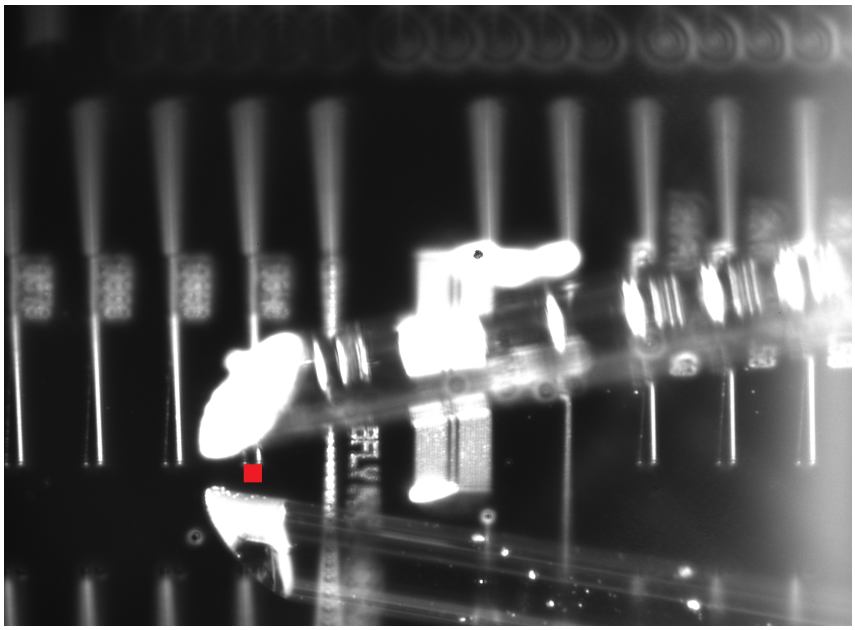

Figure 5.4: An image, captured by the visible light camera system, of the optical fiber in the aligned position. The fiber (top) is brought close to its reflection (bottom), above the standard IMOS grating coupler (red square).

In addition to the measurements on the large grating couplers, beam profile measurements are also performed on the angle polished fibers in order to determine their output angles. The output angles are needed in the calculations for the ideal fiber rotator angles that maximize the coupling. The procedure for beam profile measurement on the fibers is almost identical to the procedure described above, except for the first part. The beam profile measurements of the angle polished fibers start by a reconfiguration of the visible light camera system. The position and orientation of the visible light camera is temporarily changed to align the camera in the horizontal plane, for which a spirit level is used. The tilt angle of the fibers are then adjusted to have the fibers positioned completely horizontal, as accurate as possible. The minimal tilt angle that might still be present in the end can be estimated by simple pixel counting of the camera image, and the measurement results can be corrected for this. After the tilt angle is fixed to have the fiber as horizontal as possible, the fiber is rotated until the tip of the angle polished fiber is exactly at the top side, such that the output beam is directed straight up to the IR camera system. Subsequently, the IR camera system is focused on the tip of the angle polished fiber, which is the starting point of the measurement in this case ($x = 0$). The remainder of the beam profile measurement is then similar as for the measurement on the grating couplers, meaning stepwise increasing the height of the IR camera system and capturing the images for analysis. It can be verified that the rotation angle is set correctly, by checking if the output beam is not moving sideways while increasing the height.

5.2.3 Alignment scan

As mentioned before, the initial plan of performing alignment scan measurements on the PIC alignment sensor prototype could not be executed. For this reason the alignment scan procedure is only briefly discussed, although the complete procedure is complex and extensive. For a description of the complete procedure a reference is made to the thesis of M.R. Otto [7].

In the alignment scan measurement, the tunable laser source is connected to one of the angle polished fibers. This fiber then couples light into the waveguide connected to the emitting grating coupler. As a result, a focused Gaussian beam is emitted from the emitting grating coupler on the PIC towards the IR camera system. Hence, the IR camera system can be used to check the characteristics of the output beam of the emitting grating coupler. Moreover, the tunable laser source can also be connected to the output fiber that is coupled to the output of the beam combiner. This way, both capturing grating couplers will emit a focused Gaussian beam. By blocking the output beam from one of the capturing grating couplers, the characteristics of the output beam of one capturing grating coupler can be determined. Then the characteristics of both the emitting and capturing grating couplers can be compared with the design to verify if they comply with the designed characteristics. Thereafter, the wafer sample with the alignment

marks, which is glued to the bottom of a transparent glass plate, is slid above the PIC at the correct location. However, in order to determine the required position of the alignment marks, an additional calibration step needs to be performed first. Therefore, the glass plate is mounted in reverse position, such that the alignment marks face the IR camera. The position of the alignment marks with respect to certain scale marks on the transparent glass plate are then determined with the IR camera. After this calibration measurement the glass plate position is reversed again, such that the alignment marks face the PIC. This calibration measurement is used to determine the exact position of the alignment marks relative to the scale marks on the glass plate, which are visible from either side.

Subsequently, the IR camera is focused on the center of the PIC and moved up by 10 mm. Then, with the calibration measurement the alignment marks can be positioned in focus of the IR camera. This way, the alignment marks are exactly at the right position, such that it diffracts the Gaussian beam from the emitting grating coupler onto the capturing grating couplers. The diffracted orders are captured by the capturing grating couplers on the PIC. As described in section 2.1, both diffracted orders are interfered on the PIC, resulting in the output signal at the output standard IMOS grating coupler. This signal is coupled to the other angle polished fiber. The signal of the fiber is then measured by connecting it to the photodetector, which is connected to the amplifier. In order to determine the alignment signal, the output signal of the amplifier needs to be stored over time. To enable this data storage over time, an additional compact oscilloscope is arranged. By connecting the amplifier output to this PicoScope 2205A oscilloscope, the alignment signal can be recorded over time, with the associated PicoScope 6 software [45]. This way, the alignment signal can be measured while translating (scanning) the wafer sample in one direction. Finally, if the PIC alignment sensor works as expected, the alignment marker position can be determined from analysis of the alignment scan signal. As elaborated by M.R. Otto, the performance of the PIC alignment sensor is quantified by the repeatability of the distance measurement between two alignment marks that are 10 mm apart [7]. With the current experimental setup the expected repeatability of this distance measurement is $\pm$ 4.3 nm at maximum. This value arises from possible errors in marker position and orientation. For example, the accuracy in the height of the IR camera is verified to be 18.8 µm at maximum [7], which can translate into errors in the height position of the alignment marks of this order. Furthermore, the tilt accuracy of the wafer sample holder is 2 mrad, which also translates into an uncertainty in the orientation of the alignment marks with respect to the PIC. All possible error sources and their effects on the repeatability of the alignment scan are extensively discussed in the thesis of M.R. Otto [7]. It is beyond the scope of this research project to provide more details about the alignment scan measurement, since it could not be performed in this project. As mentioned at the start of this section, for all the information on the alignment scan measurement, a reference is made to the thesis of M.R. Otto [7].

Chapter 6

Experimental results and analysis

In this research project, two different beam profile measurements are performed with the experimental setup discussed in the previous chapter. Beam profile measurements are performed on the angle polished fibers which are used to couple light in and out of the PIC. Additionally, radiation profiles of the large grating couplers on the test PIC from the TU/e, introduced in section 2.2.4, are measured. The results of these two measurements are presented and analyzed individually in the two sections of this chapter.

6.1 Angle polished fibers

In order to couple light into and out of the PIC with the highest possible efficiency, the fibers need to be optimally aligned to the standard IMOS grating couplers. Therefore, it is important to accurately measure the output beam profiles of the angle polished fibers. Since there are two fibers needed to simultaneously couple light into and out of the PIC, both of them need to be characterized. In the remainder of this thesis, the input fiber refers to the fiber clamped in the right rotator (seen from figure 5.1) and the output fiber refers to the fiber clamped in the left rotator. The procedure for the characterization measurements is described in section 5.2.2. The images of the fibers, captured by the visible light camera system, for this measurement configuration, are shown in figure 6.1.

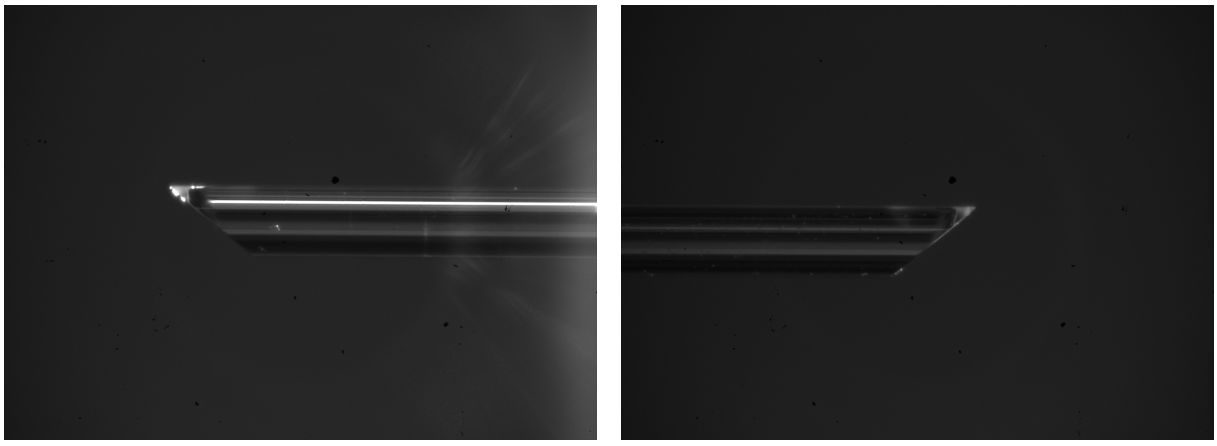

(a) Input fiber (b) Output fiber

Figure 6.1: Images of the angles polished fibers in their characterization measurement position, captured with the visible light camera system.

Since the visible light camera system is horizontally leveled for this measurement by using a spirit level, it can be concluded from figure 6.1 that the fiber still has a minimal tilt angle. This tilt angle can be determined from primitive pixel counting of the edges of the fibers in these images. Therefore, the pixel coordinates of numerous points on both edges of the fibers are determined. This can be done within an uncertainty of approximately 2 pixels with the particular zoom factor of figure 6.1. Thereafter, a linear fit is made through these coordinates to determine the slope of the edge, from which the tilt angle can be determined. The results of both edges are then combined to obtain the final value for the tilt angle

with its associated uncertainty, resulting in:

$$\text{Input fiber: } \omega = (0.41 \pm 0.03)^\circ \tag{6.1}$$

$$\text{Output fiber: } \omega = (-0.32 \pm 0.03)^\circ \tag{6.2}$$

The used sign convention in this case is that the tilt angle ω is defined positive when the fiber tip is tilted upwards with respect to the perfect horizontal position. Furthermore, it is important to mention that in these results it is assumed that the visible light camera system is perfectly horizontally leveled.

For the next step in the accurate characterization of the fiber output beams, the IR camera system is used to perform the beam profile measurements, for which the results are shown in figure 6.2. This figure shows the beam widths at each measured height location of the IR camera (x). The beam width is again defined as the points with an intensity higher than $1/e^2$ of the maximum intensity of that height slice. In this figure, the red arrows indicate the propagation direction of the light inside the fiber.

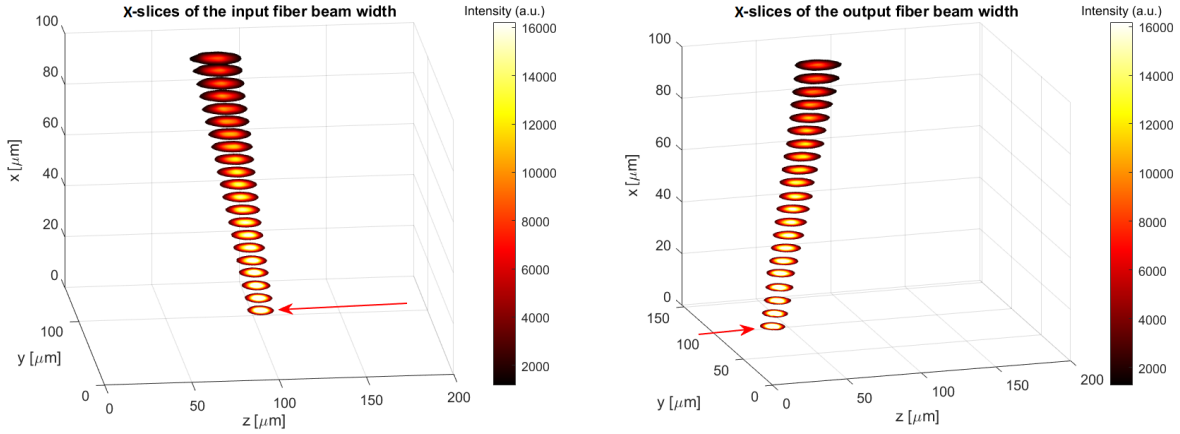

(a) Input fiber

(b) Output fiber

Figure 6.2: Fiber beam widths at different heights (x) above the fiber tip. The red arrows indicate the direction of light propagation inside the fiber.

Figure 6.2 thus provides an accurate representation of the beam propagation out of both fibers. Yet, the results are still discretized (sliced) in the height direction. In order to provide a more intuitive representation of the beam propagation, the discretized height measurements can be interpolated to show the beam propagation in the x-z plane in figure 6.3. Since the fibers are positioned in such a way that the output beam goes straight up, the movement of the beam in the y-direction should be negligible. This is indeed found to be the case when the effects of vibrations and air flows are minimized by reducing the length of the unsupported part of the fiber, which is simply achieved by repositioning the fiber in the fiber rotator. The 2D beam propagation images of figure 6.3 are obtained by interpolating the slices at the y-position of the beam center. Again the red arrows in this figure indicate the direction of light propagation in the fiber.

These beam characterization measurements can be used to accurately determine the beam output angles of both fibers. Figure 6.3 already provides the visualization of this output angle. However, to determine this angle in the most accurate way, the measured intensity profiles of the height slices (figure 6.2) are used. A 2D Gaussian function is used to fit the beam width profiles in order to determine the center position of the beam for all the slices. The final results of this fit procedure are shown in figure 6.4. These figures show the height of the IR camera system focus point above the fiber tip (x) versus the center position in the z-direction resulting from the fit procedure. Subsequently, by fitting a simple linear equation to both figures, the following fit results are obtained:

$$\text{Input fiber: } x = (417.6 \pm 0.5)\ \mu\text{m} - (3.956 \pm 0.006)\ \mu\text{m} \cdot z \tag{6.3}$$

$$\text{Output fiber: } x = (-137.6 \pm 0.4)\ \mu\text{m} + (3.368 \pm 0.008)\ \mu\text{m} \cdot z \tag{6.4}$$

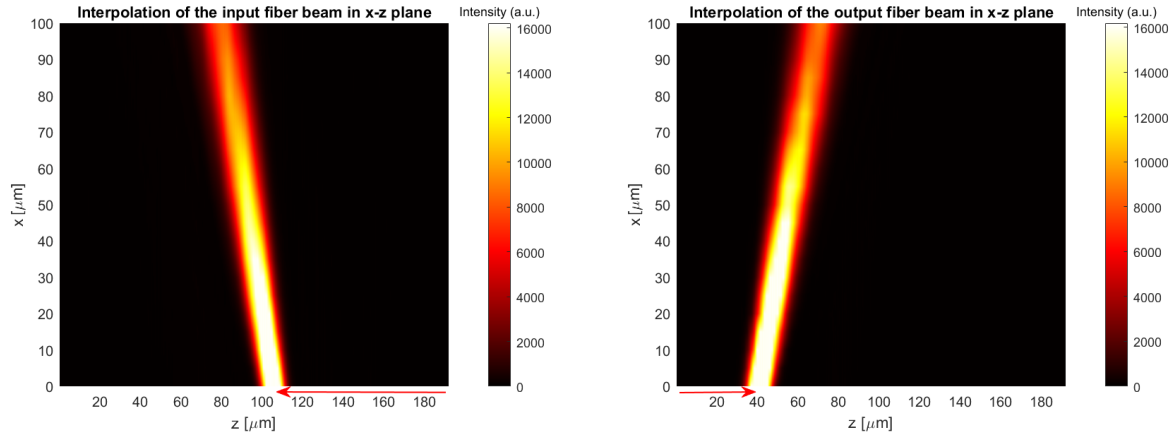

(a) Input fiber (b) Output fiber

Figure 6.3: Beam propagation out of the fibers in the x-z plane at the center position in the y-direction. The red arrows indicate the direction of light propagation inside the fiber.

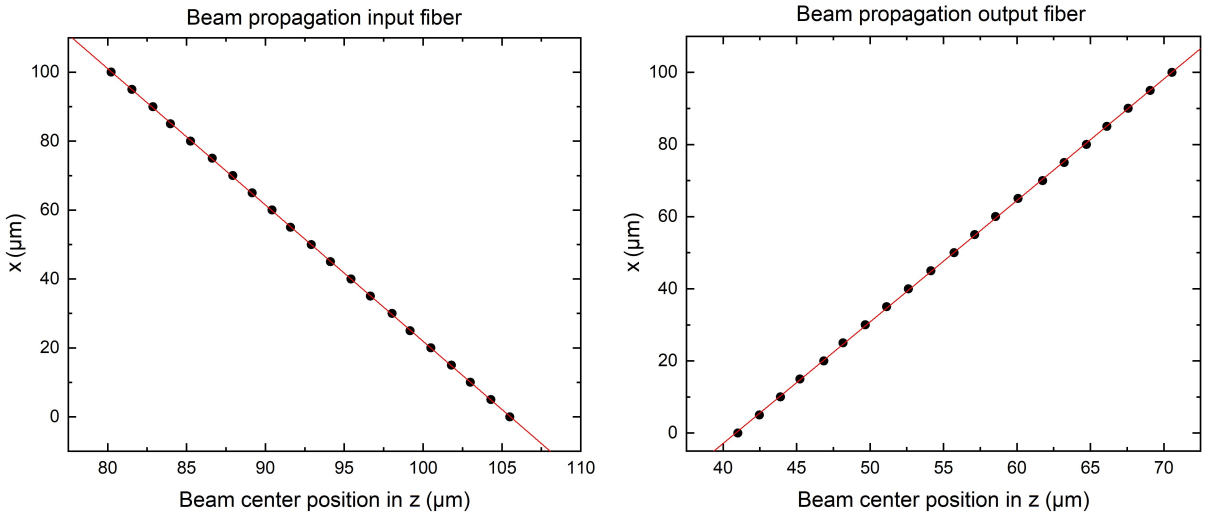

(a) Input fiber (b) Output fiber

Figure 6.4: Height of the focus point of the IR camera system above the fiber tips (x) versus the center position of the beam in the z-direction resulting from the slice measurement fits. Although the uncertainties in both directions are included in the figure, they are not visible due to their small sizes. A linear fit is made through the data points, with the resulting formulas provided in equations 6.3 and 6.4.

The gradient of the linear fits through figure 6.4 can be converted into the beam output angle, which is defined as the angle between the fiber axis and the output beam, as illustrated in figure 5.3a by θ_{out}. Hence, the output angle is equal to 90 ° plus the angle that the output beam makes with the normal to the fiber axis. However, as mentioned before, the fibers still have a minimal tilt angle, which is also visible in figure 6.1. Consequently, the measured output angles are corrected for these tilt angles to find the actual value for θ_{out}. The final values for the output angles of both fibers resulting from these measurements are:

$$\text{Input fiber: } \theta_{out} = (104.59 \pm 0.05)^\circ \tag{6.5}$$

$$\text{Output fiber: } \theta_{out} = (106.21 \pm 0.07)^\circ \tag{6.6}$$

These values are then used to maximize the coupling efficiency of light into and out of the PIC with these specific fibers. As elaborated in section 5.2.1, this beam output angle result are used in combination with the results for the AoI of section 4.3 to determine the determine the exact values for all rotational degrees of freedom of the fibers. The rotation angle of the fiber rotator stages needs to be fixed to the value of equation 4.4. Substitution of this value of AoI and the values for θ_{out} from equations 6.5 and 6.6 into

equation 5.7, then yields a tilt angle of the fiber rotator stages for maximum light coupling of:

$$\text{Input fiber: } \omega = (14.83 \pm 0.08)^\circ \tag{6.7}$$

$$\text{Output fiber: } \omega = (16.5 \pm 0.1)^\circ \tag{6.8}$$

Additionally, the beam output angle values can be converted into a value for the polished angle of the fibers. The calculation behind this conversion is provided in appendix C and it eventually leads to the following values for the polished angles of both fibers:

$$\text{Input fiber: } \theta_{fiber} = (39.98 \pm 0.02)^\circ \tag{6.9}$$

$$\text{Output fiber: } \theta_{fiber} = (39.43 \pm 0.02)^\circ \tag{6.10}$$

These values for the polished angles of the fibers are in agreement with the specifications of the manufacturer: that the fibers have a polished angle of $(40.5 \pm 1.5)^\circ$.

6.2 Grating coupler beam profiles

The procedure for the beam profile measurements ,discussed in section 5.2.2, is also applied to the large grating couplers on the TU/e test PIC. The purpose of this measurement is twofold: it will demonstrate the capability of the experimental setup to perform beam profile measurements on large grating couplers and the measured profiles can be compared with the results of the BA-GCE model presented in section 4.2. The beam profile measurements are performed on the 200 µm long uniform grating couplers with FFs of 0.8, 0.65 and 0.5. The input fiber is aligned to the standard IMOS input grating coupler by maximizing the signal out of the standard IMOS output grating coupler, as discussed in section 5.2.2. In this step, the IR camera is focused on the standard IMOS output grating coupler and this position is taken as the starting point in y and z for the beam profile measurement. In addition, the beam that is coming out of the standard IMOS output grating coupler is blocked by a piece of black paper attached to the bottom of a micropositioner in order to prevent this signal from interfering with the output beam of the large grating coupler. Thereafter, the IR camera is moved up by the motorized actuator by 17 or 20 mm for the two different measurements. Through translation of the manual IR camera stage and by combining all the images, the final beam profiles at a certain height above the PIC can be determined. Accurate alignment of the FoV plane and the translation plane of the IR camera system to the PIC, as discussed in section 5.1, is crucial. The experimental results for the large grating coupler with FF = 0.65 are shown in figure 6.5.

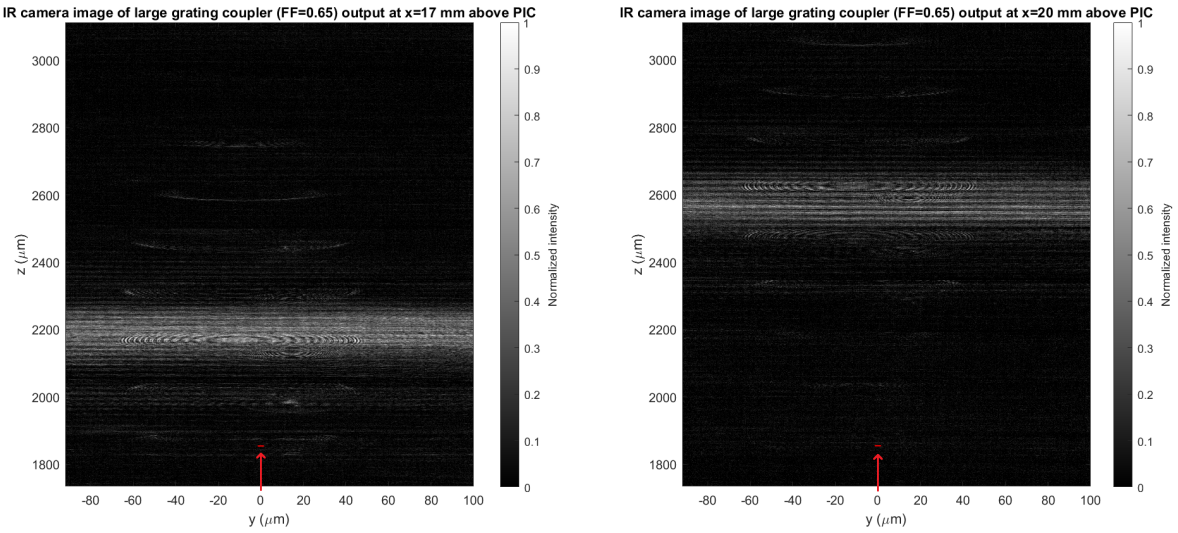

Figure 6.5: Experimentally measured beam profiles of the large grating coupler with $N = 333$ and FF = 0.65, at 17 mm (left) and 20 mm (right) above the PIC. The red arrow refers to the propagation direction of the light in the waveguide and in the large grating coupler. The small red line indicates the landmark point: the transition from waveguide to standard IMOS output grating coupler (see figure 2.7).

The axes values in figure 6.5 are with respect to the origin, which is defined at start of the first grating groove. These values are determined from the landmark point, which is the transition point from the waveguide to the standard IMOS output grating coupler, which is indicated by the small red line in figure 6.5. The position of this landmark point is determined from the IR camera image captured at the starting position. From the PIC layout it is known that the distance between the start of the first grating groove and the landmark point is 1854.7 µm. This way, the axes values with respect to the origin can be determined, which makes the coordinate system identical to the one in the BA-GCE model (with $z_0 = 0$), thereby simplifying the comparison between both results. The resulting beam profiles for the large grating couplers with the other two FF values are similar, as was the case in section 4.2. The measured beams all have a wide peak width in the y-direction and only a limited peak width in the z-direction. This is as expected from the paper of Y. Wang et al. [36], since this is the purpose of the designed beam steerer devices. Moreover, the z-direction is also the direction of interest for the model comparison due to the 2D nature of the BA-GCE model.

The output beams from the large grating couplers can be fit with a Gaussian function according to the paper of Y. Wang et al. [36], for which the test PIC was specifically designed and characterized. The fit of this Gaussian function to the center slice of the beam profile measurements results in the peak characteristic values that are presented in table 6.1. For comparison, this table also includes the results from the BA-GCE model of section 4.2. From table 6.1 it can be concluded that significant differences exist between the measured intensity profiles and the BA-GCE model intensity profiles.

Grating coupler FF	x (mm)	Peak characteristics			
		Experimental measurements		BA-GCE model	
		Position z (µm)	FWHM (µm)	Position z (µm)	FWHM (µm)
0.5	17	2160 ± 2	196 ± 4	2516.78	120.701
	20	2544 ± 2	187 ± 3	2960.91	142.001
0.65	17	2192 ± 1	145 ± 3	2544.12	120.788
	20	2573 ± 2	161 ± 5	2993.07	142.104
0.8	17	2214 ± 2	134 ± 3	2572.14	120.873
	20	2609 ± 2	201 ± 5	3026.05	142.203

Table 6.1: Values for the peak position and FWHM of the field intensity profiles at 17 and 20 mm above the PIC for the three different large grating coupler variants (different in FF). The table includes the experimental results and the results from the BA-GCE model as introduced in section 4.2.

The experimental measurement results are computed by assuming that the captured images are precisely aligned. However, since the minimum scale reading of the manual translation stage of the IR camera system is only 10 µm, it is expected that this will not be the case. The resolution of the translation stage could easily be improved by controlling it with a high resolution motorized actuator. Nonetheless, the manual translation of the current stages would only result in additional inaccuracies of a few µm, thus it does not explain the large differences observed in table 6.1. Another issue which reduces the quality and accuracy of the measurements, is the presence of interference features in the beam profiles. It can be seen in figure 6.5 that there are multiple interference patterns visible in the measured beam profiles. Similar interference effects are also visible in the measured beam profiles of the large grating couplers with the other two FF values. There are two different types of interference patterns which also have different causes. In figure 6.5, interference rings and interference lines can be identified. Although the interference rings appear to have an elliptical shape in figure 6.5, they are circular, as the ellipticity is simply caused by the difference in aspect ratio of the two axes. The interference rings should be caused by the IR camera system, because they always appear at the exact same position in the IR camera image. Therefore, there are two probable causes for these interference rings. Firstly, interference rings can be caused by the presence of dust particles on the objective of the IR camera system. Even though the setup is in the cleanroom environment, dust particles can enter the room through humans or it might have happened during the movement of the experimental setup. Secondly, the interference rings can be caused by the interaction of the light with the cover glass of the IR camera sensor. Thus, in order to minimize, or ideally completely eliminate these interference rings, the IR camera objective should be cleaned to remove dust particles. This requires dedicated cleaning equipment, which was unfortunately not yet available or operational during this project. If this objective cleaning does not eliminate all the interference rings, the cover glass of the IR camera sensor should be removed. However, this is a challenging operation with high risk of damage. Another obvious solution would then be to arrange a new IR camera system.

Besides these interference rings, the beam profile measurements also show straight interference lines. These interference lines are caused by the interference of the output beam of the large grating coupler with another beam. As mentioned before, the beam out of the standard IMOS output grating coupler is blocked, so that cannot cause the interference lines. Instead, the interference lines are caused by the reflected light of the input fiber. Since a different standard IMOS input grating coupler is used in the TU/e test PIC compared to the one on the PIC alignment sensor, the calculations for ideal light coupling into the PIC (which are made in the previous section) are not valid for the test PIC. Furthermore, due to the 45° orientation of the visible light camera system, it is difficult to determine the exact height of the fiber above the standard IMOS input grating coupler. For these reasons, the established coupling between the input fiber and the standard IMOS input grating coupler will not be ideal. Hence, reflection of the light from the input fiber on the standard IMOS input grating coupler will occur. These reflected beams will then interfere with the output beam of the large grating couplers, causing interference lines in the measured IR camera images. The fact that the interference line pattern changes when the position of the input fiber is adjusted, supports this explanation. Evidently, this effect can be minimized by maximizing the coupling between the fiber and the standard IMOS input grating coupler. Therefore, the outcouple angle of this specific standard IMOS input grating coupler should be accurately measured, as well as the output angle of the specific fiber, as in section 6.1. Then, the calculations in this thesis can be used to achieve maximum coupling efficiency. However, due to an insufficient amount of time, and since the PIC alignment sensor will have different standard IMOS grating couplers, this advanced investigation is not performed in this research project. The limited resolution of the manual translation stage and the presence of the interference patterns both reduce the quality and accuracy of the final results. Yet, it is still important to analyze these results in more detail.

From the peak positions of table 6.1, the beam output angles of the grating couplers can be determined. Simple trigonometric calculations lead to the beam output angles provided in table 6.2. The table includes two different values for the beam output angle of the experimental measurements: one value is calculated from the peak positions at 17 mm and the other value is calculated from the peak positions at 20 mm. For the BA-GCE model only one value is provided, since every position results in the same angle in that case.

Grating coupler FF	Beam output angle (°)		
	Experimental measurements		BA-GCE model
	From position at x=17 mm	From position at x=20 mm	
0.5	7.241 ± 0.007	7.249 ± 0.006	8.421
0.65	7.347 ± 0.004	7.331 ± 0.006	8.511
0.8	7.420 ± 0.007	7.432 ± 0.006	8.604

Table 6.2: Beam output angles from the large grating couplers determined from the results of table 6.1. The beam output angles resulting from the experimental measurements are calculated from the measured positions at the two different distances (17 and 20 mm) and only a single output angle results from the BA-GCE model.

The two values for the output angle following from the experimental measurements are consistent, considering that the small differences between them can be caused by the two effects discussed in the previous paragraph. Since both experimental measurements (at 17 and 20 mm) are independent of each other, it can be concluded from the consistency of the results that the large differences in peak position values in table 6.1 are caused by a difference in the output angle between the experiment and the model. The most probable explanation for this observed difference in the output angle is that there are deviations of the actual fabricated structure from the initial design. The equivalent structure that is inserted in the BA-GCE model is based on this design and according to the grating equation for uniform grating (equation 2.11), the initial design indeed has an output angle close to 8.5°. Therefore, the measured structure must deviate from the initial design to result in a different output angle. According to the grating equation, the observed difference in output angle of table 6.2 can, for example, already be caused by a deviation of the grating period of less than 5 nm from the designed period of 600 nm. Indeed, it is possible that fabrication and processing steps lead to deviations of the grating parameters compared to the initial design, thereby changing the effective refractive index, which will also change the output angle according to equation 2.11. Another observation in support of this explanation is obtained from the results of Y. Wang et al. [36]. In this paper, which measured the same large grating coupler structures,

the intensity peak of the 2000 µm long grating coupler with FF = 0.8 is measured at approximately 10.9°, for a wavelength of 1550 nm. Since the number of grating lines only has a negligible effect on the peak position, a similar output angle would be expected for the 200 µm long variant. However, both the experimental results as well as the BA-GCE model results lead to a significantly different output angle. This proves that there are variations within the large grating coupler structures over the PIC cells. Furthermore, another finding in support of this explanation is that the experimentally determined output angles increase for grating couplers with higher FF values, with a similar fraction as according to the BA-GCE model. This hints at the existence of structural deviations from the initial design, since all three grating coupler variants have a similar difference in output angle with the model.

Moreover, a diverging beam is expected to be emitted from uniform grating couplers, meaning that the FWHM should increase with the height, as in the BA-GCE model results. However, this is not the case in the experimental results for the grating coupler with FF = 0.5, which is therefore unexpected. Since it is a rather small difference, it can still be caused by the reduced quality of the results due to the limited resolution of the IR camera translation stage and especially due to the interference effects. The unexpected large relative spread in the FWHM values compared to the model results also indicated a reduced quality of these parameter values, since such a spread is not present in the peak position results. Furthermore, also for this parameter, a deviation of the fabricated structure from the initial design can cause these differences.

Another weakness of this experimental verification is that the BA-GCE model results are calculated indirectly, by first finding an equivalent structure with Lumerical, as explained in section 4.2 and appendix B. This is currently the best available alternative to circumvent the problem that the model is developed for grating couplers that are etched into the waveguide layer only. Although this is the best alternative, it makes the assessment of the model in this way rather questionable. Since the equivalent structure is based on the results of Lumerical simulations, it can be argued that this assessment is more about comparing Lumerical simulations with experimental results. Thus, the found differences in the peak characteristics indicate a difference between Lumerical results and the experimental results. Probable explanations for these observed differences are already provided in the discussion above.

Overall, it is hard to draw explicit conclusions about the performance of the BA-GCE model based on this experimental verification, neither positive nor negative assessments. There are two main reasons for this conclusion. Firstly, the results indicate differences between the actual measured large grating coupler structures and the simulated ones. Secondly, the comparison with the model is indirect, since it is based on Lumerical results. Fortunately, besides the aforementioned ways to improve the accuracy of the translation stages and to minimize the interference effects, there are alternative ways to improve the reliability of experimental comparisons to the BA-GCE model in the future. For example, an extensive inspection of the measured large grating couplers can be performed to verify grating parameter values. This would require high resolution microscopy equipment, such as electron microscopes. This way, the model can be made to simulate exactly the same structure as the one which is measured. In addition, large grating couplers with their gratings etched into the waveguide layer can be fabricated to avoid the additional complicating step of finding equivalent structures for the BA-GCE model. Then, the model could be used to simulate the measured structure directly. Lastly, it is surely a recommendation for further improvement of the BA-GCE model to develop a variant which is able to simulate radiation patterns of grating couplers etched into the superstrate layer. This would also avoid the equivalent structure step and thereby provide direct comparison with the experimental results. It is strongly recommended to follow one or more of these suggestions for improvement, such that a reliable experimental verification of the BA-GCE model can take place.

Chapter 7

Conclusions and outlook

BA-GCE model

In this research project, the novel analytic BA-GCE model has been developed. It is derived by improving and extending Flory's model [1], which models the grating coupler as an unperturbed homogeneous waveguide plus the refractive index perturbation introduced by the grating structure. The scattered field as a result of the refractive index perturbation of each grating groove is modelled as a collection of point sources, which all emit radiation according to the Green's function. The novelty of the BA-GCE model is created by the applied adaptations and extensions. The model is adapted to include the exponential decay of the light intensity in the waveguide due to the light outcoupling. In addition, the range of applicability of the model is extended to grating couplers with asymmetric waveguide structures and period apodization. The main advantage of this model is that it enables fast computation of radiation profiles for grating couplers of any size. Besides that, another vital advantage of the model is its transparency and intuitiveness, hereby clearly reflecting the underlying physics.

After an extensive benchmarking procedure, it was concluded that the BA-GCE model has a limited region of validity due to the two approximations that are applied in the derivation: the first order Born approximation and the far field approximation. The Born approximation is only valid for weak grating couplers which have a fractional energy loss factor smaller than ζ. However, the exact value for ζ is application-specific and depends on the required level of accuracy. Similarly, the distance at which the far field approximation is valid also depends on the application and the desired level of accuracy. The benchmarking procedure seems to show promising results, since the BA-GCE model results are in good agreement with both the theoretical expectations and the Lumerical FDTD [9] results. After the inclusion of the exponential decay adaptation and the asymmetric structure extension, the relative differences in the peak positions of the radiated spectra between the model and Lumerical, normalized by the FWHM, are still within 2.5%. In addition, it was found that the deviation of the BA-GCE model results from the Lumerical results increased when the steps in the period apodization are increased. This is caused by the fact that an increase of the period apodization steps increases the error induced by the Born approximation. Nevertheless, it can be concluded that the BA-GCE model shows promising results, as it is able to accurately determine normalized radiation profiles within its region of validity. Another deficiency of the model, besides the limited region of validity, is the inaccuracy that is present in the absolute values, which is why normalized radiation profiles are used. This inaccuracy can be explained by the absence of reflections in the model. Therefore, a suggestion for improvement of the model is to perform additional research in order to find a correction method for this absolute value inaccuracy.

The importance of continuing the development of the BA-GCE model built on the foundation of the current model is non-negligible. Hence, focusing on further improvements and extensions of the BA-GCE model is strongly recommended. Since the main purpose of the BA-GCE model, within the PIC alignment sensor project, is to aid in the design optimization process of the large area grating couplers, a valuable extension would be to develop optimization scripts for focusing grating couplers. However, in order to simplify the design process of focusing grating couplers, the model has to be extended to allow for grating groove apodization alongside the period apodization which is already included in the current model. Furthermore, the third recommended extension option is to develop a variant of the BA-GCE model for grating couplers that are etched into the superstrate layer. Together with the extension for grating groove width apodization, this would then enable direct computation of the normalized radiation

profiles from the large area grating couplers of the PIC alignment sensor. Lastly, another extension option would be to convert the current 2D model into a 3D model.

In addition, experimental verification of the BA-GCE model was performed. Unfortunately, no explicit conclusions could be drawn from this, due to the indirectness of the comparison and the deviation of the experimentally measured grating coupler structures from their initial design. Therefore, reliable experimental verification can only be achieved if the variant of the BA-GCE model with grating couplers etched into the superstrate layer would be developed, and if an extensive inspection of the actual fabricated structure is performed.

Experimental setup

Besides the development and verification of the BA-GCE model, the other focus point of this study is the preparation of the experimental setup for the measurements on the PIC alignment sensor. The experimental setup has been disassembled, rebuilt and re-calibrated and is now completely prepared to perform the measurements. The procedure to receive the required safety label for the setup has been successfully finished and extensive operation manuals have been passed to the future users, hereby allowing for immediate characterization measurements once the PIC alignment sensor is delivered. Furthermore, fiber measurements resulted in output angles of $(104.59 \pm 0.05)^\circ$ and $(106.21 \pm 0.07)^\circ$ for respectively the input and output fibers. These fiber measurements can be used together with the simulations and trigonometric calculations that are performed in this project, to predetermine the required fiber angles in order to achieve maximum coupling efficiency in the experimental measurements.

Although the experimental verification of the BA-GCE model has not yet led to valuable conclusions, it has demonstrated the capability of the experimental setup to perform beam profile measurements. The results show multiple interference features, which are not beneficial for the quality of the experimental measurements. In order to reduce these interference effects, it is strongly recommended to clean the IR camera objective with dedicated cleaning equipment and to use this study to maximize the light incoupling, hereby minimizing reflections that can cause these interference effects. Furthermore, as the experimental verification results indicate that the fabricated PIC structures can deviate from the initial design, it is recommended to conduct additional inspections with high resolution microscopy equipment to verify the structure parameters of the PIC alignment sensor.

Final recommendations

Overall, the current BA-GCE model shows promising results for the simulation of normalized radiation profiles from grating couplers within its region of validity. With some further improvements and extensions, this model may ultimately result in an accurate analytic model which can be used in the design process of focusing grating couplers. There is a strong demand for such an analytic model that is able to simulate large grating couplers, for which conventional rigorous simulation methods are too computationally expensive. The application range for this model will not be limited to the PIC alignment sensor, as it will be valuable in the design process of any PIC that requires large area focusing grating couplers. Apart from the continuation of the development of the BA-GCE model, the other important follow-up action of this research project is to perform the measurements on the PIC alignment sensor prototype with the experimental setup, once the PIC is delivered, taking into account the recommendations that are proposed in this chapter.

List of abbreviations

1D - One-Dimensional

2D - Two-Dimensional

3D - Three-Dimensional

BA-GCE - Born Approximation applied to computation of Grating Coupler Emission

BCB - Benzocyclobutene

CD - Critical Dimension

CDU - Critical Dimension Uniformity

CMMM - Complex Mode Matching Method

CMT - Coupled Mode Theory

FDTD - Finite Difference Time Domain

FF - Fill Factor

FoV - Field of View

FTIR - Frustrated Total Internal Reflection

FWHM - Full Width at Half Maximum

IC - Integrated Circuit

IMOS - Indium-phosphide-Membrane-On-Silicon

InP - Indium-Phosphide

IR - Infrared

MMM - Mode Matching Method

PIC - Photonic Integrated Circuit

SiO_2 - Silicon dioxide

TE - Transverse Electric

TIR - Total Internal Reflection

TM - Transverse Magnetic

TU/e - Eindhoven University of Technology

VCM - Volume Current Method

Bibliography

[1] C. A. Flory, "Analysis of directional grating-coupled radiation in waveguide structures," *IEEE Journal of Quantum Electronics*, vol. 40, no. 7, pp. 949–957, 2004.

[2] G. E. Moore, "Cramming more components onto integrated circuits," *Electronics*, vol. 38, no. 8, pp. 114–119, 1965.

[3] A. J. den Boef, "Optical wafer metrology sensors for process-robust CD and overlay control in semiconductor device manufacturing," *Surface Topography: Metrology and Properties*, vol. 4, no. 023001, 2016.

[4] I. D. Setija, "Optical Metrology for Advanced Lithography Systems." PowerPoint Presentation, 2021. University of Technology Eindhoven, Course: Optical Sensing and Metrology (5LHB0).

[5] D. Brown, D. Friedrich, F. Brückner, L. Carbone, R. Schnabel, and A. Freise, "Invariance of waveguide grating mirrors to lateral displacement phase shifts," *Optics letters*, vol. 38, no. 11, pp. 1844–1846, 2013.

[6] B. Menchtchikov, R. Socha, C. Zheng, S. Raghunathan, I. Aarts, K. Shome, J. Lee, C. de Ruiter, M. Rijpstra, H. Megens, *et al.*, "Reduction in overlay error from mark asymmetry using simulation, orion, and alignment models," in *Optical Microlithography XXXI*, vol. 10587, p. 105870C, International Society for Optics and Photonics, 2018.

[7] M. R. Otto, "An experimental setup for photonic integrated circuit alignment sensors." Master Thesis, 2021. Delft University of Technology: Department of Precision and Microsystems Engineering.

[8] J. P. de Graaf and I. D. Setija, "Integrated optical sensor for diffraction based wafer alignment." Master Thesis, 2020. Eindhoven University of Technology, ASML internal version.

[9] Lumerical Inc., "Lumerical FDTD solver," 2022.

[10] E. Hecht, *Optics*. Pearson, 5th ed., 2016.

[11] R. Menzel, *Photonics: Linear and Nonlinear Interactions of Laser Light and Matter*. Springer Science & Business Media, 2nd ed., 2007.

[12] T. Erdogan, "The Grating Equation." PGL Technical Note, 2022. Plymouth Grating Laboratory.

[13] V. D. Calzadilla, "Metal nanocavity light sources integrated with passive waveguide components," 2016. Eindhoven University of Technology: Department of Electrical Engineering.

[14] Y. Jiao, J. van der Tol, V. Pogoretskii, J. van Engelen, A. A. Kashi, S. Reniers, Y. Wang, X. Zhao, W. Yao, T. Liu, *et al.*, "Indium Phosphide Membrane Nanophotonic Integrated Circuits on Silicon," *Physica Status Solidi (a)*, vol. 217, no. 3, p. 1900606, 2020.

[15] S. F. G. Reniers, "Integration of a polarization converter on the active-passive IMOS platform," 2022. Eindhoven Universtiy of Technology: Department of Electrical Engineering.

[16] J. J. van der Tol, Y. Jiao, J. P. Van Engelen, V. Pogoretskiy, A. A. Kashi, and K. Williams, "InP membrane on silicon (IMOS) photonics," *IEEE Journal of Quantum Electronics*, vol. 56, no. 1, pp. 1–7, 2019.

[17] J. van der Tol, J. Pello, S. Bhat, Y. Jiao, D. Heiss, G. Roelkens, H. Ambrosius, and M. Smit, "Photonic integration in indium-phosphide membranes on silicon (IMOS)," in *Integrated Optics: Devices, Materials, and Technologies XVIII*, vol. 8988, p. 89880M, International Society for Optics and Photonics, 2014.

[18] A. E. C. van den Bosch, "Extreme Distance Focusing Grating Coupler Design and Novel Simulation Model." Master Thesis, 2020. Eindhoven University of Technology.

[19] R. G. Hunsperger, *Integrated Optics: Theory and Technology*. Springer Science & Business Media, 6th ed., 2009.

[20] R. Marchetti, C. Lacava, L. Carroll, K. Gradkowski, and P. Minzioni, "Coupling strategies for silicon photonics integrated chips," *Photonics Research*, vol. 7, no. 2, pp. 201–239, 2019.

[21] J. D. Jackson, *Classical Electrodynamics*. John Willey & Sons, Inc., third ed., 1999.

[22] K. R. Harper, *Theory, design, and fabrication of diffractive grating coupler for slab waveguide*. Brigham Young University, 2003.

[23] L. Chrostowski and M. Hochberg, *Silicon photonics design: from devices to systems*. Cambridge University Press, 2015.

[24] S. Ura, T. Fujii, T. Suhara, and H. Nishihara, "Efficiency-enhanced third-order grating coupler," *Applied optics*, vol. 38, no. 14, pp. 3003–3007, 1999.

[25] R. Waldhäusl, B. Schnabel, P. Dannberg, E.-B. Kley, A. Bräuer, and W. Karthe, "Efficient coupling into polymer waveguides by gratings," *Applied optics*, vol. 36, no. 36, pp. 9383–9390, 1997.

[26] R. Marchetti, C. Lacava, A. Khokhar, X. Chen, I. Cristiani, D. J. Richardson, G. T. Reed, P. Petropoulos, and P. Minzioni, "High-efficiency grating-couplers: demonstration of a new design strategy," *Scientific Reports*, vol. 7, no. 1, pp. 1–8, 2017.

[27] D. Taillaert, H. Chong, P. I. Borel, L. H. Frandsen, R. M. De La Rue, and R. Baets, "A compact two-dimensional grating coupler used as a polarization splitter," *IEEE Photonics Technology Letters*, vol. 15, no. 9, pp. 1249–1251, 2003.

[28] D. Taillaert, F. Van Laere, M. Ayre, W. Bogaerts, D. Van Thourhout, P. Bienstman, and R. Baets, "Grating couplers for coupling between optical fibers and nanophotonic waveguides," *Japanese Journal of Applied Physics*, vol. 45, no. 8R, p. 6071, 2006.

[29] K. K. Mehta and R. J. Ram, "Precise and diffraction-limited waveguide-to-free-space focusing gratings," *Scientific reports*, vol. 7, no. 1, pp. 1–8, 2017.

[30] H. Becker, C. J. Krückel, D. Van Thourhout, and M. J. Heck, "Out-of-plane focusing grating couplers for silicon photonics integration with optical mram technology," *IEEE Journal of Selected Topics in Quantum Electronics*, vol. 26, no. 2, pp. 1–8, 2019.

[31] T. Tamir and S.-T. Peng, "Analysis and design of grating couplers," *Applied physics*, vol. 14, no. 3, pp. 235–254, 1977.

[32] K. Ogawa, W. Chang, B. Sopori, and F. Rosenbaum, "A theoretical analysis of etched grating couplers for integrated optics," *IEEE Journal of Quantum Electronics*, vol. 9, no. 1, pp. 29–42, 1973.

[33] C. Oton, "Long-working-distance grating coupler for integrated optical devices," *IEEE Photonics Journal*, vol. 8, no. 1, pp. 1–8, 2015.

[34] Y. Chen, R. Halir, Í. Molina-Fernández, P. Cheben, and J.-J. He, "High-efficiency apodized-imaging chip-fiber grating coupler for silicon nitride waveguides," *Optics letters*, vol. 41, no. 21, pp. 5059–5062, 2016.

[35] H. Xu, C. Sun, J. Zhao, L. Du, X. Xu, and C. Zhang, "Efficient modeling method for emitting focusing grating coupler based on complex mode matching and effective index method," *JOSA A*, vol. 39, no. 1, pp. 32–36, 2022.

[36] Y. Wang, J. P. van Engelen, S. F. Reniers, M. B. van Rijn, X. Zhang, Z. Cao, V. Dolores-Calzadilla, K. A. Williams, M. K. Smit, and Y. Jiao, "Inp-based grating antennas for high-resolution optical beam steering," *IEEE Journal of Selected Topics in Quantum Electronics*, vol. 27, no. 1, pp. 1–7, 2019.

[37] M. Kuznetsov and H. Haus, "Radiation loss in dielectric waveguide structures by the volume current method," *IEEE Journal of Quantum Electronics*, vol. 19, no. 10, pp. 1505–1514, 1983.

[38] U. Hohenester, *Nano and Quantum Optics*. Springer, 2020.

[39] L. Novotny and B. Hecht, *Principles of nano-optics*. Cambridge university press, 2012.

[40] G. B. Arfken, H. J. Weber, and F. E. Harris, *Mathematical methods for physicists*. Academic Press Elsevier, seventh ed., 2012.

[41] C. Pollock and M. Lipson, *Integrated photonics*, vol. 20. Springer, 2003.

[42] J. M. Liu, *Photonic devices*. Cambridge University Press, 2009.

[43] Wolfram Research, Inc., "Wolfram Mathematica 12.2," 2022.

[44] Lumerical Inc., "Lumerical MODE solver," 2022.

[45] Pico Technology Limited, "PicoScope 6," 2022.

[46] I. H. Malitson, "Interspecimen comparison of the refractive index of fused silica," *Josa*, vol. 55, no. 10, pp. 1205–1209, 1965.

Appendices

Appendix A: Mathematica script BA-GCE model

This appendix includes the Mathematica [43] script with the main calculations behind the BA-GCE model, which is explained in chapter 3.

Constants and parameter values

```
ClearAll["`*"]
(* Physical Constants *)
nm = 10^(-9); (* Nanometer *)
μ0 = 4 * π * 10^(-7); (* Vacuum permeability *)
ε0 = 8.85419 * 10^(-12); (* Vacuum permittivity *)

(* Grating structure parameters *)
d1 = 100 * nm;(* Depth of the grating grooves (etch depth) *)
h = 1000 * nm;(* Height of the waveguide *)
w1 = 52.5 * nm; (* Grating groove width *)
ε1 = 12.96; (* Dielectric constant (= relative permittivity) of waveguide medium *)
ε2 = 11.56;(* Dielectric constant superstrate *)
ε3 = 11.56;(* Dielectric constant substrate *)
Ng = 100;(* Number of grating grooves *)
z0 = 0; (* Z-coordinate of first grating groove *)
λ0 = 880 * nm ;(* Vacuum wavelength *)
E0 = 1 ;(* Electric field amplitude (in V/m) *)

(* Calculated constants *)
k0 = 2 * π / λ0; (* Vacuum wavenumber *)
ω = 2 * π / (λ0 * Sqrt[ε0 * μ0]); (* Angular frequency *)
ksup = Sqrt[ε2] * k0 ;(* Background wavenumber superstrate *)
ksub = Sqrt[ε3] * k0;
(* Background wavenumber substrate *)
```

Grating Period (only run the correct one)

```
(* Case 1: constant grating period *)
Λ = 210 * nm ;

(* Case 2: linearly varying grating period *)
Λ1 = 200 * nm; (* Period of first grating element *)
dΛ = 1 * nm; (* Linear change of grating period for each consecutive grating element *)
Λ = Reap[Do[Sow[N[Λ1 + dΛ * (j - 1)]], {j, Ng}]][[2, 1]];
(* Makes a list of the grating periods of all consecutive grating elements *)

(* Case 3: random varying grating period *)
Λ1 = 200 * nm;(* Period of first grating element *)
Λ2 = 205 * nm;(* Period of second grating element *)
Λ3 = 198 * nm;(* Period of third grating element *)
Λ4 = 174 * nm; (* Period of fourth grating element *)
(* And so on *)
(* The periods of each grating element can be inserted manually or through some script,
as long as the value of the grating period of each element is included in the final expression for Λ *)
 Λ = {Λ1, Λ2, Λ3, Λ4, ...};
```

Solving for the wavenumber and decay constants

```
βfunc[κ_] := Sqrt[k0^2 * ε1 - κ^2]; (* From the relation between the parallel (β) and transverse (κ) components of the guided mode *)
κmax = Sqrt[k0^2 * ε1 - k0^2 * Max[ε2, ε3]]; (* Maximum allowed transverse wavevector component of guided mode *)
γ2func[κ_] := Sqrt[k0^2 * (ε1 - ε2) - κ^2]; (* Decay constant in superstrate (medium 2) *)
γ3func[κ_] := Sqrt[k0^2 * (ε1 - ε3) - κ^2]; (* Decay constant in substrate (medium 3) *)
Plot[{Tan[κ * h], κ * (γ3func[κ] + γ2func[κ]) / (κ^2 - γ2func[κ] * γ3func[κ])}, {κ, 0, κmax}, PlotRange → {-10, 10}, PlotLegends → "Expressions"]

sol = FindRoot[Tan[κ * h] == κ * (γ2func[κ] + γ3func[κ]) / (κ^2 - γ2func[κ] * γ3func[κ]), {κ, 2100000}]; (* The last number provides the estimation for the κ solution,
can be checked with the plot *)
κsol = κ /. sol[[1]] (* Provides the solution of the eigenvalue equation for κ, using the relations specified above *)
β = βfunc[κsol]; (* Solution for β *)
γ2 = γ2func[κsol]; (* Solution for γ2 *)
γ3 = γ3func[κsol]; (* Solution for γ3 *)
ϕ = N[1/2 * ArcTan[κsol * (γ3 - γ2) / (κsol^2 + γ2 * γ3)]]; (* Value of the phase factor ϕ following from the eigenvalue equation and the values above.
  This is for the fundamental (n=0) mode *)
(* Not used now, but higher order modes would give an additional factor of n*π/2 in front: ϕn=n*π/2+N[1/2*ArcTan[κsol*(γ3-γ2)/(κsol^2+γ2*γ3)]] *)

(* A plot is made to check if the solution for κ is indeed refers to the fundamental mode *)
```

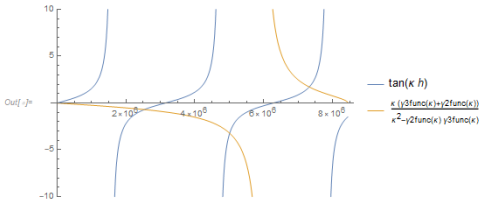

Initial script factors (part 1)

```
(* rad=input ϑ in radians, deg=input ϑ in degree *)
(* Superstrate *)
(* x-integral *)
ϑsupRad[ϑ_] := (d1 / 2) * (Exp[I * ((h - d1) / 2) * (κsol - ksup * Cos[ϑ]) - I * ϕ] * Sinc[(d1 / 2) * (κsol - ksup * Cos[ϑ])]
      + Exp[-I * ((h - d1) / 2) * (κsol + ksup * Cos[ϑ]) + I * ϕ] * Sinc[(d1 / 2) * (κsol + ksup * Cos[ϑ])]);
```

```
𝒟supDeg[σ_] := (d1 / 2) * (Exp[I * ((h - d1) / 2) * (κsol - ksup * Cos[σ * Degree]) - I * ϕ] * Sinc[(d1 / 2) * (κsol - ksup * Cos[σ * Degree])]
      + Exp[-I * ((h - d1) / 2) * (κsol + ksup * Cos[σ * Degree]) + I * ϕ] * Sinc[(d1 / 2) * (κsol + ksup * Cos[σ * Degree])]);
(* Element factor *)
ℰsupRad[σ_] := w1 * Exp[I * (w1 / 2) * (β - ksup * Sin[σ])] * Sinc[(w1 / 2) * (β - ksup * Sin[σ])];

(* Substrate *)
(* x-integral *)
𝒟subRad[σ_] := (d1 / 2) * (Exp[I * ((h - d1) / 2) * (κsol - ksub * Cos[σ]) - I * ϕ] * Sinc[(d1 / 2) * (κsol - ksub * Cos[σ])]
      + Exp[-I * ((h - d1) / 2) * (κsol + ksub * Cos[σ]) + I * ϕ] * Sinc[(d1 / 2) * (κsol + ksub * Cos[σ])]);
𝒟subDeg[σ_] := (d1 / 2) * (Exp[I * ((h - d1) / 2) * (κsol - ksub * Cos[σ * Degree]) - I * ϕ] * Sinc[(d1 / 2) * (κsol - ksub * Cos[σ * Degree])]
      + Exp[-I * ((h - d1) / 2) * (κsol + ksub * Cos[σ * Degree]) + I * ϕ] * Sinc[(d1 / 2) * (κsol + ksub * Cos[σ * Degree])]);
(* Element factor *)
ℰsubRad[σ_] := w1 * Exp[I * (w1 / 2) * (β - ksub * Sin[σ])] * Sinc[(w1 / 2) * (β - ksub * Sin[σ])];
```

Calculation of initial Floss factor for constant E0

```
TotalSincAsym = E0^2 * β / (2 * ω * μ0) * NIntegrate[(Cos[κsol * x - ϕ])^2, {x, -h/2, h/2}];
LossFactorAsymSup = μ0 * ω^3 * ε0^2 * (ε1 - ε2)^2 * E0^2 / (16 * Pi) * NIntegrate[(Abs[𝒟supRad[σ]])^2 * (Abs[ℰsupRad[σ]])^2, {σ, -Pi/2, Pi/2}];
LossFactorAsymSub = μ0 * ω^3 * ε0^2 * (ε1 - ε2)^2 * E0^2 / (16 * Pi) * NIntegrate[(Abs[𝒟subRad[σ]])^2 * (Abs[ℰsubRad[σ]])^2, {σ, Pi/2, 3*Pi/2}];
TotalLossFactor = LossFactorAsymSup + LossFactorAsymSub;
Floss = TotalLossFactor / TotalSincAsym ;
NumberForm[Floss, 10]
```

Automized iteration step Floss
(until Floss value changes by less than 10^{-10} of the value at previous iteration)

```
Flossold = 100 ; (* Random initial value to start while loop *)
Flossnew = 0.001; (* Random initial value to start while loop *)
While[Abs[((Flossnew - Flossold) / Flossold)] > 10^-10,
 (* New ℰ factor with exponential loss based on previous Floss factor *)
 Flossold = Floss;
 (* For superstrate *)
 ℰsupRad[σ_] := (-1 + Exp[I * w1 * (β - ksup * Sin[σ])] * Sqrt[1 - Floss]) / (I * (β - ksup * Sin[σ]) + (Log[1-Floss] / 2w1));
 (* For substrate *)
 ℰsubRad[σ_] := (-1 + Exp[I * w1 * (β - ksub * Sin[σ])] * Sqrt[1 - Floss]) / (I * (β - ksub * Sin[σ]) + (Log[1-Floss] / 2w1));

 (* Calculate new Floss factor with these new ℰ factors *)
 LossFactorAsymSup = μ0 * ω^3 * ε0^2 * (ε1 - ε2)^2 * E0^2 / (16 * Pi) * NIntegrate[(Abs[𝒟supRad[σ]])^2 * (Abs[ℰsupRad[σ]])^2, {σ, -Pi/2, Pi/2}];
 LossFactorAsymSub = μ0 * ω^3 * ε0^2 * (ε1 - ε2)^2 * E0^2 / (16 * Pi) * NIntegrate[(Abs[𝒟subRad[σ]])^2 * (Abs[ℰsubRad[σ]])^2, {σ, Pi/2, 3*Pi/2}];
 TotalLossFactor = LossFactorAsymSup + LossFactorAsymSub;
 Floss = TotalLossFactor / TotalSincAsym ;
 Flossnew = Floss;
]
NumberForm[Floss, 10]
(* Final value for Floss resulting from this iteration *)
```

Final script factors Flory (part 2)

```
(* rad=input σ in radians, deg=input σ in degree *)
```

Element factors

```
(* Superstrate *)
ℰsupRad[σ_] := (-1 + Exp[I * w1 * (β - ksup * Sin[σ])] * Sqrt[1 - Floss]) / (I * (β - ksup * Sin[σ]) + (Log[1-Floss] / 2w1));
ℰsupDeg[σ_] := (-1 + Exp[I * w1 * (β - ksup * Sin[σ * Degree])] * Sqrt[1 - Floss]) / (I * (β - ksup * Sin[σ * Degree]) + (Log[1-Floss] / 2w1));
(* Substrate *)
ℰsubRad[σ_] := (-1 + Exp[I * w1 * (β - ksub * Sin[σ])] * Sqrt[1 - Floss]) / (I * (β - ksub * Sin[σ]) + (Log[1-Floss] / 2w1));
ℰsubDeg[σ_] := (-1 + Exp[I * w1 * (β - ksub * Sin[σ * Degree])] * Sqrt[1 - Floss]) / (I * (β - ksub * Sin[σ * Degree]) + (Log[1-Floss] / 2w1));
```

Array factors (depending on type of period apodization. Again only run the correct one)

```
(* Case 1: Constant grating period *)
(* Superstrate *)
𝒜supRad[σ_] := (1 - (Exp[I * Λ * (β - ksup * Sin[σ])] * Sqrt[(1 - Floss)])^Ng) / (1 - Exp[I * Λ * (β - ksup * Sin[σ])] * Sqrt[(1 - Floss)]);
𝒜supDeg[σ_] := (1 - (Exp[I * Λ * (β - ksup * Sin[σ * Degree])] * Sqrt[(1 - Floss)])^Ng) / (1 - Exp[I * Λ * (β - ksup * Sin[σ * Degree])] * Sqrt[(1 - Floss)]);
(* Substrate *)
𝒜subRad[σ_] := (1 - (Exp[I * Λ * (β - ksub * Sin[σ])] * Sqrt[(1 - Floss)])^Ng) / (1 - Exp[I * Λ * (β - ksub * Sin[σ])] * Sqrt[(1 - Floss)]);
𝒜subDeg[σ_] := (1 - (Exp[I * Λ * (β - ksub * Sin[σ * Degree])] * Sqrt[(1 - Floss)])^Ng) / (1 - Exp[I * Λ * (β - ksub * Sin[σ * Degree])] * Sqrt[(1 - Floss)]);
```

```
(* Case 2: Linearly varying grating period *)
(* Superstrate *)
ℜsupRad[σ_] := Sum[(1 - Floss)^(n/2) * Exp[I * (β - ksup * Sin[σ]) * (n * Δ1 + 0.5 * n * (n - 1) * dΔ)], {n, 0, (Ng - 1)}];
ℜsupDeg[σ_] := Sum[(1 - Floss)^(n/2) * Exp[I * (β - ksup * Sin[σ * Degree]) * (n * Δ1 + 0.5 * n * (n - 1) * dΔ)], {n, 0, (Ng - 1)}];

(* Substrate *)
ℜsubRad[σ_] := Sum[(1 - Floss)^(n/2) * Exp[I * (β - ksub * Sin[σ]) * (n * Δ1 + 0.5 * n * (n - 1) * dΔ)], {n, 0, (Ng - 1)}];
ℜsubDeg[σ_] := Sum[(1 - Floss)^(n/2) * Exp[I * (β - ksub * Sin[σ * Degree]) * (n * Δ1 + 0.5 * n * (n - 1) * dΔ)], {n, 0, (Ng - 1)}];

(* Case 3: Random varying grating period *)
(* Superstrate *)
ℜsupRad[σ_] := Sum[(1 - Floss)^(n/2) * Product[Exp[I * Δ[[m]] * (β - ksup * Sin[σ])], {m, n}], {n, 0, Ng - 1}];
ℜsupDeg[σ_] := Sum[(1 - Floss)^(n/2) * Product[Exp[I * Δ[[m]] * (β - ksup * Sin[σ * Degree])], {m, n}], {n, 0, Ng - 1}];
(* Substrate *)
ℜsubRad[σ_] := Sum[(1 - Floss)^(n/2) * Product[Exp[I * Δ[[m]] * (β - ksub * Sin[σ])], {m, n}], {n, 0, Ng - 1}];
ℜsubDeg[σ_] := Sum[(1 - Floss)^(n/2) * Product[Exp[I * Δ[[m]] * (β - ksub * Sin[σ * Degree])], {m, n}], {n, 0, Ng - 1}];
```

Calculation Radiated Poynting vector S and E field at certain height above the grating coupler

```
(* Seperate calculations for substrate and superstrate due to difference in k-vector, σ in degree *)
SsupDeg[σ_, r_] := (μ0 * ω^3 * ε0^2 * (ε1 - ε2)^2 * E0^2) / (16 * Pi * r) * (Abs[ℜsupDeg[σ]])^2 * (Abs[𝔇supDeg[σ]])^2 * (Abs[𝔖supDeg[σ]])^2;
SsubDeg[σ_, r_] := (μ0 * ω^3 * ε0^2 * (ε1 - ε2)^2 * E0^2) / (16 * Pi * r) * (Abs[ℜsubDeg[σ]])^2 * (Abs[𝔇subDeg[σ]])^2 * (Abs[𝔖subDeg[σ]])^2;

EfieldSup[x_, z_] := -((I * μ0 * ω^2 * ε0 * (ε1 - ε2) * E0) / 4) * Sqrt[2 / (Pi * ksup * Sqrt[x^2 + z^2])] * Exp[-I * (Pi / 4)] * Exp[I * ksup * Sqrt[x^2 + z^2]]
* Exp[I * z0 * (β - ksup * (z / Sqrt[x^2 + z^2]))] * ℜsupRad[ArcTan[z / x]] * 𝔖supRad[ArcTan[z / x]] * 𝔇supRad[ArcTan[z / x]];
```

Final figure of Srad at r = 1 meter

```
r = 1; (* radius in meters *)
plot1 = Plot[SsupDeg[σ, r], {σ, 0, 90}, PlotRange → Full, MaxRecursion → $RecursionLimit];
plot2 = Plot[SsubDeg[σ, r], {σ, 90, 270}, PlotRange → Full, MaxRecursion → $RecursionLimit];
plot3 = Plot[SsupDeg[σ, r], {σ, 270, 360}, PlotRange → Full, MaxRecursion → $RecursionLimit];
Show[plot1, plot2, plot3, PlotRange → Full, AxesLabel → {"σ (degree)", "S_rad at a radius of 1 m (W/m^2)"}]
```

Figure A.1: Mathematica script of the BA-GCE model.

Appendix B: Equivalent structure calculation large grating couplers

As mentioned in section 4.2, the equivalent structure of the experimentally measured large grating couplers has to be determined in order to compute the radiated fields with the BA-GCE model. The large grating couplers have the grating etched into the superstrate layer, as indicated in the left layer stack of figure B.1. In order to compute the radiated fields with the BA-GCE model, the equivalent structure with the layer stack on the right of figure B.1 has to be determined, since the grating must be etched into the waveguide layer in this model. Hence, the additional SiO_2 superstrate layer has to be completely removed and the grating needs to be etched into the InP waveguide layer. In the search for the equivalent structure, the thickness of the InP layer in the etched grooves remains 300 nm. In addition, also the grating period Λ and the FF are the same as in the real structure. The only variable that is adjusted to find the equivalent structure is the thickness of the additional blocks of InP on top of the waveguide which constitute the grating. This is indicated by ? in figure B.1.

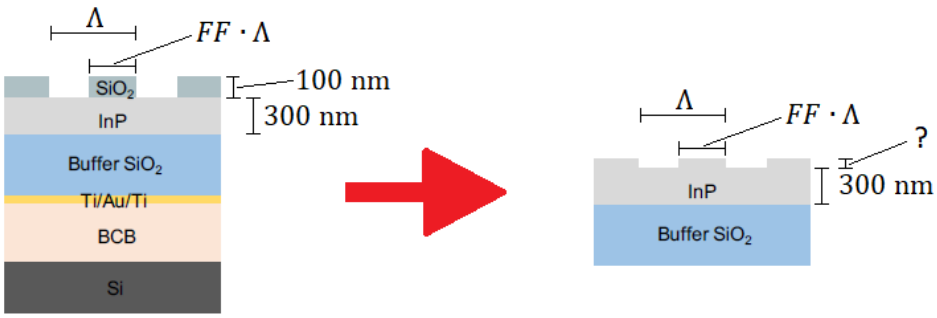

Figure B.1: Real layer stack of the large grating couplers (left) and the equivalent layer stack for in the BA-GCE model (right). For the equivalent layer stack the thickness of the additional blocks of InP on top of the waveguide (?) needs to be determined. Adapted from: [36]

The real structures that are simulated are identical to the grating coupler structures that are measured, except that the number of grating elements (N) has been reduced in order to decrease the computational burden of the Lumerical simulations. The real structures have a grating period (Λ) of 600 nm, a waveguide height (h) of 300 nm, an etch depth of 100 nm into the superstrate and the material properties of the layer stack of figure B.1. There are three different variations of this grating coupler structure measured: FF = 0.5, FF = 0.65 and FF = 0.8. Thus, the equivalent structure is also determined for all these three variants. The final results after an extensive investigation are shown in figures B.2, B.3 and B.4. In these figures the red curves show the Lumerical results when the real grating coupler structure is simulated and the black curves show the results of the BA-GCE model with the equivalent structure. The red curve is almost invisible because it is exactly below the black curve, which is also confirmed by the values of the peak characteristics. The equivalent structures have the following parameter values:

$$\text{FF} = 0.5: \ ? = 2.933\text{nm} \tag{1}$$

$$\text{FF} = 0.65: \ ? = 3.772\text{nm} \tag{2}$$

$$\text{FF} = 0.8: \ ? = 4.635\text{nm} \tag{3}$$

The question mark refers to the thickness of the additional blocks of InP on top of the waveguide that constitute the grating, as defined in figure B.1. Since a similar level of agreement was found between the real and equivalent structures for different numbers of grating elements, it is concluded that these equivalent structures can indeed be used in the BA-GCE model to replicate the radiation from the real structures. Hence, the values in equations 1, 2 and 3 are used to compute the fields of the experimentally measured large grating couplers with the BA-GCE model, for which the results are provided in section 4.2. A remark must be made that this investigation focused only on the normalized radiation profiles, since the profiles in section 4.2 are also normalized. Hence, the peak values of the radiation patterns of both structures are not made equivalent.

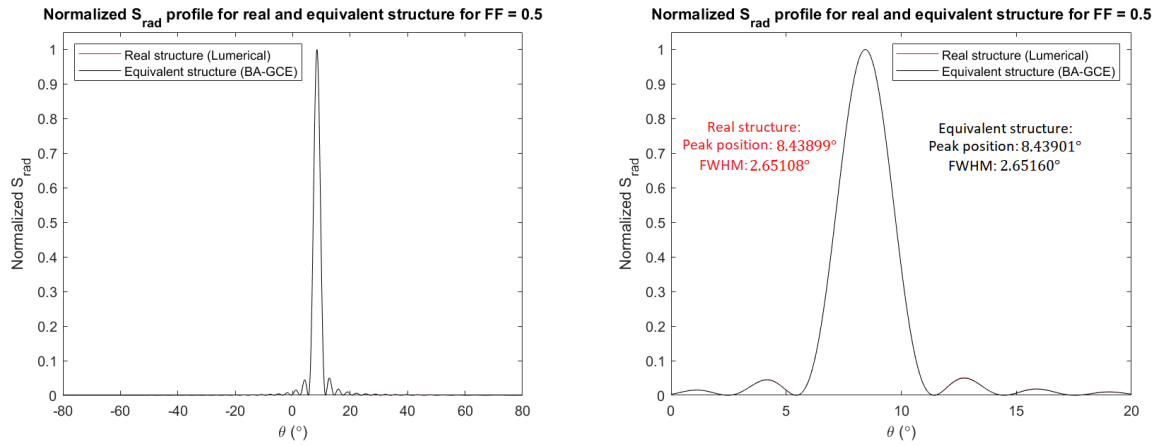

Figure B.2: Normalized spectrum for the radiated Poynting vector (S_{rad}) into the superstrate and a zoom of the peak with relevant characteristic values (right) for the real structure (red) and the equivalent structure in the BA-GCE model with additional InP blocks of 2.933 nm thick (black), for FF = 0.5.

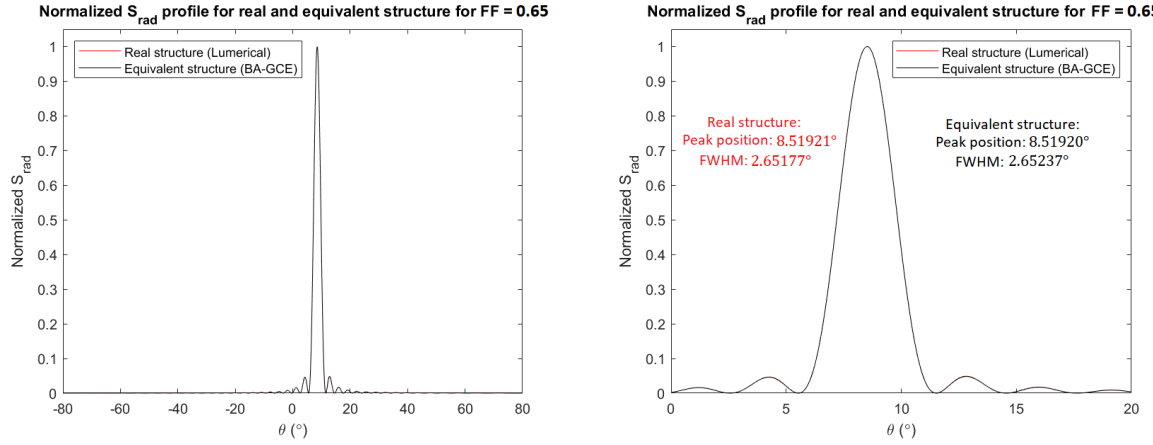

Figure B.3: Normalized spectrum for the radiated Poynting vector (S_{rad}) into the superstrate and a zoom of the peak with relevant characteristic values (right) for the real structure (red) and the equivalent structure in the BA-GCE model with additional InP blocks of 3.772 nm thick (black), for FF = 0.65.

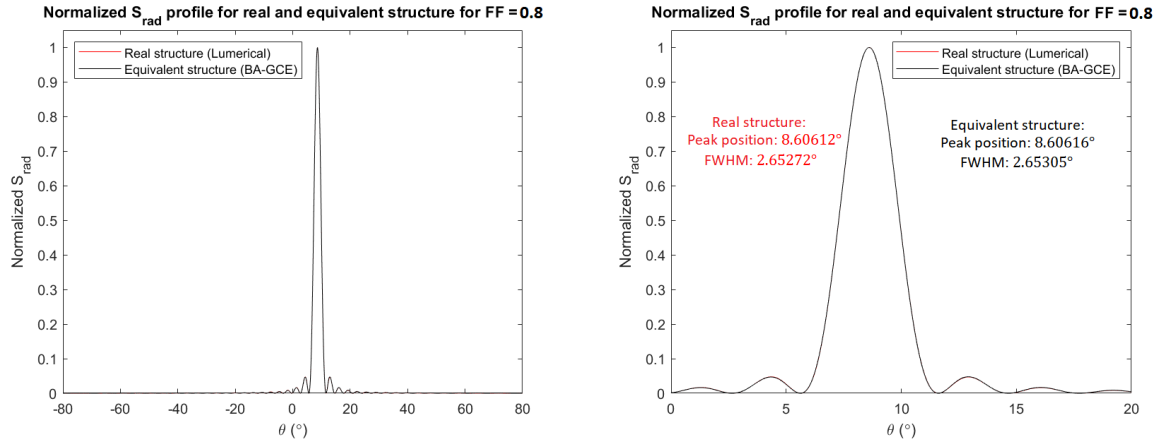

Figure B.4: Normalized spectrum for the radiated Poynting vector (S_{rad}) into the superstrate and a zoom of the peak with relevant characteristic values (right) for the real structure (red) and the equivalent structure in the BA-GCE model with additional InP blocks of 4.635 nm thick (black), for FF = 0.8.

Appendix C: Angle polished fiber calculation

This section will provide the calculation that is used to convert the beam output angle of the fibers, as obtained from the measurements in section 6.1, into a value for its polished angle, in order to compare it with the specifications of the manufacturer.

Consider the angle polished fiber configuration as illustrated in figure C.1, including the definitions of the angles θ_{air}, $\theta_{cladding}$ and θ_{fiber}. The light travelling through the core of the fiber will undergo TIR at the cleaved facet if it satisfies the condition for this. The condition for TIR is that the incoming angle (with respect to the cleaved facet normal) needs to be larger than the critical angle for TIR. The critical angle for TIR at the cleaved facet interface is given by:

$$\theta_{critical} = \arcsin\left(\frac{n_{air}}{n_{core}}\right) \tag{4}$$

From geometrical considerations it follows that the angle $\theta_{cladding}$ after this total internal reflection is defined by equation 5.

$$\theta_{cladding} = 90° - 2\theta_{fiber} \tag{5}$$

The exact values of the refractive indices of the optical fibers used in the experimental setup are not provided by the manufacturer. Nevertheless, fibers of this type typically have a refractive index of the core and the cladding of approximately 1.444 at the wavelength of 1550 nm [46]. Obviously, the core will have a slightly higher refractive index than the cladding in order to confine and guide the light through the core. Since this difference is usually very small, both refractive indices can be taken equal to 1.444 in good approximation. For this reason, the refraction at the core-cladding interface can be neglected. Hence, refraction happens at the air-cladding interface with an incident angle given by $\theta_{cladding}$. Snell's law describing refraction at interfaces then results in an output angle given by:

$$\theta_{air} = \arcsin\left(\frac{n_{cladding}}{n_{air}}\sin\left(\theta_{cladding}\right)\right). \tag{6}$$

Substitution of equation 5 into equation 6 and rewriting, results in the following expression for the polished angle (θ_{fiber}) as a function of the output angle (θ_{air}):

$$\theta_{fiber} = \frac{1}{2}\arccos\left(\frac{n_{air}}{n_{cladding}}\sin\left(\theta_{air}\right)\right) \tag{7}$$

Equation 7 is used in section 6.1 to convert the measured output angle to a value for the polished angle to compare it with the manufacturer specifications.

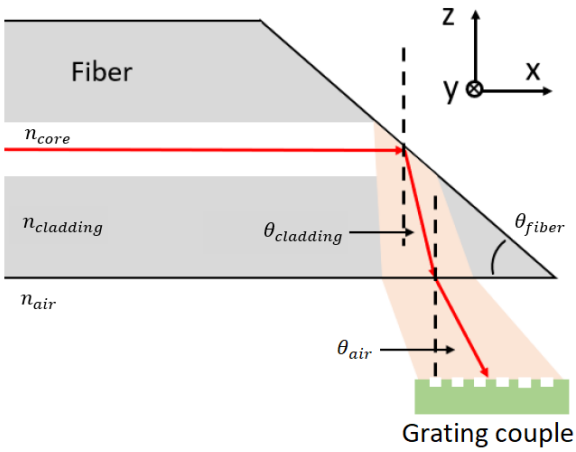

Figure C.1: Configuration of the angle polished fiber incident on the grating couplers, including the definitions of the various angles. Adapted from: [7]